Magnetic Systems studied by First-Principles Thermodynamics

Fritz Körmann

Paderborn 2011

Magnetic Systems studied by First-Principles Thermodynamics

Dissertation
zur Erlangung des akademischen Grades
Doktor der Naturwissenschaften (Dr. rer. nat.)
vorgelegt dem
Department Physik der Fakultät für Naturwissenschaften
an der Universität Paderborn

Fritz Körmann

Promotionskommission	
Vorsitzender	Prof. Dr. Klaus Lischka
Gutachter	Prof. Dr. Jörg Neugebauer
Gutachter	Prof. Dr. Arno Schindlmayr
Gutachter	Prof. Dr. Igor A. Abrikosov

Tag der Einreichung:	14. Februar, 2011
Tag der mündlichen Prüfung:	03. Mai, 2011

To my family...

Danksagung

Zuallererst danke ich Herrn Prof. Dr. Jörg Neugebauer nicht nur für das spannende Thema dieser Dissertation, sondern auch dafür, dass ich viel von ihm lernen durfte. Er hat die Arbeit durch gezielte Fragestellungen in den entscheidenden Phasen auf Kurs gehalten. Mein besonderer Dank gilt auch Tilmann Hickel und Alexey Dick. Durch viele Gespräche haben sie die Arbeit entscheidend mitgeprägt. Ich möchte Beiden für die unbeschreibliche Unterstützung während der gesamten Zeit (nicht nur bei physikalischen Fragestellungen) als auch für detaillierte Verbesserungsvorschläge zu dieser Arbeit danken.

Blazej Grabowski danke ich für unzählige Diskussionen rund um die Physik, insbesondere für die Einführung in die Berechnung vibronischer und elektronischer Entropiebeiträge. Nicht unerwähnt möchte ich Ugur Aydin, Sixten Boeck, Björn Lange, Gernot Pfanner, Niko Sandschneider und Alexander Udyansky lassen (in alphabetischer Reihenfolge), denen ich viele, viele interessante Gespräche zu verdanken habe. Ein lieber Dank gilt Ugur, dass er mir den größeren Teil der Kaffee-Verwaltung unserer Abteilung abgenommen hat. Frau Helemann danke ich für die Bewältigung vieler organisatorischer Aufgaben sowie aller Fragen rund um das Thema Fussball. Der gesamten Abteilung verdanke ich ein ausgezeichnetes Arbeitsklima, welches den entscheidenden Grundstein für die Arbeit gelegt hat. Albert, Alexander, Björn, Johann, Niko und Ugur danke ich für das Korrekturlesen. Der Max-Planck-Gesellschaft sowie ICAMS bin ich für die finanzielle Unterstützung während der Promotion zu Dank verpflichtet.

Ausserhalb des Instituts gilt mein Dank vor allem meinen Eltern und Geschwistern, für ihre stete Unterstützung in allen Zeiten. Mein letzter Dank gilt meiner kleinen Familie. Dank ihrer kann ich jeden Tag neue Kraft tanken und mich jeden Morgen mit einem Lächeln auf den Lippen erwischen.

"*Zu einer friedlichen Familie kommt das Glück von selbst.*"
Sprichwort aus China

Abstract

A major challenge in applying state-of-the-art density functional theory (DFT) simulation tools on real materials is that they have been originally designed to predict ground-state properties. Since finite temperature effects are crucial for practically all real-world applications, extending DFT capabilities towards finite temperature predictions is indispensable. Within the last few years it has been shown that a careful consideration of different temperature induced excitation processes such as lattice and electronic contributions can provide extremely accurate finite-temperature predictions for nonmagnetic materials. However, for the vast variety of materials, such as metallic alloys, magnetic shape memory alloys, or diluted magnetic semiconductors, where magnetic interactions and excitation processes are critical and cannot be neglected, the nonmagnetic approaches are not sufficient. So far practically no theoretical concepts to include magnetic excitations and to bridge between (i) the complexity of real structural materials, (ii) magnetic theories which are designed to describe very particular model systems, and (iii) DFT calculations exist.

In this work we have closed the gap between these three fields. A key challenge is that highly accurate techniques such as Spin Quantum Monte Carlo work best for frustration-free spin systems, whereas practically all real world materials show an oscillatory and long-range magnetic interaction resulting into spin frustration when being mapped onto model Hamiltonians. Therefore, finite temperature magnetism of real systems is commonly described using classical approaches such as classical Spin Monte Carlo. These methods work well for temperatures well above the critical (Curie, Néel) temperature, but fail for low temperatures, where spin-quantization becomes crucial. A key concern in this work is the correct incorporation of quantum effects into our models which turned out to be mandatory even up to the critical temperature. We, therefore, developed a hierarchy of numerically exact quantum Monte Carlo based methods and analytical (Green's functions) approaches to treat the magnetic free energy of complex magnetic materials. The proposed approach allowed us to describe the free energies with a hitherto not achievable accuracy for a wide range of materials. Successful applications include key materials in steel manufacturing like ferrite and cementite as well as various magnetic metals (e.g., nickel and cobalt). A careful analysis of these results allowed us for the first time to evaluate the relevance of spin quantum effects on thermodynamic properties. In contrast to common belief, we could show that spin quantum effects have a dramatic impact on various quantities such as free energies, heat capacities, and magnetizations, all the way up to the critical (Curie, Néel) temperature. The presented methodologies also provide a clear and systematic separation of different physically relevant contributions and are even applicable to phases which are not or only hardly accessible by experiment (such as, e.g., metastable phases), or systems where experimental input simply does not exist.

Contents

Chapter 1

Introduction

The development and improvement of functional materials, such as, e.g., steels, is a key concern since thousands of years. To give an example, the earliest known production of steel (i.e., iron with a small amount of carbon) is about 4000 years old [1]. Today, steel is one of the most important materials in our daily life (buildings, ships, tools, cars, etc.) with more than 1300 million tons produced annually worldwide, see Fig. 1.1. Along with the production, the demand on new structural materials with

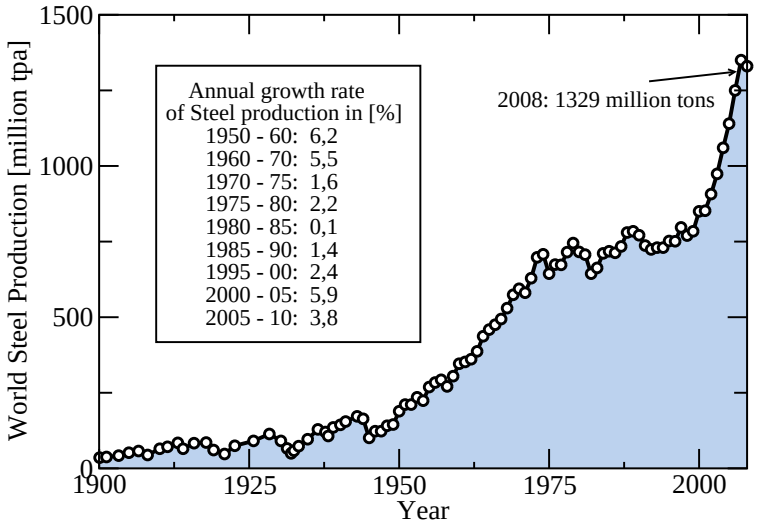

Figure 1.1: World Steel production for 1900-2008. Data taken from Refs. [2] and [3].

well defined properties (e.g., ultra-light weight steels) has also significantly increased. Every new steel generation goes along with new and more complex physical mechanisms often increasing the involved number of parameters (constituents) as well. A typical example of a modern manganese steel is given by [4]

$$\mathrm{Fe_{77.98}Mn_{20.98}C_{0.71}Si_{0.17}Ni_{0.04}N_{0.02}Cr_{0.02}Nb_{0.02}Mo_{0.01}Al_{0.01}Cu_{0.01}Co_{0.01}}... \qquad \text{(in wt.\%)}$$

with 16 ingredients in total. Refinement of such compositions by pure experimental approaches becomes not only time-consuming, but more and more economically expensive. To cope with this

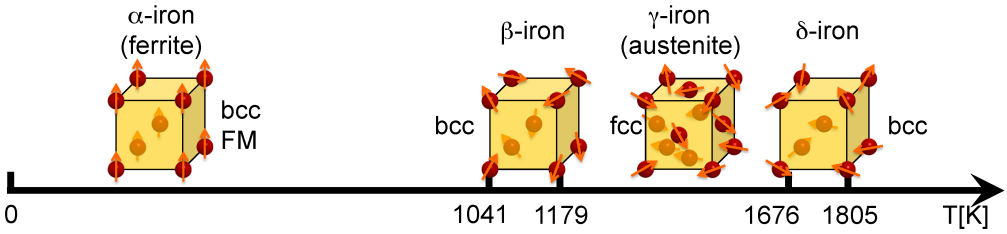

Figure 1.2: The temperature driven structural phase transitions of pure iron. Details are given in the text.

large configurational space, approaches such as CALPHAD (calculation of phase diagrams) have been developed, which are based on experimental input and sophisticated interpolation schemes. However, in absence of experimental input, such approaches can fail dramatically.

A very recent approach has attracted a lot of attention starting from the most elementary microscopic level - quantum mechanics. This approach is only based on the fundamental physical constants such as nuclei and electron mass and charge, and allows completely parameter-free and unbiased materials properties prediction without any experimental input. This method is, therefore, called first principles or, using the Latin term, *ab initio* technique.

A major challenge in applying state-of-the-art density functional theory (DFT) simulation tools to real materials is that they have been originally designed to predict ground-state properties ($T = 0$ K). Since finite-temperature effects are crucial for practically all real-world applications, extending DFT capabilities towards finite-temperature predictions is indispensable. Fortunately, nowadays sophisticated combined concepts exist (e.g., the so-called quasiharmonic approximation and finite temperature DFT), which allow a highly accurate prediction of properties of *nonmagnetic* materials even up to the melting temperature [5]. As shown recently [6], such an approach is, however, not sufficient for the main ingredient of steels and the most famous *magnetic* material, namely iron. Iron shows a complex and untypical order of structural phase transitions, illustrated in Fig. 1.2. At low temperatures iron crystalizes in the bcc structure called α-iron or ferrite. Above the Curie temperature $T_C = 1043$ K, the paramagnetic bcc Fe (β-iron) transforms at 1184 K into the more close-packed fcc lattice, also called γ-iron or austenite. At 1673 K Fe undergoes a second structural transition and becomes bcc again (δ-iron) until it melts at about 1800 K. It is known that in particular the magnetic excitations are of fundamental importance for the structural transitions and phase stability [7, 8]. However, the theoretical concepts to predict magnetic contributions to thermodynamic properties based on DFT input is still in its infancy.

The reason for this is that so far practically no theoretical concepts to include magnetic excitations and to bridge between (i) the complexity of real structural materials, (ii) magnetic theories which are designed to describe very particular model systems, and (iii) DFT calculations exist. Starting from the microscopic theory, the extension of DFT towards the spin-polarized DFT (SDFT), first introduced by von Barth and Hedin [9], is nowadays well established for the computation of ground-state properties of magnetic systems [10]. To investigate finite-temperature properties it is, however, indispensable to recourse to model considerations. Besides the Ising model and effective theories such as the Weiss mean field theory for ferromagnets, more realistic theoretical descriptions have become possible by the quantum-mechanical Heisenberg model [11]. In the last two decades a

number of techniques (such as the frozen-magnon approach [12]) emerged, which allow to extract realistic Heisenberg model parameters from SDFT methods. A key challenge is that highly accurate techniques to solve the model such as Spin Quantum Monte Carlo work best for frustration-free spin systems, whereas practically all real world materials show an oscillatory and long-range magnetic interaction resulting into spin frustration when being mapped onto model Hamiltonians. Therefore, finite-temperature magnetism of real systems is commonly described using classical approaches such as classical Spin Monte Carlo [13–17]. These methods work well for temperatures well above the critical (Curie, Néel) temperature, but fail for low temperatures, where spin-quantization becomes crucial.

A key concern in this work is the correct incorporation of quantum effects into our models. We, therefore, developed a hierarchy of numerically exact quantum Monte Carlo based methods and analytical (Green's functions) approaches to treat the magnetic free energy of complex magnetic materials. The proposed approach allowed us to describe the free energies with a hitherto not achievable accuracy for a wide range of materials. Successful applications include key materials in steel manufacturing like ferrite and cementite as well as various magnetic metals (e.g., nickel and cobalt). A careful analysis of these results allowed us for the first time to evaluate the relevance of spin quantum effects on thermodynamic properties. The presented methodologies also provide a clear and systematic separation of different physically relevant contributions and are even applicable to phases which are not or only hardly accessible by experiment (such as, e.g., metastable phases), or systems where experimental input simply does not exist.

This work is organized as follows: After introducing the theoretical fundamentals (Chap. 2), we focus in Sec. 3.1 on the pressure dependence of the critical temperature $T_C(p)$ of pure iron. We show that the experimentally observed weak dependence on pressure for iron ($T_C^{\mathrm{exp}}(p) \approx 0$) can be understood by a competition between two mechanisms. These investigations revealed that in particular the RPA provides a promising approach to study magnetic properties. The theory, which was originally designed for predicting the magnetization as well as T_C [18], is therefore extended to compute also quantities such as free energies and heat capacity capacities. The results of the derived theory are finally combined with vibronic and electronic contributions (Sec. 3.2.1) in order to achieve a fully *ab initio* framework for the thermodynamic properties of bcc iron.

A shortcoming of the analytic RPA treatment is, by construction, the neglect of magnetic short-range order. A numerically exact Quantum Monte Carlo (QMC) simulation appears as the ideal candidate for this purpose. We show, however, that this technique is not applicable for a realistic system such as bcc iron due the negative sign problem. In an extensive comparison between the numerically exact quantum and classical results of the Heisenberg model for various thermodynamic properties, the advantages and disadvantages of a *classical* approach to the *quantum* Heisenberg model become apparent (Sec. 3.2.2). Based on the results of the model calculations, a semi-empirical rescaling function is derived. The rescaling method allows an *ad hoc* inclusion of quantum effects in the classical description and its application to bcc iron is discussed in comparison with experimental data.

The fcc phase of iron is in the focus of Sec. 3.3. Fcc iron constitutes a challenging task for the theoretical modeling: Recent theoretical calculations reveal a non-collinear spin-spiral ground state [19], which is a particular challenge for analytic treatments such as the RPA, typically requiring

a global quantization axis (as given for ferro- or antiferromagnets). Working in a locally rotated coordinate system allows us to generalize the RPA theory, which is developed for bcc iron, to non-collinear magnetic spin system. We apply both, the generalized RPA as well as the classical Monte Carlo method to fcc iron, and combine the results with vibronic and electronic contributions.

Particularly, a model study (Sec. 3.2.2) shows that the thermodynamic properties are robust with respect to the specific magnetic configuration or the range of magnetic exchange interaction, if considered on a *reduced* $t = T/T_C$ temperature scale. This encourages a decoupling of T_C from other thermodynamic properties such as the specific heat capacity. Based on this insight we propose a nearest-neighbor model, which can be solved quantum-mechanically *and* numerically exact using QMC (Sec. 3.4). The shortcomings and advantages of this ansatz are critically evaluated on the three prototype ferromagnets Fe, Co, and Ni.

Finally, the thermodynamic properties of cementite, the most common precipitate phase in Fe-C steels (see Fig. 1.2), are investigated in Sec. 3.5. The impact of magnetic contributions for selected properties such as the specific heat capacity or formation enthalpy are discussed. This example highlights that the developed methods in this work not only allow insights into fundamental aspects of pure elementary magnets such as iron, cobalt, or nickel, but could be employed to address even properties of complex magnetic materials.

Chapter 2

Theoretical Background

The first-principles thermodynamic description of magnetic materials is the central aim of this work. A key quantity in the thermodynamic description is the thermodynamic potential. In principle its knowledge provides access to all thermodynamic equilibrium properties. For the methodologies in this work it is convenient to start with the Helmholtz free energy (Helmholtz potential) $F(T, V)$, with temperature T and volume V as natural variables. It is completely determined by the partition sum $Z(T, V) = \mathrm{Tr}\ \mathrm{e}^{-\beta\mathcal{H}}$ as

$$F(T, V) = -k_B T\ \ln Z(T, V). \tag{2.1}$$

The key challenge in order to access $F(T, V)$ is the computation of the trace in Z. This requires the solution of the Schrödinger equation

$$\mathcal{H}\Psi_\nu = E_\nu \Psi_\nu, \tag{2.2}$$

where $\Psi_\nu \equiv \Psi_\nu(\{\boldsymbol{r}_{i\sigma_i}\}, \{\boldsymbol{R}_I\})$ represents the many-particle wave function, $\{\boldsymbol{r}_{i\sigma_i}\}$ and $\{\boldsymbol{R}_I\}$ denote the complete set of coordinates for the electrons with spin $\sigma_i = (\uparrow, \downarrow)$ and nuclei respectively, and E_ν represents the ν's energy levels of the system. However, although the microscopic eigenvalue problem (2.2) can be readily formulated, a direct solution is in general impractical. Describing a *solid* involves a many-body problem of an immense number of particles (the number of nuclei N_n and electrons N_e are in the order of $\sim 10^{23}$ particles per cm^3). A direct treatment of Eq. (2.2) is therefore not feasible and simplifications are mandatory.

One of the most important approximations is the adiabatic decoupling of the ionic, electronic, and magnetic degree of freedom. This is justified by considering the different time scales of the underlying physical excitations. For the *d*-metals considered in the present study, the electronic excitations are inherently connected to the *d*-band width W_d revealing the underlying excitations in the order of $\hbar/W_d \sim 10^{-15}$ s. The characteristic time of spin-waves are inverse proportional to their excitation energy, $1/\omega_{\mathrm{SW}} \sim 10^{-13}$ s, and vibronic excitations are characterized by their inverse

Debye temperature $\sim 10^{-12}$ s.[1] As sketched in Fig. 2.1 the adiabatic decoupling for the Helmholtz free energy results in

$$F(T,V) = F^{\mathrm{el}}(T,V) + F^{\mathrm{vib}}(T,V) + F^{\mathrm{mag}}(T,V) + \ldots, \tag{2.3}$$

where the "..." symbolize higher order terms (such as, e.g., coupling terms or vacancy contributions) and F^{el}, F^{vib}, and F^{mag} denote the electronic, vibronic, and magnetic contribution, respectively.

In a similar way the adiabatic decoupling can be employed on the microscopic level for the Schrödinger equation (2.2). Regarding the energy scale, the fastest degree of freedom is realized for the electronic subsystem. Its solution involves still a huge number of particles N_e. A very elegant and powerful method to solve the electronic subsystem in its ground state was introduced in 1963 by W. Kohn, the reformulation of the many-body problem Eq. (2.2) in terms of the electronic density, namely the development of the density functional theory (DFT). Although the DFT is in principle an exact theory, for a practical implementation an approximation for the so called exchange-correlation (xc) functional is required. For the xc-functional well established and carefully tested approximations exist nowadays so that DFT has become the most common applied first-principles approach in theoretical solid state physics for the prediction of properties at $T = 0$ K.

The extension towards finite temperatures is a challenging and nontrivial task. In order to address $T > 0$ K properties, and in particular to determine the free energy contributions, the knowledge of ground-state properties alone is not sufficient. At $T > 0$ K the number of possible microstates increases dramatically making the usage of statistical concepts in combination with DFT mandatory. In the last decades, the quasiharmonic approximation and the finite temperature DFT have been proven to provide a very accurate and realistic approach for F^{el} and F^{vib} respectively, see Fig. 2.1. Although the principle concepts behind were known since long time, the practical implementation in combination with DFT turns out to be a highly nontrivial and challenging task itself [5]. The inclusion of magnetic excitations into a full thermodynamic description is, however, still in its infancy. This is *inter alia* caused by the fact that even model Hamiltonians capturing the main underlying excitations are in general not exactly solvable.

This chapter is structured as follows: We start with the formulation of the microscopic many-body problem Eq. (2.2) and the introduction of the spin-polarized DFT. This provides the fundamentals for the further analysis at finite temperatures. The concepts to determine the electronic and vibronic contributions based on the DFT input are shortly discussed in Sec. 2.2.4.

In Sec. 2.2 an introduction into the different magnetic treatments at finite temperatures is given. In particular the Heisenberg model, chosen for the further analysis, is discussed in detail. Different analytic and numerical solution techniques are introduced. The section is concluded with the adiabatic spin dynamics. It is shown how spin-wave energies and effective exchange coefficients for the Heisenberg model can be determined by DFT.

[1] The decoupling of the electronic motion and that of the nuclei (Born-Oppenheimer approximation) is *a priori* backed up by the different masses of both particles. Note that a similar mass argument for the decoupling of the magnetic degree of freedom does not exist.

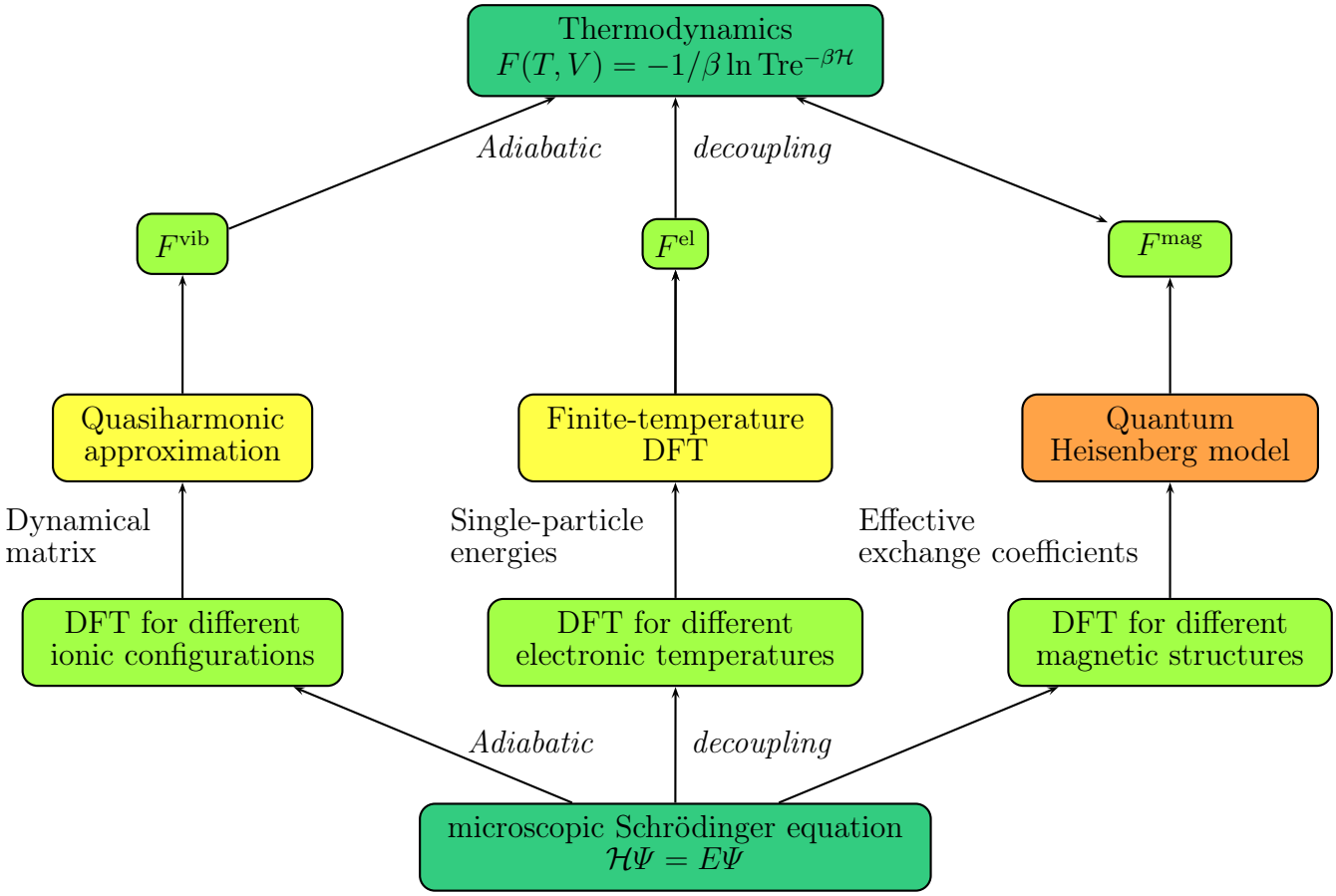

Figure 2.1: Sketch of the integrated *ab initio* approach to access thermodynamic properties of magnetic materials. The adiabatically decoupled free energy contributions as well as the adiabatically decoupled treatment via spin density functional theory are shaded in light green. The statistical concepts to capture the vibronic and electronic contributions are shaded in yellow, whereas the Heisenberg model, accounting for the magnetic degree of freedom, is highlighted in orange.

2.1 Many-Body Problem and Density Functional Theory

2.1.1 The Many-Body Problem

In principle, the many-body problem of interacting electrons and nuclei is completely determined by Eq. (2.2) as

$$\mathcal{H}\Psi_\nu(\{\boldsymbol{r}_{i\sigma_i}\},\{\boldsymbol{R}_I\}) = E_\nu\Psi_\nu(\{\boldsymbol{r}_{i\sigma_i}\},\{\boldsymbol{R}_I\}). \tag{2.4}$$

Defining the solid as a system of localized ions (nuclei) and a specific number of electrons, the full Hamiltonian[2]

$$\mathcal{H} = \mathcal{H}^{\mathrm{e}} + \mathcal{H}^{\mathrm{I}} + \mathcal{H}^{\mathrm{eI}} + \mathcal{H}^{\mathrm{z}} \tag{2.5}$$

is given by the following contributions:

The Hamiltonian of the *electronic subsystem* $\mathcal{H}^{\mathrm{e}}$ is split into the kinetic energy T^{e} and the electron-electron repulsion term V^{ee}:

$$\mathcal{H}^{\mathrm{e}} = T^{\mathrm{e}} + V^{\mathrm{ee}} = -\sum_i^{N_e}\frac{\hbar^2}{2m_e}\nabla_i^2 + \frac{1}{2}\sum_i^{N_e}\sum_{j\neq i}^{N_e}\frac{e^2}{4\pi\epsilon_0|\boldsymbol{r}_{i\sigma_i}-\mathbf{r}_{j\sigma_j}|}. \tag{2.6}$$

Here $\hbar$ denotes the reduced Planck constant, m_e the electron mass, e the elementary charge, ϵ_0 the electric constant (vacuum permittivity) and N_e the total number of electrons.

Analogously the operator of the *ionic subsystem* $\mathcal{H}^{\mathrm{I}}$ can be decomposed into a kinetic T^{n} and a repulsion term V^{nn} as

$$\mathcal{H}^{\mathrm{I}} = T^{\mathrm{n}} + V^{\mathrm{nn}} = -\sum_I^{N_n}\frac{\hbar^2}{2M_I}\nabla_I^2 + \frac{1}{2}\sum_I^{N_n}\sum_{J\neq I}^{N_n}\frac{Z_I Z_J e^2}{4\pi\epsilon_0|\mathbf{R}_I-\mathbf{R}_J|}, \tag{2.7}$$

where M_I denotes the mass and Z_I the number of protons of the I-th of the N_n nuclei.

The interaction of the electrons with the nuclei $\mathcal{H}^{\mathrm{eI}}$(repulsion term) and the (possible) interaction with an (external) magnetic field $\mathcal{H}^{\mathrm{z}}$ (Zeeman term) are defined as

$$\mathcal{H}^{\mathrm{eI}} + \mathcal{H}^{\mathrm{z}} = -\sum_i^{N_e}\sum_I^{N_n}\frac{Z_I e^2}{4\pi\epsilon_0|\boldsymbol{r}_{i\sigma_i}-\mathbf{R}_I|} + 2\mu_B\sum_i^{N_e}\boldsymbol{B}(\boldsymbol{r})\boldsymbol{\sigma}_i \equiv \boldsymbol{\upsilon}^{\mathrm{ext}}(\{\boldsymbol{r}_{i\sigma_i}\}), \tag{2.8}$$

where μ_B denotes the Bohr magneton, $\boldsymbol{B}$ an external field, $\boldsymbol{\sigma}_i = (\sigma_{ix},\sigma_{iy},\sigma_{iz})$ the spin operator, and $\sigma_{i,(xyz)}$ being the Pauli matrices. As already mentioned, the huge number of involved particles rules out a direct solution of the eigenvalue problem and several simplifications have to be accepted, which will be discussed in the following.

The Born-Oppenheimer Approximation

In 1927 Born and Oppenheimer suggested to decouple the electronic and ionic motion. Such an approximation is justified due to the huge unbalance between the mass of the electron and of the nucleus, $m_e \ll m_I$, yield different time scales of electronic and nuclei motion. Consequently, the

[2]This is the non-relativistic formulation of the Hamiltonian. It does not account for relativistic effects such as spin-orbit coupling. These contributions are, however, not relevant for this work and are neglected in the following.

electronic systems could be solved for a *fixed* (given) set of nuclei coordinates $\{\tilde{\mathbf{R}}_I\}$. Physically, this corresponds to the situation where the electrons follow the nuclei motion almost instantaneously or saying differently: the nuclei move on the energy surface E_ν^{BOS} defined by the energy of the electronic subsystem $E_\nu^{\mathrm{e}}(\{\boldsymbol{R}_I\})$ and the nuclei-nuclei-repulsion $V^{\mathrm{nn}}(\{\boldsymbol{R}_I\})$. The energy surface on which the nuclei move,

$$E_\nu^{\mathrm{BOS}} = E_\nu^{\mathrm{e}}(\{\boldsymbol{R}_I\}) + V^{\mathrm{nn}}(\{\boldsymbol{R}_I\}), \tag{2.9}$$

is called Born-Oppenheimer surface. It determines together with the kinetic energy the ionic contribution of Eq. (2.4),

$$\tilde{\mathcal{H}}^{\mathrm{I}}(\{\boldsymbol{R}_I\})\Theta_{\mu\nu} = \left(T^{\mathrm{n}}(\{\boldsymbol{R}_I\}) + E_\nu^{\mathrm{BOS}}(\{\boldsymbol{R}_I\})\right)\Theta_{\mu\nu} = E_{\mu\nu}^{\mathrm{I}}(\{\boldsymbol{R}_I\})\Theta_{\mu\nu}, \tag{2.10}$$

providing the $E_{\mu\nu}^{\mathrm{I}}$, where μ is running over all eigenenergies for a given potential surface ν. In practice, one usually considers out of the various potential energy surfaces E_ν^{BOS} only the energetically lowest one corresponding to the electronic ground state ($T = 0$ K), i.e., $E_\nu^{\mathrm{BOS}} \equiv E_0^{\mathrm{BOS}}$.

In principle, however, an analogous adiabatic decoupling could also be derived for finite temperatures using the same mass argument as for the derivation of the equation above. It is straightforward to show [20] that for $T > 0$ K the Born-Oppenheimer approximation leads to

$$\left(T^{\mathrm{n}}(\{\boldsymbol{R}_I\}) + F^{\mathrm{BOS}}(\{\boldsymbol{R}_I\}, T)\right)\tilde{\Theta}_\mu = \tilde{E}_\mu^{\mathrm{I}}(\{\boldsymbol{R}_I\}, T)\tilde{\Theta}_\mu, \tag{2.11}$$

where the temperature dependent Born-Oppenheimer surface is defined as

$$F^{\mathrm{BOS}} = -k_B T \ln \sum_\nu \mathrm{e}^{-\beta E_\nu^{\mathrm{BOS}}}. \tag{2.12}$$

It turns out, however, that $\tilde{E}_\mu^I(\{\boldsymbol{R}_I\}) \approx E_{\mu 0}^I(\{\boldsymbol{R}_I\})$, resulting in a negligible impact of applying Eq. (2.11) compared to Eq. (2.10) for the vibronic free energy.[3] In this work Eq. (2.10) is used in combination with the $T = 0$ K energy surface $E_{\nu 0}^{\mathrm{BOS}}$.

Employing the Born-Oppenheimer approximation, the electronic eigenvalue problem for a given set of nuclei coordinates ($\{\boldsymbol{R}_I\}$),

$$\tilde{\mathcal{H}}^{\mathrm{e}}\Phi_\nu^{\{\boldsymbol{R}_I\}}(\{\boldsymbol{r}_{i\sigma_i}\}) = \left(\mathcal{H}^{\mathrm{e}} + \boldsymbol{v}^{\mathrm{ext}}\right)\Phi_\nu^{\{\boldsymbol{R}_I\}}(\{\boldsymbol{r}_{i\sigma_i}\}) = E_\nu^{\mathrm{e}}(\{\boldsymbol{R}_I\})\Phi_\nu^{\{\boldsymbol{R}_I\}}(\{\boldsymbol{r}_{i\sigma_i}\}), \tag{2.13}$$

remains to be solved, involving a gigantic number of particles though.

The density functional theory, introduced next, allows an *enormous* reduction of the involved degrees of freedom.

2.1.2 Density Functional Theory

In this section we briefly discuss the fundamental aspects of the density functional theory and the most important involved simplifications and techniques.

The introduction of the density functional theory (DFT) in 1965 by W. Kohn, is certainly one

[3] In Ref. [5] it is shown on the specific example aluminum that incorporation of the electronic temperature for the derivation of F^{vib} results in energy corrections which are in magnitude smaller compared to the contribution of the quasiharmonic approximation or its higher order corrections (explicit anharmonic contributions).

of the fundamental breakthroughs in condensed matter physics in the last century. Since magnetic systems are in the focus of the present study we directly discuss the extension of DFT to spin-polarized systems, the so called spin-polarized DFT (SDFT), introduced by von Barth and Hedin [9] in 1972. The main concepts of both versions are, however, very similar.

The basic idea of the SDFT is to express the eigenvalue problem Eq. (2.13) not in terms of the many-body wave function $\Phi = \Phi(\{\boldsymbol{r}_{i\sigma_i}\})$, but instead in terms of the electronic density

$$n(\boldsymbol{r}) = \langle \Phi | \sum_i^{N_e} \delta(\boldsymbol{r} - \boldsymbol{r}_i) | \Phi \rangle, \tag{2.14}$$

and the magnetization density

$$\boldsymbol{m}(\boldsymbol{r}) = -2\mu_B \langle \Phi | \sum_i^{N_e} \boldsymbol{\sigma}_i \delta(\boldsymbol{r} - \boldsymbol{r}_i) | \Phi \rangle. \tag{2.15}$$

Both are for convenience often combined in the compact 2×2 spin-density matrix as

$$\boldsymbol{n}(\boldsymbol{r}) = \frac{1}{2} \left(n(\boldsymbol{r}) \mathbb{1} + \boldsymbol{\sigma} \boldsymbol{m}(\boldsymbol{r}) \right). \tag{2.16}$$

The original version of the *First Hohenberg Kohn theorem* states that for a nonmagnetic, nondegenerate electronic system in a given external potential v^{ext} (in absence of external fields), this potential is uniquely defined (within a trivial constant) by the ground-state electron density $n_0(r)$. Since by definition the kinetic and electron-electron interaction operators in $\mathcal{H}^e$ (see Eq. (2.6)) are fully determined by the total number of electrons N_e (which can be derived from the electronic density n as well), the complete eigenvalue problem Eq. (2.13) can be expressed as a functional of n. A similar unique correspondence in the SDFT between the spin density matrix $\boldsymbol{n}$ and a given external potential does, however, not exist. This was already recognized a long time ago by von Barth and Hedin [9], and formally shown independently by Capelle and Vignale [21] and Eschrig and Pickett [22]. The nonuniqeness is a generic feature of multidensity DFTs (as the spin-polarized DFT or the current-DFT) and the consequences are still under investigation [23–27]. There are indications that the non-invertibility is restricted to exceptional and rather artificial cases [24]. This assumption is empirical substantiated by the fact that the SDFT is the most widely used formulation of DFT in practical applications. If provided that the first theorem holds for SDFT as well, the external potential v^{ext}, and hence the total ground-state energy and all ground-state properties could be expressed as a functional of the ground-state spin density $\boldsymbol{n}_0$. Evidently, this yields a substantial reduction of the degrees of freedom (from the many-body wave function Φ towards the 2×2 spin density matrix $\boldsymbol{n}$ having 12 degrees of freedom).

The *Second Hohenberg-Kohn theorem* states that the total energy for a given density n is always greater or equal to the true ground-state energy defined by the corresponding ground-state density n_0. It is based on the Rayleigh-Ritz variational principle [28], according to which for any given

Hamiltonian $\mathcal{H}$ (and in particular $\tilde{\mathcal{H}}^{\mathrm{e}}$ in Eq. (2.13)) and any trial wave function Φ_{trial}, the expectation value of $\langle\mathcal{H}\rangle_{\Phi_{\mathrm{trial}}}$ is always greater than the ground-state energy E_0:

$$E^{\mathrm{tot}}[\Phi_{\mathrm{trial}}] \equiv \frac{\langle\Phi_{\mathrm{trial}}|\mathcal{H}^{\mathrm{e}}|\Phi_{\mathrm{trial}}\rangle}{\langle\Phi_{\mathrm{trial}}|\Phi_{\mathrm{trial}}\rangle} \geq E_0^{\mathrm{tot}}. \tag{2.17}$$

The theorem allows by virtue of the minimization above a straightforward way to find the ground-state energy by minimizing the functional $E^{\mathrm{tot}}[\Phi_{\mathrm{trial}}]$ with respect to Φ_{trial}. Since the ground-state density $\boldsymbol{n}_0$ uniquely determines the ground-state wave function $\boldsymbol{n}_0 \rightarrow \Phi_0$, E_0^{tot} is completely defined by $\boldsymbol{n}_0$ as well,

$$E^{\mathrm{tot}}[\Phi_0] \leftrightarrow E^{\mathrm{tot}}[\boldsymbol{n}_0] \equiv E_0^{\mathrm{tot}}, \tag{2.18}$$

and can be determined by minimizing (2.17).

The energy functional

$$E^{\mathrm{tot}}[\boldsymbol{n}(\boldsymbol{r})] = F[\boldsymbol{n}(\boldsymbol{r})] + \int \boldsymbol{n}(\boldsymbol{r})\boldsymbol{v}^{\mathrm{ext}}(\boldsymbol{r})d\boldsymbol{r} \tag{2.19}$$

contains, however, an unknown (yet universal, i.e., not depending on $\boldsymbol{v}^{\mathrm{ext}}$ though) functional

$$F[\boldsymbol{n}(\boldsymbol{r})] = \min_{\Phi_{\mathrm{trial}}\rightarrow\boldsymbol{n}(\boldsymbol{r})} \langle\Phi_{\mathrm{trial}}|\left(T^{\mathrm{e}} + V^{\mathrm{ee}}\right)|\Phi_{\mathrm{trial}}\rangle, \tag{2.20}$$

including T^{e} and V^{ee} given by the electronic subsystem Eq. (2.6).

The Hohenberg-Kohn theorems provide a major simplification by transferring the problem of dealing with the many-body wave function to the much simpler ground-state density. A (practical) route to treat the functional $F[\boldsymbol{n}]$ was proposed by Kohn and Sham in 1965.

Kohn-Sham Equations

In order to determine the functional $F[\boldsymbol{n}]$, Kohn and Sham introduced a fictitious auxiliary system of non-interacting electrons. The "trick" is to map the complex problem of *interacting* electrons in a given external potential $\boldsymbol{v}^{\mathrm{ext}}$ onto a system of *non-interacting* electrons in an effective, so called Kohn-Sham potential V^{KS} [29]. The potential V^{KS} of the auxiliary system is constructed in such a way that the electronic density of the non-interacting electron system equals the density of the interacting electronic system, i.e., $\boldsymbol{n} \equiv \boldsymbol{n}^{\mathrm{KS}}$.[4] This allows to reformulate the functional $F[\boldsymbol{n}]$ as

$$F[\boldsymbol{n}] = T^{\mathrm{KS}}[\boldsymbol{n}] + J[\boldsymbol{n}] + E^{\mathrm{xc}}[\boldsymbol{n}], \tag{2.21}$$

where the kinetic energy functional $T^{\mathrm{KS}}[\boldsymbol{n}]$ of the non-interacting electrons defined by the *single-particle* wave functions $\varphi_{i\alpha}^{\mathrm{KS}}$ could be expressed in a comparable simple form[5]

$$T^{\mathrm{KS}}[\boldsymbol{n}] \leftrightarrow T^{\mathrm{KS}}[\{\varphi_{i\alpha}^{\mathrm{KS}}\}] = -\sum_{\alpha=\uparrow,\downarrow}\sum_i \frac{1}{2}\langle\varphi_{i\alpha}^{\mathrm{KS}}|\nabla_i^2|\varphi_{i\alpha}^{\mathrm{KS}}\rangle, \tag{2.22}$$

[4] There is no exact proof that this mapping is always possible, see e.g. [10].

[5] Provided that the $\{\varphi_{i\alpha}^{\mathrm{KS}}\}$ are orthonormalized.

where the sum runs over all N_e occupied eigenstates. The Hartree term $J[\boldsymbol{n}]$ (classical electrostatic electron-electron interaction) in Eq. (2.21) is defined as

$$J[\boldsymbol{n}(\boldsymbol{r})] = J[n(\boldsymbol{r})] = \frac{e^2}{4\pi\epsilon_0}\frac{1}{2}\int\int \frac{n(\boldsymbol{r})n(\boldsymbol{r}')}{|\boldsymbol{r}-\boldsymbol{r}'|}d\boldsymbol{r}d\boldsymbol{r}'. \tag{2.23}$$

Apart from $J[\boldsymbol{n}]$ and $T^{\mathrm{KS}}[\boldsymbol{n}]$, which are explicitly known [see Eqs. (2.22) and (2.23)], the (unknown) correction including the kinetic energy difference of the non-interacting and interacting electronic system in Eq. (2.21) and the nonclassical contribution of the electron-electron repulsion is defined as the exchange-correlation energy

$$E^{\mathrm{xc}}[\boldsymbol{n}] \equiv T^{\mathrm{e}}[\boldsymbol{n}] - T^{\mathrm{KS}}[\boldsymbol{n}] + V^{\mathrm{ee}}[\boldsymbol{n}] - J[\boldsymbol{n}]. \tag{2.24}$$

Although the explicit formulation for the functional dependence of $E^{\mathrm{xc}}[\boldsymbol{n}]$ is unknown, successful approximations exist (some are discussed in the next section). On the other hand, we gain (due to the mapping) a much more convenient situation: The many-body problem in Eq. (2.13) is reduced to the problem of solving the single-particle Schrödinger equation[6]

$$\left[\left(-\frac{1}{2}\nabla^2 + \int\frac{n(\boldsymbol{r}')}{|\boldsymbol{r}-\boldsymbol{r}'|}d\boldsymbol{r}'\right)\mathbf{1} + \boldsymbol{V}^{\mathrm{KS}}(\boldsymbol{r})\right]\begin{pmatrix}\varphi^{\mathrm{KS}}_{i\uparrow}(\boldsymbol{r})\\ \varphi^{\mathrm{KS}}_{i\downarrow}(\boldsymbol{r})\end{pmatrix} = \epsilon_i\begin{pmatrix}\varphi^{\mathrm{KS}}_{i\uparrow}(\boldsymbol{r})\\ \varphi^{\mathrm{KS}}_{i\downarrow}(\boldsymbol{r})\end{pmatrix}. \tag{2.25}$$

The effective Kohn-Sham potential $\boldsymbol{V}^{\mathrm{KS}}$ of the one-particle electron system is given by the 2×2 matrix

$$V^{\mathrm{KS}}_{\alpha\beta}(\boldsymbol{r}) = \boldsymbol{v}^{\mathrm{ext}}_{\alpha\beta}(\boldsymbol{r}) + V^{\mathrm{xc}}_{\alpha\beta}(\boldsymbol{r}), \tag{2.26}$$

including the known contributions $\boldsymbol{v}^{\mathrm{ext}}$ and α,β representing the spins $\uparrow,\downarrow$. The unknown exchange-correlation potential is derived from the corresponding energy, Eq. (2.24), as

$$V^{\mathrm{xc}}_{\alpha\beta} = \frac{\delta E^{\mathrm{xc}}[\boldsymbol{n}(\boldsymbol{r})]}{\delta n_{\alpha\beta}(\boldsymbol{r})}. \tag{2.27}$$

Due to the construction of the auxiliary system, the electronic density matrix Eq. (2.16) can be expressed in terms of the introduced Kohn-Sham single-particle wave functions as

$$n_{\alpha\beta}(\boldsymbol{r}) = \sum_i^{N_e}\varphi^{\mathrm{KS}}_{i\alpha}(\boldsymbol{r})\varphi^{*\mathrm{KS}}_{i\beta}(\boldsymbol{r}). \tag{2.28}$$

Based on the variational principle Eq. (2.17), the Kohn-Sham formalism [Eqs. (2.21)-(2.28)] provides a practical recipe to compute the ground-state density and the total energy of the electronic subsystem for a given set of nuclei positions $\{\tilde{\boldsymbol{R}}_I\}$.

In principle the whole formalism is very general and applicable even to non-collinear spin systems, i.e., systems where the spin density matrix $\boldsymbol{n}(\boldsymbol{r})$ in Eq. (2.28) is not diagonal for all $\boldsymbol{r}$ in space. For these situations, the evaluation of Eq. (2.25) including Eq. (2.27) is not convenient for practical implementation due to the non-diagonal elements in $\boldsymbol{n}$. More important, the approximations for

[6] For the sake of clarity we use atomic units here.

E^{xc}, which enter (2.27), are commonly based on diagonal $\boldsymbol{n}$. Following Sandratskii *et al.* [30], the spin matrix can be locally diagonalized using the unitary transformation

$$\sum_{\alpha\beta} U_{i\alpha} n_{\alpha\beta} U^{+}_{\beta j} = \delta_{ij} n_i, \tag{2.29}$$

where $\boldsymbol{U}$ is given by the $S = 1/2$-rotation matrix

$$\boldsymbol{U} = \exp\left(\frac{1}{2} i\theta \boldsymbol{\sigma}_y\right) \exp\left(\frac{1}{2} i\phi \boldsymbol{\sigma}_z\right), \tag{2.30}$$

and θ, ϕ represent the spherical angles. To express Eq. (2.27) in terms of the (locally) diagonal n_i one uses [31]

$$\frac{\partial n_i}{\partial n_{\alpha\beta}} = U_{i\alpha} U^{+}_{\beta i}. \tag{2.31}$$

Employing the above relation, $V^{\mathrm{xc}}_{\alpha\beta}$ in Eq. (2.27) can be expressed in terms of the locally diagonal n_i as

$$V^{\mathrm{xc}}_{\alpha\beta} = \frac{\delta E^{\mathrm{xc}}}{\delta n_{\alpha\beta}} = \sum_{i=\uparrow,\downarrow} \frac{\delta E^{\mathrm{xc}}}{\delta n_i} \frac{\delta n_i}{\delta n_{\alpha\beta}} = \sum_{i=\uparrow,\downarrow} \frac{\delta E^{\mathrm{xc}}}{\delta n_i} U_{i\alpha} U^{+}_{\beta i}. \tag{2.32}$$

The single-particle Schrödinger equation, Eq. (2.25), can be rewritten in terms of the diagonal and non-diagonal part of the spin density. Therefore it is convenient to express the effective KS potential $\boldsymbol{V}^{\mathrm{KS}}$ in terms of the rotated Pauli-matrix,

$$\tilde{\boldsymbol{\sigma}}_z = \boldsymbol{U} \boldsymbol{\sigma}_z \boldsymbol{U}^{+} = \begin{pmatrix} \cos\theta & e^{-i\phi}\sin\theta \\ e^{i\phi}\sin\theta & -\cos\theta \end{pmatrix}, \tag{2.33}$$

as

$$\boldsymbol{V}^{\mathrm{KS}} = V_0 \mathbf{1} + \Delta V \tilde{\boldsymbol{\sigma}}_z \tag{2.34}$$

with diagonal terms

$$V_0 = v^{\mathrm{ext}} + \int \frac{n(\boldsymbol{r}')}{|\boldsymbol{r} - \boldsymbol{r}'|} d\boldsymbol{r}' + \sum_{i=\uparrow,\downarrow} \frac{\delta E^{\mathrm{xc}}}{\delta n_i}, \tag{2.35}$$

and mixing terms

$$\Delta V = \left(\frac{\delta E^{\mathrm{xc}}}{\delta n_\downarrow} - \frac{\delta E^{\mathrm{xc}}}{\delta n_\uparrow}\right). \tag{2.36}$$

This results in the general expression for the single-particle Schrödinger equation for non-uniform magnetic systems[7]

$$\left[(-\frac{1}{2}\nabla^2 + V_0)\mathbf{1} + \Delta V \tilde{\boldsymbol{\sigma}}_z\right] \begin{pmatrix} \varphi^{\mathrm{KS}}_{i\uparrow}(\boldsymbol{r}) \\ \varphi^{\mathrm{KS}}_{i\downarrow}(\boldsymbol{r}) \end{pmatrix} = \epsilon_i \begin{pmatrix} \varphi^{\mathrm{KS}}_{i\uparrow}(\boldsymbol{r}) \\ \varphi^{\mathrm{KS}}_{i\downarrow}(\boldsymbol{r}) \end{pmatrix}. \tag{2.37}$$

[7] Practically, one usually coarse grain the space $\boldsymbol{r}$ in a discrete mesh containing atomic spheres ν, i.e., $\theta(\boldsymbol{r}), \phi(\boldsymbol{r}) \to \theta^{\nu}, \phi^{\nu}$. This is justified in most cases, where the spin density is almost collinear within the atomic sphere ν and is vanishing outside.

Since V_0 as well as ΔV_0 depend only on the (locally) diagonal spin density matrices Eq. (2.29), the solution is much more straightforward [30] than solving Eqs. (2.25)-(2.27) directly.

Exchange-correlation Functionals

As pointed out above, the only remaining unknown part is the exchange-correlation (xc) functional E^{xc}, Eq. (2.24), for which several approximations have been proposed.

A well established approximation is the so called *local-spin-density approximation* (LSDA) which is based on the homogeneous electron gas model. It is assumed that the exchange-correlation energy per electron ϵ^{xc} at every coordinate $\boldsymbol{r}$ is a function of $n^{\uparrow}(\boldsymbol{r})$ and $n^{\downarrow}(\boldsymbol{r})$ at that point only, i.e., $\epsilon^{\mathrm{xc}}_{\mathrm{LSDA}} \equiv \epsilon^{\mathrm{xc}}_{\mathrm{LSDA}}(n^{\uparrow}(\boldsymbol{r}), n^{\downarrow}(\boldsymbol{r}))$ which results for the E^{xc} in the LSDA in[8]

$$E^{\mathrm{xc}}_{\mathrm{LSDA}}[n^{\uparrow}(\boldsymbol{r}), n^{\downarrow}(\boldsymbol{r})] = \int n(\boldsymbol{r}) \epsilon^{\mathrm{xc}}_{\mathrm{LSDA}}(n^{\uparrow}(\boldsymbol{r}), n^{\downarrow}(\boldsymbol{r})) d\boldsymbol{r}, \tag{2.38}$$

where $n^{\uparrow,\downarrow}$ represent the spin density of the spin-up/spin-down electrons and $n = n^{\uparrow} + n^{\downarrow}$.

The xc-energy $\epsilon^{\mathrm{xc}}_{\mathrm{LSDA}}$ can be further split into the exchange and correlation energy:

$$\epsilon^{\mathrm{xc}}_{\mathrm{LSDA}} = \epsilon^{\mathrm{x}}_{\mathrm{LSDA}} + \epsilon^{\mathrm{c}}_{\mathrm{LSDA}}. \tag{2.39}$$

For the homogeneous electron gas model the $\epsilon^{\mathrm{x}}_{\mathrm{LSDA}}$ can be derived analytically via Hartree-Fock theory [20] whereas for the remaining correlation part in $\epsilon^{\mathrm{c}}_{\mathrm{LSDA}}$ efficient parameterizations [32] based on highly accurate Quantum Monte Carlo calculations of the homogeneous electron gas exist [33].[9] Despite the simple character of Eq. (2.38), the LSDA provides (surprisingly) extremely accurate results.

However, as it turned out, one of the most famous deficiencies of the LSDA is that it predicts a nonmagnetic fcc ground state for iron (which is one of the key materials in the present study) instead of the experimentally observed ferromagnetic bcc state [34]. This issue was resolved by the introduction of the *generalized gradient approximation* (GGA) which accounts in addition for an explicit dependence of ϵ^{xc} on $\nabla n(\boldsymbol{r})$:

$$E^{\mathrm{xc}}_{\mathrm{GGA}}[\boldsymbol{n}(\boldsymbol{r})] = \int n(\boldsymbol{r}) \epsilon^{\mathrm{xc}}_{\mathrm{GGA}} \left(n^{\uparrow}(\boldsymbol{r}), n^{\downarrow}(\boldsymbol{r}), \nabla n^{\uparrow}(\boldsymbol{r}), \nabla n^{\downarrow}(\boldsymbol{r}) \right) d\boldsymbol{r}. \tag{2.40}$$

Among the different proposed GGA parameterizations (PBE, PBE0, rPBE, PW91, etc.), the PBE-GGA type is one of the most established ones and is employed in the present work.

Although the GGA turned out to improve various properties with respect to the LSDA, Eq. (2.40) does not allow to quantify the introduced error as well it is not *a priori* clear if it improves LSDA in principle. For selected applications in the present study, both functionals were used to estimate the intrinsic error within the approximations of the xc-functional.

[8] For the sake of clearness we present here the representation of the LSDA for collinear spin polarization (e.g. ferro-/anti-ferromagnets). The generalization to non-collinear spin polarization can be achieved by a local rotation of the coordinate system similar to Eq. (2.29) [see e.g. Ref. [31]].

[9] The parameterization performed in [32] are performed for the polarized system $\zeta = (n_{\uparrow} - n_{\downarrow})/n = 1$, the unpolarized system ($\zeta = 0$) and an interpolation in between as proposed by Barth and Hedin [9].

Bloch Theorem, Periodic Boundary Conditions, and Plane Wave Approach

The DFT formalism discussed above maps the problem of solving a system of interacting electrons onto an equivalent system of non-interacting electrons in an effective Kohn-Sham potential. Nevertheless, the amount of the effective KS wave functions φ^{KS} for the description of solids ($> 10^{23}$ per cubic cm) is much too high to be computationally handled. A drastic reduction of the required wave functions is obtained by taking the crystal symmetries into account. According to *Bloch's theorem*, the periodicity of a (external) potential $V^{\mathrm{ext}}(\boldsymbol{r}+\boldsymbol{R}) = V^{\mathrm{ext}}(\boldsymbol{r})$ with respect to a lattice translation $\boldsymbol{R}_n = \sum_i n_i \boldsymbol{a}_i$ in terms of multiple of the lattice unit vectors $\boldsymbol{a}_i$ is reflected in the wave functions of the electrons (also called *Bloch functions*):

$$\varphi^{\mathrm{KS}}_{i\boldsymbol{k}\alpha}(\boldsymbol{r}) = e^{\mathrm{i}\boldsymbol{k}\cdot\boldsymbol{r}} u_{i\boldsymbol{k}\alpha}(\boldsymbol{r}). \tag{2.41}$$

Here i denotes the band index, $\boldsymbol{k}$ a vector in the first Brillouin zone Ω_{BZ} and $u_{i\boldsymbol{k}\alpha}(\boldsymbol{r}) = u_{i\boldsymbol{k}\alpha}(\boldsymbol{r}+\boldsymbol{R})$ the lattice periodic part of the wave function. Since the single-particle Hamiltonian, the wave functions and hence all observables inhibit the translational invariance, solving the Schrödinger equation in the unit cell spanned by the $\boldsymbol{a}_i$ is sufficient to describe the whole translational periodic system.

Formulated differently, the problem of solving an infinite number of electrons occupying a finite number of states in an infinite crystal is transformed into the problem of solving a finite number of electrons in a finite cell, but occupying an infinite number of states ($\boldsymbol{k}$-points). This is reflected in the computation of the density

$$n(\boldsymbol{r}) = \sum_{\alpha=\uparrow,\downarrow} \sum_{i}^{\mathrm{occ}} |\varphi^{\mathrm{KS}}_{i\alpha}(\boldsymbol{r})|^2 = \frac{1}{\Omega_{\mathrm{BZ}}} \sum_{\alpha=\uparrow,\downarrow} \sum_{i}^{\mathrm{occ}} \int_{\mathrm{BZ}} |\varphi^{\mathrm{KS}}_{i\boldsymbol{k}\alpha}(\boldsymbol{r})|^2 d\boldsymbol{k}. \tag{2.42}$$

In practice, the integration over the infinite number of k-points in Ω_{BZ} is replaced by a discrete grid, and typically crystal symmetries are employed to reduce the computational effort. The explicit chosen number of k-points for the numerical integration in Eq. (2.42) has to ensure the desired convergence criteria and depends on the system under investigation.[10]

Although it is in principle possible to solve the unknown part of the wave function $u_{i\boldsymbol{k}\alpha}(\boldsymbol{r})$ directly numerically, it is more convenient to expand the latter first in an appropriate basis set. One of the most common approaches in solid state physics is the so called *plane-wave approach*. It is based on a plane-wave expansion of $u_{i\boldsymbol{k}\alpha}(\boldsymbol{r})$ as

$$u_{i\boldsymbol{k}\alpha}(\boldsymbol{r}) = \sum_{\boldsymbol{G}} c_{i,\boldsymbol{k}+\boldsymbol{G},\alpha} \exp[\mathrm{i}\boldsymbol{G}\cdot\boldsymbol{r}], \tag{2.43}$$

where $\boldsymbol{G}$ denotes the reciprocal lattice vectors. The expansion coefficients $c_{i,\boldsymbol{k}+\boldsymbol{G},\alpha}$ can be calculated by combining Eqs. (2.37), (2.41), and (2.43) as

$$\sum_{\boldsymbol{G}'} \left[\left(-\frac{1}{2}|\boldsymbol{k}+\boldsymbol{G}|^2 + V_0(\boldsymbol{G},\boldsymbol{G}') \right) \delta_{\boldsymbol{G}\boldsymbol{G}'} + \Delta V(\boldsymbol{G},\boldsymbol{G}')\tilde{\boldsymbol{\sigma}}_z \right] \begin{pmatrix} c_{i,\boldsymbol{k}+\boldsymbol{G},\uparrow} \\ c_{i,\boldsymbol{k}+\boldsymbol{G},\downarrow} \end{pmatrix} = \epsilon_{i\boldsymbol{k}} \begin{pmatrix} c_{i,\boldsymbol{k}+\boldsymbol{G},\uparrow} \\ c_{i,\boldsymbol{k}+\boldsymbol{G},\downarrow} \end{pmatrix}. \tag{2.44}$$

[10] For each material system under investigation, the explicit chosen parameters are given in the corresponding section.

The coefficients with small kinetic energy $\leq \frac{1}{2}|\boldsymbol{k}+\boldsymbol{G}|^2$ are typically more important than those with large kinetic energy [35]. In practice, the basis set Eq. (2.43) is therefore truncated at a certain cutoff value $\frac{1}{2}|\boldsymbol{k}+\boldsymbol{G}|^2 \leq E_{\text{cut}}$. The increase of E_{cut} yields to a consistently better description of the ground-state density. Therewith E_{cut} represents a very convenient *convergence parameter* to control the basis set and the error introduced due to the truncation within the plane wave approach. The controllability of the convergence parameters (i.e., in particular the cutoff energy) is one of the big advantages of the plane-wave basis set.

Summary

Let us briefly summarize this section. For a feasible solution of the many-body problem for the bulk system, Eq. (2.4), two major steps are required. First, the decoupling of the nuclei and magnetic degrees of freedom from the electronic motion. In order to compute the ground-state energy for a given (fixed) set of nuclei $\{\tilde{\boldsymbol{R}}_I\}$ and/or a given magnetic configuration (direction of spin density $\tilde{\boldsymbol{m}}$), the electronic Hamiltonian $\tilde{\mathcal{H}}^e$ in an effective potential, Eq. (2.13), has to be solved. This is possible by the introduction of the DFT reducing the problem to a minimization procedure for the ground-state spin density $\boldsymbol{n}_0$. The mapping onto an effective, auxiliary system of non-interacting electrons, the Kohn-Sham approach, reveals a practical recipe to perform this energy minimization, yielding $\boldsymbol{n}_0$ and the ground-state energy. The only remaining approximation is given by the treatment of the (unknown) exchange-correlation functional E^{xc}.

Ultimately, we are interested in a complete description of the Helmholtz free energy (2.3). In the next sections we discuss how the DFT computed properties for given constraints can be used as input data for finite temperature concepts.

2.2 Extension to Finite Temperatures

The methodology discussed so far provides an efficient first-principles scheme to compute *ground-state properties* at zero temperature. For the description of *finite temperature properties*, two challenges have to be accomplished:

(a) The description of finite temperature excitations within the Kohn-Sham DFT formalism.

(b) The contribution of these excitations to the thermodynamic properties.

Both tasks (a) and (b) represent a wide field of research on their own. We focus in the following in particular on the magnetic excitations. In the beginning, a brief overview of the different types of magnetic excitations (a) is given and several techniques to capture these excitations within the framework of DFT are introduced. For this purpose we discuss in particular the so called adiabatic spin dynamics.

The treatment of thermodynamic properties (b) is discussed afterwards. For this purpose the Heisenberg model is introduced and discussed in detail followed by different solution strategies. Finally, the concepts for the determination of vibronic and electronic excitations are shortly summarized.

2.2.1 Magnetic Excitations from DFT

The dominant magnetic excitation in ferromagnets are the so called (single-particle) Stoner excitations and the (collective) spin-wave excitations (see also Fig. 2.2). At low temperatures the

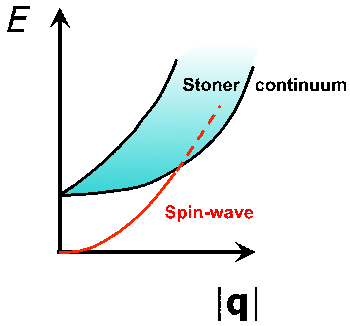

Figure 2.2: Sketch of Stoner continuum (shaded region) and spin-wave excitation spectrum (red line) for a strong ferromagnet.

spin-waves dominate the magnetic contribution to the thermodynamic properties. They are for instance responsible for the famous $T^{3/2}$ Bloch law for the magnetization in ferromagnets as well as for their $T^{3/2}$ contribution to the specific heat capacity at low T.

Going to higher temperatures, in addition single-particle spin-flip processes take place which also contribute to the thermodynamics of the system. These Stoner excitations are electron transitions between bands of opposite spin. For $\boldsymbol{q} \to 0$ the energy of such excitation corresponds to the exchange splitting energy (e.g., $\Delta_{\mathrm{ex}} = 1.5, 1.1$, and 0.3 eV for Fe, Co, and Ni, respectively [36]). At

high temperatures, the crossover of the spin-wave spectrum and Stoner continuum results in the damping of spin-waves.

A rigorous way to describe both types of excitations starting from the microscopic many-body problem is the determination of the dynamical spin susceptibility,

$$\chi_{ij}^{\alpha\beta}(\mathbf{r_i}, t_i; \mathbf{r}_j, t_j) = g\mu_B \frac{\partial \boldsymbol{m}^{\alpha}(\boldsymbol{r}_i, t_i)}{\partial \boldsymbol{B}^{\beta}(\boldsymbol{r}_j, t_j)}, \tag{2.45}$$

which describes the (time-dependent) response of the magnetization

$$\boldsymbol{m}^{\alpha}(\boldsymbol{r}, t) = g\mu_B \langle \boldsymbol{\sigma}^{\alpha} \rangle (\boldsymbol{r}, t) \tag{2.46}$$

under variation of a magnetic field $\boldsymbol{B_r}(t)$. In the above equation, $\alpha, \beta = (x, y, z, +, -)$ denote the index of the Pauli matrices including spin annihilation " $-$ " and creation " $+$ ", and $\boldsymbol{r}_i, \boldsymbol{r}_j$ represent the real space coordinates at times t_i, t_j, respectively. The collective excitations (including the interference with the Stoner continuum) can be readily obtained by the poles of the Fourier transformed transversal spin susceptibility $\chi^{+-}(\boldsymbol{q}, \omega)$.

A direct determination of the time-dependent response function Eq. (2.45) is, however, not possible within the framework of the time-independent DFT formalism introduced above. Two extensions to DFT turned out to allow a very accurate description of the dynamical susceptibility, namely the linear-response DFT [37] based on the time-dependent DFT (TDDFT) formalism [38] as well as the application of many-body perturbation theory (MBPT) (see e.g. [39]). Both methods are, compared to the *pure* DFT formalism, conceptually and computationally much more complex and expensive, respectively. We briefly expose in the following one of these concepts, namely the MBPT, to illustrate how $\chi_{ij}^{\alpha\beta}$ can be in principle addressed within the DFT framework. For a detailed review we refer to [40]. Starting point is the local spin density in Eq. (2.46),

$$\langle \boldsymbol{\sigma}_{\mathbf{r}_m}^{\alpha}(t_m) \rangle = -i \sum_{ij} \boldsymbol{\sigma}_{ij}^{\alpha} G_{ji}(\mathbf{r}_m, t_m; \mathbf{r}_m, t_m^+), \tag{2.47}$$

where t_m^+ indicates an infinitesimal increase of the time variable (to ensure proper time ordering). The single-particle Green's function is given by

$$G_{ij}(\mathbf{r}_1, t_1; \mathbf{r}_2, t_2) = \langle \langle a_i(\mathbf{r}_1, t_1); a_j^+(\mathbf{r}_2, t_2) \rangle \rangle \equiv G_{ij}(1, 2), \tag{2.48}$$

where $a_i^{\pm}(\mathbf{r}_m, t_m)$ denotes the creation ("+") or annihilation ("−") of an electron with spin i at time t_m and space $\mathbf{r}_m$. Using the short-hand notation introduced above, i.e., $1 = (\mathbf{r}_1, t_1)$, the single-particle Green's function of the full system $G_{ij}(1, 2)$ is determined by the Dyson equation (see e.g. [41]) as

$$G_{ij}(1,2) \quad = \quad G_i^0(1,2)\delta_{ij} + \sum_k \int\int G_i^0(1,3)\Sigma_{ik}(3,4)G_{kj}(4,2)d3d4, \tag{2.49}$$

where G_i^0 denotes the single-particle Green's function of the free (non-interacting) system and Σ the non-local and energy-dependent self-energy. The Kohn-Sham formalism directly provides via construction as a byproduct the eigenenergies ϵ_i and eigenfunctions ϕ_i^{KS} of the auxiliary (non-

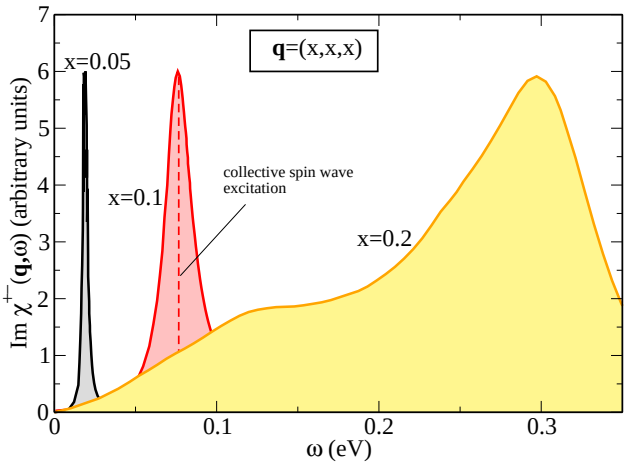

Figure 2.3: Transversal spin susceptibility $\chi^{+-}(\boldsymbol{q},\omega)$ of fcc Ni for different $\boldsymbol{q}$-vectors along the [1 1 1]-direction. For small $\boldsymbol{q}$-vectors the collective excitations are clearly dominating (sharp peaks). Due to the interference with the Stoner continuum (see also sketch in Fig. 2.2) the spin-wave excitation energies are smeared out at higher $\boldsymbol{q}$. The data are taken from [39].

interacting) Kohn-Sham system. Although they are strictly speaking no physical observables, as a first approximation a non-interacting DFT-KS Green's function G_{KS} can be defined. Therewith the single-particle excitations can directly be studied. To determine the collective excitations, access to the Green's function G_{ij} of the full, interacting system is, however, required. One of the key ingredients within a many-body-perturbation approach is therefore the self-energy Σ in Eq.(2.49). An established approach within the framework of DFT is the so called *GW* approximation [42]

$$\Sigma_{ij}(1,2) \approx iG_{ij}(1,2)W(1,2), \tag{2.50}$$

where W denotes the screened interaction. First-principles GW approaches have been successfully carried out since thirty years [40]. The second ingredient within a MBPT is the treatment of the electron-hole interaction which is well described by the Bethe-Salpeter equation via a functional derivative of Σ [40]. As an example we show in Fig. 2.3 the computed $\chi^{+-}(\boldsymbol{q},\omega)$ for fcc Ni and different $\boldsymbol{q}$ vectors. For small $\boldsymbol{q}$, the collective excitations are clearly pronounced by the sharp peak in $\chi^{+-}(\boldsymbol{q},\omega)$. For higher $\boldsymbol{q}$ and higher energies, the interference with the Stoner continuum (see Fig. 2.2) results in a broadening of the excitation spectrum emphasizing the importance of single-spin flip excitations in fcc Ni.

Considering the elementary ferromagnets Fe, Co, and Ni, very recent MBPT results by Şaşıoğlu *et al.* [39] reveal that the single-particle excitations in Fe and Co are in a large energy window negligible compared to the collective spin-wave excitations. These findings are in agreement with employment of the TDDFT by Savrasov in Ref. [37].

On the other hand, Stoner excitations are found to be much more significant in case of fcc Ni due to the much lower band-splitting [37, 39]. Focusing on the collective spin-wave excitations in Fe and Co, it is found that both approaches (TDDFT and MBPT) [37, 39] nicely agree with the so called adiabatic approximation [12, 43] which we discuss next.

Adiabatic Spin Dynamics from DFT

In the last decade most of the theoretical studies of magnetic excitations were based on an adiabatic treatment of the spin degree of freedom. The much slower motion of magnetic moments is separated from the faster electronic motion by mapping the many-body problem onto an effective Heisenberg model. In such an ansatz, the single-particle spin-flip excitations are neglected.

The derivation provided in the following is based on the adiabatic decoupling as given in [12, 43, 44]. We start by substituting $\Delta V \tilde{\boldsymbol{\sigma}}_z$ with $\boldsymbol{\sigma}\boldsymbol{B}^{\text{eff}}$ in Eq. (2.37),

$$\left[(-\frac{1}{2}\nabla^2 + V_0)\mathbf{1} + \boldsymbol{\sigma}\boldsymbol{B}^{\text{eff}}\right] \begin{pmatrix} \varphi^{\text{KS}}_{i\uparrow}(\boldsymbol{r}) \\ \varphi^{\text{KS}}_{i\downarrow}(\boldsymbol{r}) \end{pmatrix} = \epsilon_i \begin{pmatrix} \varphi^{\text{KS}}_{i\uparrow}(\boldsymbol{r}) \\ \varphi^{\text{KS}}_{i\downarrow}(\boldsymbol{r}) \end{pmatrix}, \tag{2.51}$$

which emphasizes an important point: The term $\boldsymbol{\sigma}\boldsymbol{B}^{\text{eff}}$ indicates that the spin-dependent part of the exchange-potential[11] (i.e. ΔV) acts like an *effective* magnetic field which is given by

$$\boldsymbol{B}^{\text{eff}}_{\boldsymbol{r}} = B^{\text{eff}}_{\boldsymbol{r}} \begin{pmatrix} \cos\phi_{\boldsymbol{r}} \sin\theta_{\boldsymbol{r}} \\ \sin\phi_{\boldsymbol{r}} \sin\theta_{\boldsymbol{r}} \\ \cos\theta_{\boldsymbol{r}} \end{pmatrix}, \tag{2.52}$$

with B^{eff} taking the role of ΔV i.e.

$$B^{\text{eff}}_{\boldsymbol{r}} := \Delta V_{\boldsymbol{r}}. \tag{2.53}$$

The spin-waves are caused by the time-dependent motion of the magnetization $\boldsymbol{m}_{\boldsymbol{r}}(t)$ at each point in space $\boldsymbol{r}$ as function of time t. To solve the equation of motion for the time-dependent magnetization we have in principle to solve the full time-dependent Schrödinger equation to obtain $\boldsymbol{n}_{\boldsymbol{r}}(t)$ and hence $\boldsymbol{m}_{\boldsymbol{r}}(t) = \text{Tr}\,(\boldsymbol{\sigma}\boldsymbol{n}_{\boldsymbol{r}}(t))$. A full time-dependent DFT would render the current study to be infeasible.

Since the motion of $\boldsymbol{m}_{\boldsymbol{r}}(t)$ (spin-waves $\sim$ meV) is much slower than the electronic motion ($\sim$ eV) it is justified to use an adiabatic approach similar to the decoupling of the nuclei and electronic motion (Born-Oppenheimer approximation in Sec. 2.1.1). This implies that the electrons follow the time-dependent change of $\boldsymbol{m}_{\boldsymbol{r}}(t)$ instantaneously.

The main assumption is that the time-dependent Schrödinger equation holds also in the framework of DFT in the adiabatic approximation [38], i.e.,

$$i\frac{\partial}{\partial t} \begin{pmatrix} \varphi^{\text{KS}}_{i\uparrow} \\ \varphi^{\text{KS}}_{i\downarrow} \end{pmatrix} = \left[(-\frac{1}{2}\nabla^2 + V_0)\mathbf{1} + \boldsymbol{\sigma}\boldsymbol{B}^{\text{eff}}\right] \begin{pmatrix} \varphi^{\text{KS}}_{i\uparrow} \\ \varphi^{\text{KS}}_{i\downarrow} \end{pmatrix}. \tag{2.54}$$

The equation above describes the time evolution of the spinor components $\varphi^{\text{KS}}_{i\uparrow}$ and $\varphi^{\text{KS}}_{i\downarrow}$. Solving this equation yields the spin density $\boldsymbol{n}_{\boldsymbol{r}}(t)$ and hence the time dependence of the magnetization density via

$$\frac{\partial}{\partial t}\boldsymbol{m}_{\boldsymbol{r}} = \text{Tr}\boldsymbol{\sigma}\frac{\partial}{\partial t}\boldsymbol{n}_{\boldsymbol{r}}. \tag{2.55}$$

[11] We remind that V_0 includes the spin-independent part of the exchange-correlation potential, see Eq. (2.35).

Using Eq. (2.54) and some algebra (see e.g. [31]) one gets a rather simple form[12],

$$\frac{\partial}{\partial t}\boldsymbol{m}_{\boldsymbol{r}} = -2\boldsymbol{m}_{\boldsymbol{r}} \times \boldsymbol{B}^{\text{eff}}_{\boldsymbol{r}}, \tag{2.56}$$

for the motion of the magnetization density.

Above equation could be identified with the famous (classical) *Landau-Lifshitz Equation* which was introduced by Landau and Lifshitz already in 1935 to model the precessional motion of the magnetization under an (effective) magnetic field $\boldsymbol{B}^{\text{eff}}$ [45].[13] In our case, the effective field $\boldsymbol{B}^{\text{eff}}$ is caused by the spin-dependent part of the exchange-correlation potential, Eqs. (2.52) and (2.53).

If we assume the z-axis as a global quantization axis $\theta_{\boldsymbol{r}} \equiv \theta$ (which is in absence of magnetic anisotropy possible), an ansatz fulfilling the differential equation (2.56) is given by

$$\boldsymbol{m}_{\boldsymbol{r}}(t) = m_{\boldsymbol{r}} \begin{pmatrix} \cos\phi_{\boldsymbol{r}}(t)\sin\theta \\ \sin\phi_{\boldsymbol{r}}(t)\sin\theta \\ \cos\theta \end{pmatrix}, \tag{2.57}$$

where θ denotes the time- and location-independent polar (cone) angle and $\phi_{\boldsymbol{r}}(t)$ the time-dependent azimuthal angle at every point in the crystall $\boldsymbol{r}$.

In principle, the magnetization direction $\boldsymbol{m}_{\boldsymbol{r}}(t)/|\boldsymbol{m}_{\boldsymbol{r}}(t)|$ as well as the effective field $\boldsymbol{B}^{\text{eff}}_{\boldsymbol{r}}$ may vary in every point in space $\boldsymbol{r}$. However, for most practical calculations $\boldsymbol{m}_{\boldsymbol{r}}(t)$ is in a good approximation collinear within the atomic spheres Ω_ν of each atom ν [31]. One can therefore proceed by coarse graining $\boldsymbol{m}_{\boldsymbol{r}}(t)$ and introducing an *effective* point magnetic moment $\boldsymbol{M}_\nu$ located at the position $\boldsymbol{R}_\nu$ of every atom ν,

$$\boldsymbol{M}_\nu = \int_{\Omega_\nu} \boldsymbol{m}_{\boldsymbol{r}} d\boldsymbol{r}. \tag{2.58}$$

The above mapping of the magnetization onto effective local (point) moments allows one to define the spin quantum number via

$$|\boldsymbol{M}_\nu| = M_\nu = g\mu_{\text{B}} S_\nu \tag{2.59}$$

with the Landé factor $g \approx 2$ and the Bohr magneton μ_{B}.

By taking the lattice symmetry into account we can define $\phi_{\boldsymbol{r}}(t)$ in Eq. (2.57) as

$$\phi_{\boldsymbol{r}}(t) \rightarrow \phi_\nu(t) = \omega t + \boldsymbol{q}\boldsymbol{R}_\nu. \tag{2.60}$$

The so called *spin spiral* characterized by Eqs. (2.57)-(2.60) is illustrated in Fig. 2.4. All moments $\boldsymbol{M}_\nu$ rotate with a fixed magnitude (projection) around the z-axis (determined by a fixed cone angle θ). At each time t, the azimuthal angle $\phi_\nu(t)$ at atom ν is determined by a wave vector $\boldsymbol{q}$, Eq. (2.60). Since the situation sketched in Fig. 2.4 appears like a snapshot of a frozen spin-wave, this approach is sometimes also referred to as *frozen magnon approach*.

The total energies of the such constructed spin spirals can be associated with the spin-wave energy. To identify the total energy calculations with the spin-wave energy we assume a ferromag-

[12] Terms which can be related to the change of the orbital contribution of the magnetization are neglected since we are interested in the spin part only [31].

[13] Actually, Landau and Lifshitz treated a more general case of Eq. (2.56) including a damping factor.

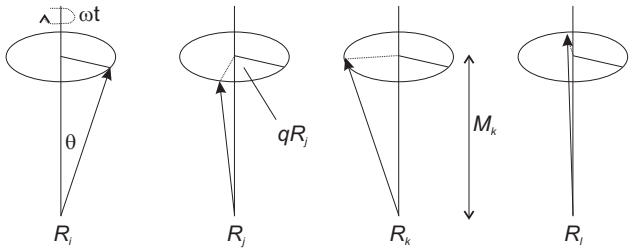

Figure 2.4: Sketch of a spin spiral Eq. (2.57).

netic system, which is perturbed by a change of the direction of the magnetic moments $\boldsymbol{M}_\nu$. The resulting energy change ΔE can be expressed as

$$\Delta E = \sum_{\alpha\beta} J^{\mathrm{CL}}_{\alpha\beta} \boldsymbol{M}_\alpha \boldsymbol{M}_\beta \tag{2.61}$$

which is exactly the *classical* solution of the Heisenberg model (the model will be discussed in detail afterwards). The perturbation ΔE gives rise to an effective field $\boldsymbol{B}_\nu$ in every atomic sphere ν,

$$\boldsymbol{B}_\nu = -\frac{\Delta E}{\partial \boldsymbol{M}_\nu} = -2 \sum_{\beta} J^{\mathrm{CL}}_{\alpha\beta} \boldsymbol{M}_\beta. \tag{2.62}$$

Assuming a small perturbation ($\theta \to 0$) and combining Eqs. (2.56) and (2.57)-(2.62), one ends up with

$$\omega^{\mathrm{DFT}}_{\boldsymbol{q}} = 4 \sum_{\beta} J^{\mathrm{CL}}_{\alpha\beta} M_\beta \left(e^{i\boldsymbol{q}(\boldsymbol{R}_\alpha - \boldsymbol{R}_\beta)} - 1 \right) = \frac{4}{M} (\tilde{J}_{\boldsymbol{q}} - \tilde{J}_{\boldsymbol{0}}), \tag{2.63}$$

where we assumed in the last step a homogeneous magnetization $M \equiv M_\beta$ and absorbed M in the effective exchange coefficients $J^{\mathrm{CL}} M^2 = \tilde{J}$.[14]

For finite cone angles θ, ΔE is given as

$$\Delta E(\boldsymbol{q}, \theta) = \sin^2 \theta (\tilde{J}_{\boldsymbol{q}} - \tilde{J}_{\boldsymbol{0}}). \tag{2.64}$$

Thus the dispersion $\omega^{\mathrm{DFT}}_{\boldsymbol{q}}$ Eq. (2.63) reads as [12, 31]

$$\omega^{\mathrm{DFT}}_{\boldsymbol{q}} = \frac{4}{M} \lim_{\theta \to 0} \frac{\Delta E(\boldsymbol{q}, \theta)}{\sin^2 \theta}. \tag{2.65}$$

This is one of the key expressions which links the total ground state energies of different spin spirals (obtained employing the DFT formalism) with the magnetic spin-wave excitations. Furthermore, Eqs. (2.64)-(2.65) allow one to extract directly effective exchange coefficients $\tilde{\boldsymbol{J}}$, which could be further used to derive other (thermodynamic) magnetic properties.

Before concluding this section we note one important point for the practical evaluation of Eq. (2.65). This concerns the choice of the cone angle θ. From a physical point of view, it should

[14] For the sake of simplicity the derivation is shown for single-species systems. The extension to multi-species systems is, however, straightforward, see e.g. [12, 31].

be as small as possible since spin-waves are small perturbations from the ground state. Because for small cone angles the total energy ΔE goes to zero as $\sin^2\theta$ [Eq. (2.64)], calculations are carried out at a finite θ, which provides sufficient large energy differences ΔE within a reasonable choice of technical convergence parameters (such as cutoff energy, k-point grid, etc). Apart from this rather technical aspect, the "best" choice of the cone angle for some applications is still debated [46, 47]. For the determination of high temperature properties such as T_C, some works suggest [47] to employ larger cone angles since they may better mimic the situation at high T (paramagnetic regime). We will discuss this point in more detail for a realistic material system (namely bcc iron) and also the impact of the choice of θ on T_C. However, we would like to note already here that for strong ferromagnets (large exchange splitting) such as bcc iron, the actual choice of θ is rather uncritical. This has been shown in Refs. [12, 48] and very recently by Kübler [44]. In fact, already the use of planar spin spirals (the limit case $\theta = \pi/2$), i.e.

$$\omega_{\boldsymbol{q}}^{\mathrm{DFT}} = \frac{4}{M}\Delta E(\boldsymbol{q}, \pi), \tag{2.66}$$

allows reliable predictions [43, 44].

Another point concerns the computation of incommensurable (wrt. the unit cell) spin spiral structures. In this case, the "conventional" translational invariance (Bloch theorem) is broken for translations non-orthogonal to $\boldsymbol{q}$. However, the atoms separated by a lattice translation are still equivalent apart from the rotated local moments (if we neglect the small lattice anisotropy due to spin orbit coupling). Transformations combining a translation (by $\boldsymbol{R}_n$) *and* a rotation (by $\boldsymbol{q}\cdot\boldsymbol{R}_n$) leave the spiral structure invariant and provide a very elegant way to treat spin spirals. Following Sandratskii [49], this can formally be expressed by a generalized translation $\mathcal{T}_n$ which includes the translation $\boldsymbol{R}_n$ and the spin rotation U [Eq. (2.30)], and commutes with the Hamiltonian:

$$\mathcal{T}_n\mathcal{H}(\boldsymbol{r})\varphi(\boldsymbol{r}) = \mathcal{H}(\boldsymbol{r})U(-\boldsymbol{q}\boldsymbol{R}_n)\varphi(\boldsymbol{r}+\boldsymbol{R}_n). \tag{2.67}$$

In analogy to Bloch's Theorem the eigenstates can be chosen as

$$\mathcal{T}_n\varphi_{i\boldsymbol{k}}(\boldsymbol{r}) = U(-\boldsymbol{q}\boldsymbol{R}_n)\varphi_{i\boldsymbol{k}}(\boldsymbol{r}+\boldsymbol{R}_n) = e^{\mathrm{i}\boldsymbol{k}\cdot\boldsymbol{R}_n}\varphi_{i\boldsymbol{k}}(\boldsymbol{r}). \tag{2.68}$$

The lattice periodic part of the eigenstates above follows the chemical lattice (via $\boldsymbol{R}_n$). This implies that spin spirals can be computed in the chemical unit cell, which drastically reduces the computational effort, or even makes the computation of *incommensurable* spiral structures possible in first place. Further reduction of the computational effort is possible if the perturbation is small (small $\boldsymbol{q}$ vectors and cone angles θ). In this limit, the magnetic force theorem [15] can be applied allowing to reduce the computational costs as well.

The effective spin S_ν (2.59) and the effective exchange coefficients $\tilde{\boldsymbol{J}}$ (2.63)-(2.65) completely determine the Heisenberg model which we discuss next. Therefore, we have all ingredients in hands to study the thermodynamic properties of magnetic materials based on first-principles results.

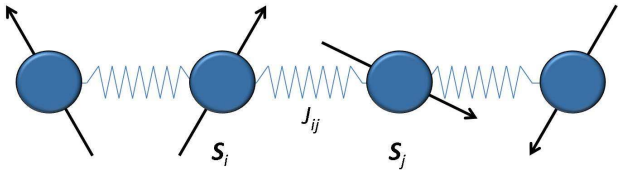

Figure 2.5: Sketch of the Heisenberg model Eq. (2.70). Exchange interaction J_{ij}^{QM} between spins $\boldsymbol{S}_i$ and $\boldsymbol{S}_j$ localized at lattice sites $\boldsymbol{R}_i$ and $\boldsymbol{R}_j$.

2.2.2 The Heisenberg Model

The frozen magnon approach based on the adiabatic spin dynamics discussed in the previous section allows us to map the complex many-body problem onto a more simple, *effective* magnetic Hamiltonian. Explicitly, we have introduced in Eq. (2.61) the *classical* formulation of the *Heisenberg model*.[15]

Originally, the model was proposed to study the magnetism caused by localized moments (e.g. due to partially filled electron shells, such as e.g. EuO or EuS). The *quantum-mechanical* Hamiltonian is given by

$$\mathcal{H} = -\sum_{ij} J_{ij}^{\mathrm{QM}} \boldsymbol{S}_i \boldsymbol{S}_j, \tag{2.70}$$

with exchange coefficients J_{ij}^{QM}, which mediate the magnetic exchange between spins $\boldsymbol{S}_i$ localized at lattice sites i and j. The $\boldsymbol{S}_i$ denote the spin operators obeying the usual commutator rules for orbital moments and having discretized eigenvalues. The Heisenberg model should be interpreted as an *effective* operator simulating the Coulomb interaction via the spin-spin interaction $\boldsymbol{S}_i \cdot \boldsymbol{S}_j$. Although originally designed to describe the situation of ideal localized moments, the model has been successfully[16] applied to magnetic metals showing *strongly* (but not ideally) localized magnetic moments (such as Fe and Co) see e.g. [15, 16, 43, 48, 54].

[15] For the sake of completeness we mention here also two other famous magnetic model Hamiltonians. The first one is the so called Hubbard model which is supposed to describe in particular itinerant magnetic materials. These are systems where both phenomena, conductivity and magnetism, are caused by the same group of (itinerant) electrons. It is therefore in particular well suited to account for the single-particle Stoner excitations. The *Hubbard model* was proposed in 1963 by Hubbard [50], Gutzwiller [51] and Kanamori [52]:

$$\mathcal{H} \quad = \quad \sum_{ij\sigma} T_{ij} a_{i\sigma}^{+} a_{j\sigma} + \frac{U_{\mathrm{Hub}}}{2} \sum_{i\sigma} n_{i\sigma} n_{i-\sigma}. \tag{2.69}$$

Here, $a_{i\sigma}^{+}$ ($a_{i\sigma}$) denotes the creation-(annihilation-) operator of an electron having spin $\sigma = \uparrow, \downarrow$. T_{ij} is the hopping integral between lattice sites $\mathbf{R}_i$ and $\mathbf{R}_j$. The operator $n_{i\sigma} = a_{i\sigma}^{+} a_{i\sigma}$ denotes the occupation number operator and U_{Hub} (also called *Hubbard-U*) represents a simplified version of the Coulomb interaction energy between the electrons, which is reduced to a local, intra-atomic interaction. The lattice information is effectively included in the T_{ij}. The Hubbard model allows hence to study the interplay between kinetic energy, Coulomb interaction and lattice structure under the Pauli principle.

Another famous magnetic model was proposed for systems where two different groups of electrons are responsible for the magnetism and the conductivity. A prototype is the 4f-system Gd. Here, the itinerant electrons can interact with the localized spin system. The appropriate model is called *Kondo-lattice model* [53].

[16] We note that this holds only true if one is interested in the magnetic properties of these materials and not in the interplay of, e.g., conductivity and magnetism.

The subscript "QM" underlies that the above representation is a *quantum* model. In fact, we will show in Sec. 3.2.2 explicitly that the quantum effects, neglected by the classical formulation (2.61), are mandatory for an accurate description of thermodynamic properties. The solution of the quantum model is, however, not that straightforward.

Before discussing different solution techniques we use the opportunity to deepen the concept of spin-waves. Up to now they were phenomenologically introduced as small perturbations ("spin spirals") from the ferromagnetic ground state. This results finally in the expression (2.65), which combines the total energy calculations $\Delta E(\boldsymbol{q},\theta)$ with the excitation energy $\omega_{\boldsymbol{q}}^{\mathrm{DFT}}$. We provide in the following a more formal approach to the spin-wave concept.

Spin-waves

To show that spin-waves are the natural eigensolutions of the Heisenberg model it is convenient to express Eq. (2.70) in terms of raising (lowering) operators $S_i^{\pm} = S_i^x \pm i S_i^y$ as

$$\boldsymbol{S}_i \cdot \boldsymbol{S}_j = S_i^x S_j^x + S_i^y S_j^y + S_i^z S_j^z = \frac{1}{2}(S_i^+ S_j^- + S_i^- S_j^+) + S_i^z S_j^z, \tag{2.71}$$

where the z-axis is chosen as the quantization axis.[17]

After Fourier transformation,

$$S_{\boldsymbol{q}}^{\sigma} = \sum_i e^{-i\boldsymbol{q}\boldsymbol{R}_i} S_i^{\sigma}, \qquad (\sigma = +,-,z) \tag{2.72}$$

$$J_{\boldsymbol{q}}^{\mathrm{QM}} = \frac{1}{N}\sum_{ij} J_{ij}^{\mathrm{QM}} e^{i\boldsymbol{q}(\boldsymbol{R}_i - \boldsymbol{R}_j)}, \tag{2.73}$$

the Hamiltonian can be expressed in $\boldsymbol{q}$-space as

$$\mathcal{H} = -\frac{1}{N}\sum_{\boldsymbol{q}} J_{\boldsymbol{q}}^{\mathrm{QM}} \left(S_{\boldsymbol{q}}^+ S_{-\boldsymbol{q}}^- + S_{\boldsymbol{q}}^z S_{-\boldsymbol{q}}^z\right) - \frac{1}{\hbar} g\mu_B B_0^z S_{\boldsymbol{0}}^z. \tag{2.74}$$

Denoting the ground state (ferromagnetic solution) as $|0\rangle$ one can show (see e.g. [56]) that

$$|\boldsymbol{q}\rangle = \frac{1}{\hbar\sqrt{2SN}} S_{\boldsymbol{q}}^- |0\rangle \tag{2.75}$$

is a (normalized) eigenstate of (2.74) with an eigenenergy given by

$$\hat{E}_{\boldsymbol{q}} = E_0 + E_{\boldsymbol{q}}, \tag{2.76}$$

where

$$E_0 = -N J_{\boldsymbol{0}} \hbar^2 S^2 - N_g \mu_B B_0^z \tag{2.77}$$

[17] In high symmetric 3D systems the magnetic lattice anisotropy due to spin-orbit coupling as well as the dipolar anisotropy is at least one order of magnitude smaller than the exchange interaction J and is therefore neglected in the present study. We note, however, that these anisotropies are crucial in low dimension, in particular to realize finite magnetization in 2D films (Mermin Wagner theorem [55]).

denotes the ground-state energy.
The energy

$$E_{\boldsymbol{q}} = g\mu_B B_0^z + 2S\hbar^2 \left(J_{\boldsymbol{0}}^{\mathrm{QM}} - J_{\boldsymbol{q}}^{\mathrm{QM}} \right) \tag{2.78}$$

is interpreted as the excitation energy of one magnon. From the Zeeman term one directly recognizes that the total moment of the system is reduced by $g\mu_B$. The quasiparticle has therefore the spin 1, i.e. magnons are bosons.

The expectation value of the lattice site dependent magnetization,

$$\langle \boldsymbol{q} | S_i^z | \boldsymbol{q} \rangle = \langle S_i^z \rangle = \hbar \left(S - \frac{1}{N} \right), \tag{2.79}$$

reveals an astonishing outcome: the spin deviation is lattice site independent! This directly implies the concept of a spin-wave: The spin deviation Eq. (2.79) is uniformly distributed over the whole lattice and characterized by a wave vector $\boldsymbol{q}$. Expressed differently, the local spins at each lattice site $\boldsymbol{S}_i$ process around the z-axis with a *fixed* projection onto the z-axis. In the thermodynamic limit $N \to \infty$, the cone angle θ, determining the deviation from the z-axis in Eq. (2.65), goes to zero.

Since at $T = 0$ K the classical and quantum solution of the ferromagnetic Heisenberg model are identical, one can formally derive Eq. (2.65) by postulating $J^{QM} S^2 \equiv \tilde{J}$ and $S \equiv 2M$ i.e. $g \approx 2$ in Eq. (2.59).

2.2.3 Thermodynamic Properties

Having introduced the magnetic model Hamiltonian (2.70) and underlying DFT methodology to extract the required model parameters, we can proceed in deriving finite temperature properties. For this purpose an important quantity is the internal energy $U(T,V) = \langle \mathcal{H} \rangle (T,V)$ of the system. It is directly connected to the specific heat capacity via

$$C_V(T) = \left. \frac{dU}{dT} \right|_V, \tag{2.80}$$

which is in turn related to the entropy via the integration

$$S_V(T) = \int_0^T C_V(T')/T' dT'. \tag{2.81}$$

Combining (2.80) and (2.81), one can derive an expression for the Helmholtz free energy solely[18] depending on $U(T,V)$ [56]

$$F^{\mathrm{mag}}(T,V) = U(0,V) - T \int_0^{T'} dT' \frac{U(T',V) - U(0,V)}{T'^2}. \tag{2.82}$$

However, a numerical or analytical exact solution for $\langle \mathcal{H} \rangle (T,V)$ is in general not feasible. Providing efficient approaches for $\langle \mathcal{H} \rangle (T,V)$ is therefore one of the key concerns in the present study.

[18] Eq. (2.82) is, strictly speaking, only valid for systems providing a unique ground state, e.g., a perfect crystal lattice.

To prepare this we discuss next different solution techniques which are commonly used to determine thermodynamic properties.

Analytic Approaches

We start by introducing two analytical approaches which are commonly used to determine the Curie temperature T_C.

For an analytical treatment it is convenient to start from the Heisenberg model in the formulation of raising/lowering operators as in Eq. (2.74), i.e.

$$\mathcal{H} \quad = \quad -\sum_{ij} J_{ij}^{\mathrm{QM}} (S_i^+ S_j^- + S_i^z S_j^z). \tag{2.83}$$

To obtain a solution for T_C, we investigate the average magnetization, i.e. $\langle S_z \rangle(T)$, which vanishes as the temperature approaches the Curie temperature, $\langle S_z \rangle(T_C) \to 0$.

A rather simple but often successful approach is the mean field (MF) or often called molecular field approximation. Essentially, fluctuations of the observables A, B around their mean values $\langle A \rangle, \langle B \rangle$ are neglected in MF, i.e. explicitly

$$(A - \langle A \rangle)(B - \langle B \rangle) \quad \to \quad 0. \tag{2.84}$$

Therewith Eq. (2.83) becomes:

$$\mathcal{H}_{\mathrm{MF}} \quad = \quad J_{\mathbf{0}}^{\mathrm{QM}} \langle S^z \rangle_{\mathrm{MF}}^2(T) - B_{\mathrm{MF}}(T) \sum_i S_i^z. \tag{2.85}$$

Physically, spin operator products are now decoupled reducing the Hamiltonian to the one of an ideal paramagnet [56] under an "effective" (mean) field

$$B_{\mathrm{MF}}(T) \quad := \quad 2 J_{\mathbf{0}}^{\mathrm{QM}} \langle S^z \rangle_{\mathrm{MF}}(T), \tag{2.86}$$

caused by the exchange interaction J_{ij}^{QM} between all spins, $J_{\mathbf{0}}^{\mathrm{QM}} = 1/N \sum_{ij} J_{ij}^{\mathrm{QM}}$ according to (2.73).

Based on Eq. (2.85) it is straightforward to derive the reduced magnetization (see A.1 for a detailed derivation):

$$m_{\mathrm{MF}}(T) = \langle S^z \rangle_{\mathrm{MF}} / S \quad = \quad B_S \left(\frac{2S^2 J_{\mathbf{0}}^{\mathrm{QM}}}{k_B T} \frac{\langle S^z \rangle_{\mathrm{MF}}}{S} \right), \tag{2.87}$$

where the Brillouin function $B_S(x)$ is defined as

$$B_S(x) \quad := \quad \frac{2S+1}{2S} \coth \left(\frac{2S+1}{2S} x \right) - \frac{1}{2S} \coth \left(\frac{x}{2S} \right). \tag{2.88}$$

The limit $T \to T_C$ implies $x \sim \langle S_z \rangle \to 0$ in Eq. (2.88) and we can expand the Brillouin function:

$$B_S(x) \xrightarrow{x \to 0} \frac{S+1}{3S} x + \mathcal{O}(x^3). \tag{2.89}$$

Combining Eqs. (2.87) and (2.89) we obtain the expression for the mean field critical temperature:

$$k_B T_C^{\mathrm{MF}} = \frac{2}{3} S(S+1) J_{\mathbf{0}}^{\mathrm{QM}} = \frac{2}{3} \tilde{J}_0. \tag{2.90}$$

In Eq. (2.90) we have introduced the effective exchange parameter for the quantum model, i.e.

$$S(S+1) J^{\mathrm{QM}} = \tilde{J}. \tag{2.91}$$

One has to note that there is no "strict" mapping between the classical and quantum model [57]. Another choice would be $S^2 J^{\mathrm{QM}} = \tilde{J}$ similar as done for the classical formulation which does, however, not account for the quantum nature of the spins. In contrast to this, the definition above is rooted in the quantum nature of the spin operators $\hat{S}$, i.e. due to the eigenvalue relation of angular momentum operators $\hat{S}^2|S\rangle = S(S+1)|S\rangle$. Such a definition of effective exchange coefficients is useful in particular when results of the classical and quantum solution are compared [57, 58], since thermodynamic quantities approximately scale in the quantum case as $S(S+1)$.[19]

Obviously, the simple character of the MF approximation reveals some shortcomings. Having spin conservation at each lattice site in mind, i.e. $\langle S_{i+}\rangle = \langle S_{i-}\rangle \equiv 0$, the spin flip terms in the Hamiltonian (2.83) were neglected by the mean field ansatz

$$\langle S_i^+ S_j^-\rangle \xrightarrow{\mathrm{MF}} 0. \tag{2.92}$$

This means that also the fundamental spin-wave excitations are suppressed in the MF ansatz. In addition short-range order is fully neglected since in the paramagnetic regime $T \geq T_C$ (where the total magnetization goes to zero $\langle S^z\rangle \to 0$), the MF Hamiltonian Eq. (2.85) vanishes, $\mathcal{H}_{\mathrm{MF}} \to 0$. Although it is well known that the mean field solution Eq. (2.90) overestimates T_C, it usually provides (at least qualitatively) a good prediction of some physical trends [17, 60].

A more sophisticated approach, which includes the collective (spin-wave) excitations, is given by the following Green's function (GF) based formalism. The main idea is to use appropriate GFs to access correlation functions which determine the magnetization. We now discuss a first order GF decoupling procedure which is known to provide a reliable prediction of T_C, even on a *quantitative* level. We start with the following operator identity

$$\langle S_i^- S_i^+\rangle = \hbar^2 S(S+1) + \hbar\langle S_i^z\rangle - \langle (S_i^z)^2\rangle. \tag{2.93}$$

In order to compute the magnetization $\langle S_i^z\rangle$ on the right hand side of this equation, we need to determine the correlation function $\langle S_i^- S_i^+\rangle$ as well as the higher order moment $\langle (S_i^z)^2\rangle$. Following the formalism proposed by Callen in 1963 [61], both can be obtained by the following GF

$$G_{ij}^{(a)} = \langle\langle S_i^+; B_j^{-(a)}\rangle\rangle := \langle\langle S_i^+; e^{aS_{jz}} S_j^-\rangle\rangle. \tag{2.94}$$

[19] The critical temperature within the quantum case does not strictly follow $T_C(S) \sim J^{\mathrm{QM}} S(S+1)$ as was, e.g., recently shown using high temperature series expansion [59]. The complex dependence of $T_C(S)$ is, however, beyond the scope of this work and we use (2.91) instead.

The above introduced parameter a allows in a very elegant way to determine $\langle (S_i^z)^n \rangle$ for various n. The equation of motion for $G_{ij}^{(a)}$ is given by

$$EG_{ij}^{(a)}(E) = \hbar\langle [S_i^-; B_j^{+(a)}]_- \rangle + \langle\langle [S_i^-, \mathcal{H}]_-; B_j^{+(a)} \rangle\rangle_E. \tag{2.95}$$

A direct solution of $G_{ij}^{(a)}$ is impractical due to the higher order GFs on the right hand side, which appear due to the commutator $[S_i^-, \mathcal{H}]_-$. To overcome this, the higher order GFs are typically decoupled on a certain level. The Tyablikov decoupling, as proposed by Tyablikov in 1959 [18], or also called random phase approximation (RPA), is given by the first order *decoupling* of the higher order Green's function on the right hand side. Explicitly, the GFs are decoupled such as

$$\langle\langle S_m^+ S_i^z; S_j^- \rangle\rangle_E \quad \overset{RPA}{\longrightarrow} \quad \langle S_i^z \rangle \langle\langle S_m^+; S_j^- \rangle\rangle_E \tag{2.96}$$

$$\langle\langle S_i^+ S_m^z; S_j^- \rangle\rangle_E \quad \overset{RPA}{\longrightarrow} \quad \langle S_m^z \rangle \langle\langle S_i^+; S_j^- \rangle\rangle_E. \tag{2.97}$$

Physically, this corresponds to the assumption that the z-component of the magnetization $\langle S_i^z \rangle$ is not strongly correlated to the surrounding and hence its fluctuations are small. This holds true at very low temperatures (close to the ground state) as well as at very high temperatures where the thermal induced randomization dominates over the correlation due to the exchange interaction. An important outcome is that the results of the RPA agree with non-interacting spin-wave theory at low temperatures as well as statistical theory at high temperatures (series expansion technique) [18, 62]. For this reason, the RPA is assumed to provide a reasonable description also between these limits. Indeed it is found that despite the simple character of the approximation, the RPA procedure describes the transversal correlation function $\langle S_i^+ S_j^- \rangle$ satisfactory over the entire temperature range [63].

Using above decouplings [Eqs. (2.96) and (2.97)] it is possible to solve Eq. (2.95) and to derive the magnetization (a full derivation is given in A.2) as

$$\langle S^z \rangle^{\mathrm{RPA}} = \frac{(1+\varphi)^{2S+1}(S-\varphi) + \varphi^{2S+1}(S+1+\varphi)}{(1+\varphi)^{2S+1} - \varphi^{2S+1}}, \tag{2.98}$$

with the effective magnon occupation number

$$\varphi = \frac{1}{N} \sum_{\boldsymbol{q}} \frac{1}{e^{\beta E(\boldsymbol{q})} - 1} \tag{2.99}$$

and effective magnon energies

$$E_{\boldsymbol{q}} = 2\hbar \langle S^z \rangle^{\mathrm{RPA}} (J_0^{\mathrm{QM}} - J_{\boldsymbol{q}}^{\mathrm{QM}}). \tag{2.100}$$

The critical temperature is obtained by the limit of vanishing magnetization, i.e. for $\langle S_z \rangle^{\mathrm{RPA}} \to 0$ in Eq. (2.98) resulting in [18]

$$k_B T_{\mathrm{C}}^{\mathrm{RPA}} \quad = \quad \frac{2}{3} S(S+1) \left(\sum_{\boldsymbol{q}} \frac{1}{J_{\boldsymbol{0}} - J_{\boldsymbol{q}}} \right)^{-1} = \frac{2}{3} \left(\sum_{\boldsymbol{q}} \frac{1}{\tilde{J}_0 - \tilde{J}_{\boldsymbol{q}}} \right)^{-1}. \tag{2.101}$$

Together with the MF result (3.2), the above expression for T_C is standardly used in combination with DFT derived input parameters [13–17, 58].

Numerical Approaches

In principle, there are different methodologies to solve the Heisenberg model exactly by using numerical approaches. Generally, the most straightforward way would be an exact diagonalization of the Hamiltonian (2.83) in its matrix representation. However, due to the fast increase of the Hilbert space, which scales as $\sim (2S+1)^N$ with the number of spins N, these methods are restricted to small systems ($N \sim 10-100$) and are usually applied to study small magnetic clusters [64]. The magnetic interaction in bulk systems such as in the 3d ferromagnets Fe, Co, or Ni are typically very long-ranged (usually not negligible below at least twenty neighboring shells) and show RKKY-type[20] oscillating (ferromagnetic/antiferromagnetic) interactions.

The Quantum Monte Carlo (QMC) technique allows one to study much larger system sizes ($N \sim 10^4$) [65]. For spin systems as the Heisenberg model,[21] the standard methods are employing so called loop algorithms (loop [67] or direct loop [68]) based on different representations of the partition function (e.g. stochastic series expansion (SSE) [69] or path integral representation).[22] A detailed discussion of these methods goes beyond the scope of this work. We briefly discuss the main idea behind the QMC method and the main inherent limitations and refer for a detailed overview to Ref. [67].

For calculating the phase space average of a quantity O in a classical Monte Carlo (cMC) simulation, the direct evaluation of the sum

$$\langle O \rangle = \frac{1}{Z} \sum_{c \in \Omega} O(c) p(c), \tag{2.102}$$

where $Z = \sum_{c \in \Omega} p(c)$ denotes the partition sum, over the high-dimensional phase space Ω is circumvented by choosing a subset of configurations $\{c_i\}$ from Ω according to the probability distribution $p(c_i)$. The average is afterwards approximated as the mean value

$$\langle O \rangle \approx \overline{O} = \frac{1}{N_{\text{steps}}} \sum_{i}^{N_{\text{steps}}} O(c_i). \tag{2.103}$$

Typically in statistical physics, $p(c) = e^{-\beta E(c)}$ is the Boltzmann weight and $E(c)$ is the energy of the configuration c.

[20] RKKY stands for Ruderman-Kittel-Kasuya-Yosida and was originally proposed to describe the indirect exchange coupling between nuclear spins via the conducting electrons. The ferromagnetic/antiferromagnetic oscillation of the exchange coupling depending on distance is one prediction of the RKKY theory.

[21] In presence of very strong magnetic fields, the so called Worm algorithm provides an alternative treatment [66].

[22] A very recent methodology is the so called Quantum Wang-Landau method (QWL) [70]. It is the analogon of the classical Wang-Landau technique [71] and was very recently implemented in the ALPS package [72] for the special case of a nearest-neighbor $S = 1/2$ model. Since our attention is to study also the spin-dependence $S \geq 1/2$ and the impact of long-range interactions we do not discuss the method in the present work.

For a quantum system described by a *quantum-mechanical* Hamiltonian $\mathcal{H}$, a thermal average requires the solution of an operator expression

$$\langle O \rangle = \frac{\mathrm{Tr}\left(Oe^{-\beta\mathcal{H}}\right)}{\mathrm{Tr}e^{-\beta\mathcal{H}}}. \tag{2.104}$$

The main problem for solving expressions as the one above is the exponential $e^{-\beta\mathcal{H}}$ in the trace. A direct calculation requires the complete diagonalization of $\mathcal{H}$. As pointed out above, this is computationally not feasible for larger systems due to the huge configuration space. Monte Carlo techniques can again be applied, but require the mapping of the quantum problem onto a classical one. A common approach is to rewrite the exponent in a Taylor expansion[23]

$$Z^{\mathrm{QM}} = \mathrm{Tr}e^{-\beta\mathcal{H}} = \sum_{n=0}^{\infty} \frac{(-\beta)^n}{n!} \mathrm{Tr}\mathcal{H}^n = \sum_{n=0}^{\infty} \sum_{\{\alpha\}} \frac{(-\beta)^n}{n!} \langle \alpha | \mathcal{H}^n | \alpha \rangle \tag{2.105}$$

in the basis $\{\alpha\} = \{|S_1^z, S_2^z, \ldots, S_N^z\rangle\}$.

This procedure is called stochastic series expansion (SSE) technique [69]. The *effective* weights $p(c)$ are defined by the product of matrix elements $\mathcal{H}^n$ and the factor $(-\beta)^n/(n!)$. The reformulation of Eq. (2.104) in terms of $p(c)$ allows one to employ (classical) Monte Carlo schemes. The main limitation is, however, that by construction the effective weights $p(c)$ for some configurations c can be in principle negative, i.e. $p(c) < 0$. This is the famous "*negative sign problem*" in QMC methods [73, 74]. These situations occur in the Heisenberg model when magnetic frustration is present (e.g. in the antiferromagnetic fcc lattice [75]). A prototype example to illustrate magnetic frustration is the antiferromagnetic triangular Ising model

$$\mathcal{H}^{\mathrm{Ising}}_{\mathrm{Triangular}} = J(\sigma_1\sigma_2 + \sigma_2\sigma_3 + \sigma_3\sigma_1) \tag{2.106}$$

with $\sigma = \uparrow, \downarrow$ as sketched in Fig. 2.6. Explicitly, negative weights arise due to matrix products such as

$$p(c) \sim (-1)^3 \langle \uparrow\downarrow\downarrow | \mathcal{H} | \downarrow\downarrow\uparrow \rangle \langle \downarrow\downarrow\uparrow | \mathcal{H} | \downarrow\uparrow\downarrow \rangle \langle \downarrow\uparrow\downarrow | \mathcal{H} | \uparrow\downarrow\downarrow \rangle < 0 \tag{2.107}$$

where three spin flips occur, yielding a factor $(-J)^3$.

There is up to now no general solution for the sign problem.[24] In principle, simulations can still be performed by taking the absolute value of $p(c)$

$$\langle O \rangle = \frac{\sum_c O(c)p(c)}{\sum_c p(c)} = \frac{\sum_c O(c)\mathrm{sgn}(p(c))|p(c)|/\sum_c |p(c)|}{\sum_c \mathrm{sgn}(p(c))|p(c)|/\sum_c |p(c)|} = \frac{\langle O\mathrm{sgn}\rangle_{|p|}}{\langle \mathrm{sgn}\rangle_{|p|}}. \tag{2.108}$$

Unfortunately, the statistical errors increase exponentially with increasing particle number N and inverse temperature β. To show this we consider the mean value of the sign $\langle \mathrm{sgn}\rangle_{|p|} = Z^{\mathrm{QM}}/Z^{\mathrm{QM}}_{|p|}$ in above equation being the ratio of the partition function $Z^{\mathrm{QM}} = \sum_c p(c)$ and the auxiliary function

[23] Alternatively the exponent can also be discretized in imaginary time τ (inverse temperature) $\beta = M\Delta\tau$ and $e^{-\beta\mathcal{H}} = (1 - \Delta\tau\mathcal{H})^M + \mathcal{O}(\Delta\tau)$. This representation is usually referred to as world line representation.

[24] In fact one can show that a generic solution of the sign problem would solve all problems in the complexity class NP (nondeterministic polynomial) in polynomial time [76].

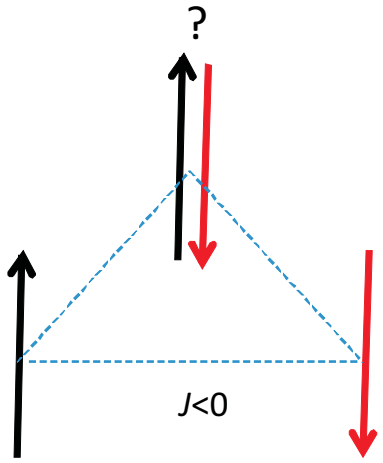

Figure 2.6: Sketch for the antiferromagnetic ($J < 0$) triangular. There is no configuration which minimizes the energy of all three bonds, causing magnetic frustration.

$Z^{\mathrm{QM}}_{|p|} = \sum_c |p(c)|$ used for the sampling. Since the partition functions are exponentials of the free energies, this ratio is exponential proportional to the free energy difference ΔF

$$\langle \mathrm{sgn} \rangle_{|p|} = Z^{\mathrm{QM}}/Z^{\mathrm{QM}}_{|p|} = \exp(-\beta N \Delta F). \tag{2.109}$$

Consequently, the relative error $\Delta\mathrm{sgn}/\langle \mathrm{sgn} \rangle$ increases exponentially with increasing particle number N and inverse temperature β:

$$\frac{\Delta \mathrm{sgn}}{\langle \mathrm{sgn} \rangle} = \frac{\sqrt{(\langle \mathrm{sgn}^2 \rangle - \langle \mathrm{sgn} \rangle^2)/N_{\mathrm{steps}}}}{\langle \mathrm{sgn} \rangle} = \frac{\sqrt{(1 - \langle \mathrm{sgn} \rangle^2)}}{\sqrt{N_{\mathrm{steps}}}\langle \mathrm{sgn} \rangle} \sim \frac{\exp(\beta N \Delta F)}{\sqrt{N_{\mathrm{steps}}}}. \tag{2.110}$$

Similar the error in the numerator in (2.108) increases exponentially [76] and hence the computational time needed to achieve a certain relative error scales exponentially with inverse temperature β and spins N.

As mentioned in the beginning of this section, in real materials such as Fe, Co or Ni, the interactions are typically long-ranged and show RKKY-type oscillating (ferromagnetic/antiferromagnetic) interactions. As we will show explicitly in Sec. 3.2.2, these type of interactions cause a negative sign problem and limit therewith the application of QMC to these materials. Considering the shortcomings of the quantum methods, it is not surprising that for properties of magnetic systems addressed in the present work (e.g. *ab initio* derived T_C), apart from the analytic methods [13–17], only *classical* cMC calculations are commonly employed [13, 43, 48, 54].

2.2.4 Vibronic and Electronic Free Energy

So far, the magnetic contribution to the free energy is considered. In order to accurately describe the transversal spin degree of freedom we recourse to the Heisenberg model, where the single-particle excitations (spin-flips) were neglected. Increasing the temperature does not only induce single-particle excitations between bands of *opposite* spins. It goes without saying that due to the Fermi distribution the electrons also occupy states above the Fermi energy ϵ_{F} in the same bands (without spin-flips). In the framework of finite temperature DFT this contribution is usually referred to as *electronic contribution*. The other main mechanism contribution to the free energy is driven by the motion of atoms, the so called *vibronic contributions*. In the following we briefly outline how both contributions can be effectively captured within the DFT framework.

Electronic Free Energy

For convenience we separate the electronic free energy F^{el} into the $T = 0$ K ground-state energy E^{tot} and the finite temperature entropy term S^{el},

$$F^{\mathrm{el}}(T, V) = E^{\mathrm{tot}}(T = 0\ \mathrm{K}, V) - TS^{\mathrm{el}}(T, V). \tag{2.111}$$

A very common and accurate parameterization of $E^{\mathrm{tot}}(T = 0\ \mathrm{K}, V)$ is given by the Murnaghan equation of state which will be used for the further evaluation [77].

To derive $S^{\mathrm{el}}(T, V)$ we employ the finite temperature formulation of DFT given by Mermin [78]. The key idea to simulate the electronic excitations is to combine the Fermi function[25] $f^{\mathrm{Fermi}}(\epsilon_i) = [1 + \exp(\beta\epsilon_i)]^{-1}$ with the single-particle electron energies ϵ_i [Eq. (2.25)]. The approach employs the analytically known (see e.g. [79]) expression for the electronic entropy of an ideal, non-interacting Fermion gas (e.g., the auxiliary Kohn-Sham particles)

$$\begin{aligned} S^{\mathrm{el}}(T, V) = -k_B \sum_i \{&[1 - f^{\mathrm{Fermi}}(T, \epsilon_i(V))] \ln[1 - f^{\mathrm{Fermi}}(T, \epsilon_i(V))] \\ &+ f^{\mathrm{Fermi}}(T, \epsilon_i(V)) \ln f^{\mathrm{Fermi}}(T, \epsilon_i(V))\}. \end{aligned} \tag{2.112}$$

Physically, the first expression on the right-hand side of above equation originates from the contribution of unoccupied states (holes) whereas the second term originates from the occupied states (particles). In practice, both contributions were computed on a finite mesh[26] of temperatures T and volumes V. Eq. (2.112) is widely used to compute DFT based electronic free energies and has been successfully applied to various materials (see e.g. [80, 81]).

Vibronic Free Energy

A major contribution to the free energy in solids is given by the thermally driven nuclei motion, the vibronic excitations. Thermal energy induces collective lattice vibrations which can be described by Bose quasiparticles, called phonons. It turns out that the so called *quasiharmonic approximation*

[25] For the ideal Fermi gas (of the electrons) at $T = 0$ K, the chemical potential μ is equal to the Fermi-energy E_F. For convenience the single-particle energies are shifted such that $\mu \equiv 0$.

[26] The explicit technical parameters ensuring a convergence of less than 1meV per atom is system dependent. The chosen parameters are therefore explicitly given in the text at the corresponding place.

(qh) is able to predict the vibronic contribution to a large extent whereas explicit[27] anharmonic contributions (which go beyond the qh) are in magnitude smaller [80, 81].

To derive the qh contribution to F^{vib} one can employ constrained DFT calculations for a fixed (given) set of nuclei positions $\{\mathbf{R}_I\}$. Within the adiabatic approximation the nuclei move in an effective potential given by the Born Oppenheimer surface E^{BOS}, Eq. (2.9). The harmonic approximation is derived by a Taylor expansion of E^{BOS}. Defining the ionic equilibrium positions $\{\mathbf{R}_I^0\}$ and ionic displacements $\{\mathbf{\Delta}_I\}$ we can expand $E^{\text{BOS}}(\{\mathbf{R}_I^0 + \mathbf{\Delta}_I\})$ for small $\{\mathbf{\Delta}_I\}$:

$$E^{\text{BOS}}(\{\mathbf{R}_I^0 + \mathbf{\Delta}_I\}) = E^{\text{BOS}}(\{\mathbf{R}_I^0\}) + \sum_{I\alpha} \Phi_{I\alpha}\mathbf{\Delta}_{I\alpha} + \frac{1}{2}\sum_{I\alpha,J\beta} \Phi_{I\alpha,J\beta}\mathbf{\Delta}_{I\alpha}\mathbf{\Delta}_{J\beta} + \mathcal{O}(\mathbf{\Delta}^3). \tag{2.113}$$

Here,

$$\Phi_{I\alpha} = \left.\frac{\partial E^{\text{BOS}}}{\partial \mathbf{R}_{I,\alpha}}\right|_{\mathbf{R}_I^0} \equiv 0, \tag{2.114}$$

denotes the derivative of E^{BOS} with respect to the displacement of nuclei $\boldsymbol{I}$ in direction α at $\mathbf{R}_I^0$, which vanishes by definition (equilibrium position). Analogously, one defines the so called force constant matrix as

$$\Phi_{I\alpha,J\beta} = \frac{\partial^2 E^{\text{BOS}}}{\partial \boldsymbol{R}_{I\alpha}\partial \boldsymbol{R}_{J\beta}} = -\frac{\partial F^{\text{HF}}_{I\alpha}}{\partial \boldsymbol{R}_{J\beta}}. \tag{2.115}$$

$F^{\text{HF}}_{I\alpha}$ represent the Hellmann-Feynman forces which can be very conveniently computed within a plane-wave approach using the Hellmann-Feynman theorem [82].

Neglecting the higher order terms $\mathcal{O}(\mathbf{\Delta}^3)$ in Eq. (2.113) is called *harmonic approximation*. Eq. (2.113) is therewith reduced to the problem of a harmonic oscillator with energies ω_i for which the known analytic expression for the free energy is given by

$$F^{\text{vib}}(T,V) = \frac{1}{N_n}\sum_i^{3N_n}\left(\frac{1}{2}\hbar\omega_i + k_B T \ln\left[1 - \exp\left(-\frac{\hbar\omega_i}{k_B T}\right)\right]\right), \tag{2.116}$$

where the sum runs over the $3N_n$ phonon states of the N_n atoms in the unit cell.[28] The first summand corresponds to the zero-point vibrations and the second represents the entropy of the ideal, non-interacting Bose-gas (here phonon gas) [79]. There are in principle two, nowadays standard approaches to obtain the phonon frequencies ω_i. Starting point is the construction of the dynamical matrix $D_{I\alpha,J\beta} = \frac{1}{M}\Phi_{I\alpha,J\beta}$ which can be done in real space (*direct-force* method) or in reciprocal space employing typically perturbation theory (*linear-response* methods).[29] For a detailed overview we refer to [83]. The eigenvalues of D provide eventually the squared frequencies ω_i^2. In practice, crystal symmetries are usually employed to reduce the number of required atom displacements $\{\mathbf{\Delta}_I\}$ to a minimum set.[30]

[27] Anharmonic contributions are (partially) *implicitly* included in the quasiharmonic approximation due to the volume dependence of the frequencies. The remaining part, which is not included in the qh approximation, is usually called *explicit* anharmonic contribution.

[28] For convenience we outline here the approach for one-species unit cell. The extension to multi-species systems is straightforward.

[29] Both are complementary and should yield in principle to the same results. We restrict ourselves in the present study, therefore, to the direct-force method.

[30] In the present work, the SxPhonons add-on of S/PHI/nX [84] has been employed to fully automatically determine

In principle the phonon frequencies can depend on temperature and volume respectively, i.e. $\omega_i = \omega_i(T, V)$. However, as it turned out, the explicit dependence on temperature is rather small [81] whereas the major contribution is included in the volume dependence. Therefore, one conventionally assumes $\omega_i \equiv \omega_i(V)$, which is known as the *quasiharmonic* (qh) approximation. The qh approximation has been proven to provide reliable results for a large range of metals [80] and will be also used in this work whenever the vibronic contribution is computed.

Summary

In this section it was shown, how finite temperature properties can be obtained by first principles by combining statistical concepts with DFT input data. It was discussed how electronic and vibronic contributions to the Helmholtz free energy are commonly calculated based on first-principles methods. To account for magnetic excitations, the concept of adiabatic spin dynamics and the Heisenberg model were introduced. Theoretical concepts to derive the input data from first principles and different ways to solve the magnetic model were presented.

the set of minimum displacements and to compute the frequencies based on the *ab initio* calculated Hellmann-Feynman forces.

Chapter 3

Results

In the previous chapter the magnetic Heisenberg model was derived based on the adiabatic spin dynamics. We remind that strictly speaking this magnetic model is only well defined for a localized spin system while single spin-flip transitions are neglected. Despite many successful applications (see e.g. [15, 16, 48]), employing the Heisenberg model for itinerant magnetic systems is, therefore, in particular for iron, still critically discussed in literature [48, 85].

In addition, as already indicated in the previous section, there is no numerically exact solution to the quantum Heisenberg Hamiltonian, Eq. (2.70), with realistic exchange parameters available. A more detailed discussion in Sec. 3.2.2 shows that the most promising approach for an exact solution, the QMC, suffers from the negative sign problem caused by the long-ranged magnetic interactions. Therefore, one has to choose between

(a) an approximate solution to the *full* Hamiltonian, or

(b) an exact solution to a *simplified* Hamiltonian.

Based on the general concepts explained in the previous chapter, we have developed for both choices promising and reliable methods. The ultimate aim of these efforts is to describe and predict thermodynamic properties such as, e.g., the specific heat capacity or the free energy for magnetic materials. In order to achieve a full description, the magnetic contribution will be combined with other excitation processes such as vibronic contributions. To large extend the magnetic free energy of a metal depends on its magnetic state. Therefore, we first focus on the determination of T_C. This also gives us the chance to prove the applicability of our chosen magnetic model Hamiltonian.

3.1 Determination of $T_C(p)$ for Bcc Iron: Performance and Robustness of Different Approaches

We introduce the approximate solution (a) on a question of high relevance for applications: The pressure dependence of the Curie temperature T_C of iron. Apart from the impact for technological applications, we will later identify T_C as the crucial quantity for building up a simplified model Hamiltonian ((b) above). This will be discussed in more detail in Sec. 3.4.

In Chapter 1 we pointed out the need of parameter free approaches in particular for supplementing/complementary data within the well known and heavily used CALPHAD (calculation of phase

diagram) approach. We remind that the CALPHAD methodology allows to compute phase diagrams of multi-component alloys on the basis of fitting thermodynamic data. Indeed, T_C is a crucial quantity within the CALPHAD ansatz since it is one of the few fitting parameters entering the empirical free energy expression [86, 87]. Since in particular the description of pressure dependent quantities is still limited in CALPHAD (most of experimental input is given for ambient pressure), predicting pressure dependent $T_C(p)$ is a very important task for the proposed *ab initio* ansatz.

For one of the key materials in the present study, bcc iron, the experimentally known weak dependence of $T_C(p)$ has by now not been understood from first principles and a key question remains still unanswered: What is the physical origin of the experimentally observed negligible change of T_C with applied pressure ($\Delta T_C(p) \approx \pm 2K$ for p up to 20 kbar [88])?

In a recent work [89] it is claimed that the Heisenberg model itself (which we have chosen for our analysis) is inapplicable for a meaningful description of $T_C(p)$ in iron. This is despite the fact that the model performs well even for more complex magnetic systems such as, e.g., Fe-Co-alloys [54], Heusler alloys [90], or diluted magnetic semiconductors [91]. This raises the question: what is the reason behind this selective failure?

The following section is devoted to these questions. At the same time the analysis offers an ideal opportunity to test the introduced methods. We would like to address explicitly the following points:

(1) How accurate is the DFT method including the necessary approximations such as for the xc-functional (LDA/GGA) to describe the spin-wave spectra (and hence the exchange coefficients) of magnetic systems?

(2) Is the combined method (DFT based Heisenberg model+analytic approximation) able to reproduce the experimental findings for bcc iron, in particular the pressure independence of the Curie temperature $T_C(p) \approx 0$?

(3) What is the physical mechanism behind this pressure independence?

In order to make sure that the performance of our *ab initio* approach is not limited by the numerical convergence, the total energy differences are converged within less than 1 meV per atom which corresponds to uncertainties for the calculated T_C of less than 10 K. This accuracy limit has been achieved by using the following parameters: a density of the $\boldsymbol{k}$-points generated with the Monkhorst-Pack scheme of $\approx$ 5000 per atom, a plane-wave energy cutoff of $E_{cut} = 450$ eV, and ≈ 3000 $\boldsymbol{q}$-points for the magnetic integration in Eqs. (3.2) and (3.3). All calculations are performed employing the VASP [92, 93] package and using the projector augmented wave method (PAW) [94] within LDA and GGA (Perdew-Burke-Ernzerhof parameterization [95]).

We start the analysis with total energy calculations of spin spirals (2.57) for different volumes V, where the energy difference between the unperturbed (collinear) ground state ($\boldsymbol{q} \equiv 0$) and the spin spiral with wave vector $\boldsymbol{q}$ is denoted as $\Delta E_V(\boldsymbol{q}, \theta)$, according to Eq. (2.64). We remind that the $\Delta E_V(\boldsymbol{q}, \theta)$ are directly connected to the spin-wave energy $\omega_V(\boldsymbol{q})$ via Eq. 2.65:

$$\omega_{\boldsymbol{q}}(V) = \frac{4}{M} \lim_{\theta \to 0} \frac{\Delta E(\boldsymbol{q}, \theta)}{\sin^2 \theta}. \tag{3.1}$$

Since all calculations were performed using fully relaxed non-collinear calculations[1], the choice of the θ angle is restricted to the two local minima at $\theta = \pi/2$ and $\theta = 0$. We, therefore, determine the magnon energies at $\theta = \pi/2$ but we will discuss the impact of the cone angle by comparing the magnon spectra with previous calculations which employ a perturbation theoretical ansatz for $\theta \to 0$ as well as by employing a "cutoff-analysis" for $\omega_{\boldsymbol{q}}$.

In order to check the stability of our approach with respect to the inherent approximation of the DFT formalism (i.e. the treatment of the xc-functional), the magnon spectrum $\omega_{\boldsymbol{q}}^{\mathrm{DFT}}(V)$ of bcc iron is computed for both, the LDA and the GGA-PBE functional. All calculations are carried out for different volumes $V \in (11.39\text{Å}^3, 12.45\text{Å}^3)$ to obtain eventually the volume dependence $T_C(V)$. The experimental volume at the Curie temperature under ambient pressure is $V^{\mathrm{exp}}(T_C) \approx 12.1$ Å^3. The results for $\omega_{\boldsymbol{q}}^{\mathrm{DFT}}(V)$ at two different volumes, $V = 11.21$ Å^3 and $V = 12.45$ Å^3, are shown in Fig. 3.1 in comparison to experimental and previously published theoretical data from Refs. [15] and [89]. The equilibrium lattice constants at $T = 0$ K are given by $V_0^{\mathrm{GGA}} = 11.39$ Å^3 , $V_0^{\mathrm{LDA}} = 10.31$ Å^3, and is extrapolated to $V_0^{exp} = 11.69$ Å^3 from experiment, respectively.

The agreement between the experiment and the calculated frequencies is remarkable for both LDA and GGA functionals, indicating that the choice of the xc-functional is probably not the limiting factor. In fact both functionals provide a similar accurate description of the magnetic excitations in the system. The agreement between the previously and presently calculated magnon spectra for experimentally accessible magnon energies is also good. For magnon energies higher than ≈ 0.25 eV there exist qualitative differences between these results, particular around the H-point. As was shown by Shallcross *et al.* in Ref. [46], these differences can be traced back to different spin-wave cone angles θ (see Eqs. (2.64) and (2.65)) used for the calculation of the magnon spectrum. Since the differences for bcc iron are only at relative high magnon energies (0.25 eV corresponds to ≈ 3000 K) they can be safely neglected. We will show this explicitly by introducing a cutoff-analysis for the magnon energy.

It should be mentioned that, as discussed in Sec. 2.2.2, spin-waves are only small perturbations from the ground state. From a principle point of view, a cone angle $\theta \to 0$ seems to provide the most reasonable description [12]. For the extracted exchange coefficients (which are directly connected to $\omega(\boldsymbol{q})$ via Eq. (2.64)), such a principle physical argument does not hold and the appropriate choice of θ for other systems (such as Nickel) at high temperatures is still debated in literature [46, 47]. In Ref. [47] it is argued that a larger cone angle may better mimic the situation at high temperatures (paramagnetic regime). In particular in case of bcc iron the choice of θ is, however, not crucial. This is consistent with previous calculations of planar spirals $\theta = \pi/2$ (as used in this work) which yield satisfactory results for the magnon spectra and the critical temperature [43, 44] of bcc Fe.

Considering the first point (1) we raised in the beginning, we can conclude that the DFT formalism in combination with the adiabatic spin dynamics, the so called frozen magnon approach, indeed allows a reliable and accurate description of the collective magnetic excitations (spin-waves).

[1] In principle VASP offers the possibility to add a penalty contribution to the total energy expression in order to force the direction of the local magnetic moments into a given direction via the flag I_CONSTRAINED_M. This contribution is controlled via a parameter LAMBDA.

We now closer investigate the critical temperature. Combining Eqs. (2.63)-(2.65) with Eqs. (2.90) and (2.101), the analytic solutions for mean field are given as

$$k_B T_{\mathrm{C}}^{\mathrm{MF}}(V) = \frac{M(V)}{6} \sum_{\boldsymbol{q}} \omega_{\boldsymbol{q}}(V), \tag{3.2}$$

and for RPA as

$$k_B T_{\mathrm{C}}^{\mathrm{RPA}}(V) = \frac{M(V)}{6} \left(\sum_{\boldsymbol{q}} \frac{1}{\omega_{\boldsymbol{q}}(V)} \right)^{-1}. \tag{3.3}$$

To compare the theoretical values for $T_C(V)$ with the experimental $T_C^{\mathrm{exp}}(p)$ we transformed the experimentally measured $T_C^{\mathrm{exp}}(p)$ to $T_C^{\mathrm{exp}}(V)$ employing experimental data for $V^{\mathrm{exp}}(p, T = T_C)$.[2] In order to elucidate the sensitivity of the Heisenberg model with respect to the quality of the model input data, we investigate the volume dependence of the Curie temperature employing three different DFT data sets. Specifically, we compare the qualitative behavior of $T_C(V)$ obtained on the basis of the DFT calculations (i) with the PAW basis set and LDA functional, (ii) with the PAW basis and the GGA-PBE xc-functional, and (iii) with the tight-binding linear-muffin-tin-orbital (TB-LMTO) basis set within the atomic sphere approximation (ASA) and LDA xc-functional with the experimental results (see Fig. 3.2). Comparison of the solutions (i) and (ii) allows to figure out the effect of the xc-functional, while comparison of solutions (i) and (iii) allows us to identify possible uncertainties related to the use of different DFT basis sets and methodologies for extracting the magnetic exchange constants (frozen-magnon vs frozen-magnon-torque method [97]).

Figure 3.2 highlights that $T_{\mathrm{C}}(V)$ of the Heisenberg model is, apart from a constant shift, very insensitive with respect to the choice of the xc-functionals for both, the RPA and the MF solution, when the same basis set is used. Even more noticeable, the use of the same exchange-correlation functional but different basis sets in the DFT calculations might lead to dramatic changes in the theoretical predictions for $T_C(V)$, as can be seen, e.g., on Fig. 3.2(b). The comparison with experiment reveals that all theoretical approaches evaluated in this work, i.e., GGA-PBE/LDA input with RPA/MF, are in good qualitative agreement with experiment showing a very weak dependence of the Curie temperature on the volume.

In order to figure out whether the use of different spin-wave cone angles θ (discussed above) might be responsible for the observed changes in the calculated volume-dependent Curie temperature, we have calculated T_C according to Eqs. (3.2)-(3.3) by introducing a cutoff magnon energy $\omega_{\mathrm{cut}} = 0.25$ eV [3] for the magnon frequencies, i.e. we set $\omega_{\boldsymbol{q}} \equiv \omega_{\mathrm{cut}}$ for $\omega_{\boldsymbol{q}} > \omega_{\mathrm{cut}}$. This treatment is motivated by the pronounced changes of the magnon spectrum at high energies (not accessible by

[2] In order to derive $V^{\mathrm{exp}}(p, T = T_C)$ we have parameterized the experimental dependence of the total energy $E(V, T = T_C)$ on the crystal volume V employing the Murnaghan equation of state. [77] The parameters of the Murnaghan equation at T_C (the bulk modulus $B_0^{\mathrm{exp}} = 119$ GPa, its derivative $B_0'^{\mathrm{exp}} = 5.3$, and the equilibrium lattice constant $V_0^{\mathrm{exp}} = 12.1$ Å^3) are taken from experiment performed by Zhang and Guyot. [96] The minimum of the enthalpy $H(p, V) = E(V) + pV$ at the Curie temperature and a given pressure p determines the equilibrium volume $V^{\mathrm{exp}}(p, T = T_C)$ and the corresponding lattice constant $V^{\mathrm{exp}}(p, T = T_C)$.

[3] The threshold value ω_{cut} is an energy above which the magnon spectra calculated employing $\theta = \pi/2$ and $\theta \to 0$ start to significantly (by more than 45 meV) deviate. The value $\omega_{\mathrm{cut}} = 0.25$ eV is deduced from the comparison of our results with the corresponding data of Ref. [15] (see Fig. 3.1). A similar threshold value applies for the different spin spirals calculated in Ref. [47].

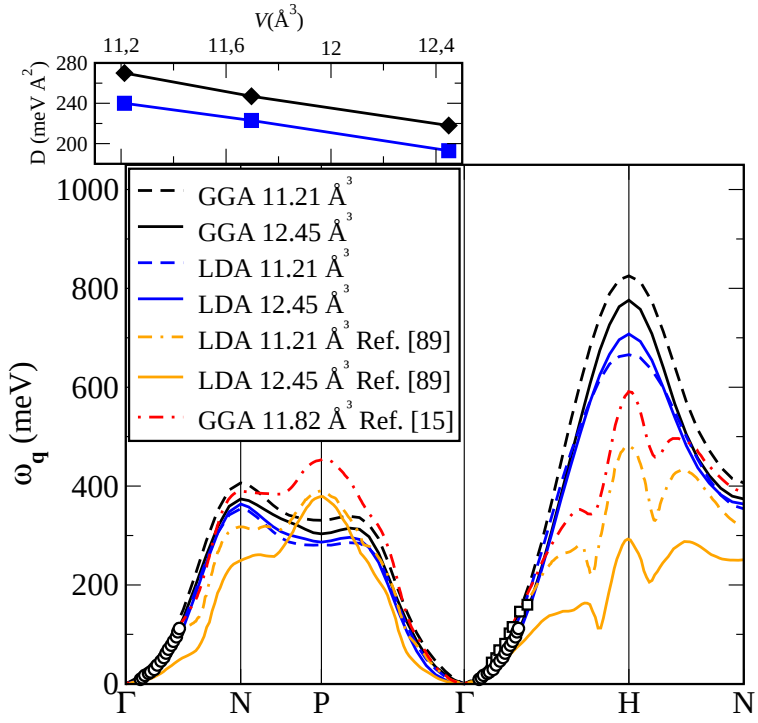

Figure 3.1: Calculated magnon spectra using planar spin spirals for two lattice constants, $a = 2.82$ Å (dashed lines) and $a = 2.92$ Å (solid lines), within GGA-PBE (black lines) and LDA (blue lines). For comparison the spectra obtained using a small cone angle taken from Ref. [89] (orange lines) and Ref. [15] (red line) are shown. The spectra taken from Refs. [15] and [89] were calculated using TB-LMTO employing GGA-PBE and TB-LMTO+ASA within LDA respectively. Experiments: Ref. [98], measured at 10 K (open squares), and Ref. [99], Fe(12-at.% Si), measured at 300 K (open circles).
Inset: spin-wave stiffness D obtained by using a least square fit of the low energy branch up to $|\boldsymbol{q}| = 0.4\ (2\pi/a_0)$.

experiment) due to the different cone angles and allows to estimate the resulting uncertainty of the calculated Curie temperatures.

The comparison of the Curie temperatures evaluated from the magnon spectrum with and without the cutoff energy are shown in Fig. 3.2. The introduction of the cutoff ω_{cut} results in an essentially volume-independent shift of the Curie temperature to smaller values over the complete range of the studied volumes. This already justifies that the choice of the spin-wave cone angle θ is not essential for a qualitative analysis of the volume dependence of the Curie temperature in bcc Fe. We notice, however, that quantitatively such shifts differ for the MF and RPA solutions of the Heisenberg Hamiltonian. The most pronounced change of the calculated Curie temperatures occurs for the MF solution (Eq. (3.2)), independent on whether LDA or GGA exchange-correlation functionals are used. Within the RPA theory, however, an accurate description of the high-temperature magnons is not decisive for the evaluation of the Curie temperature since those energies entering the approximation for the Curie temperature have a lower weight [Eq. (3.3)]. Indeed, the maximum error introduced by the approximative treatment of the spin spirals for the RPA solution in this work

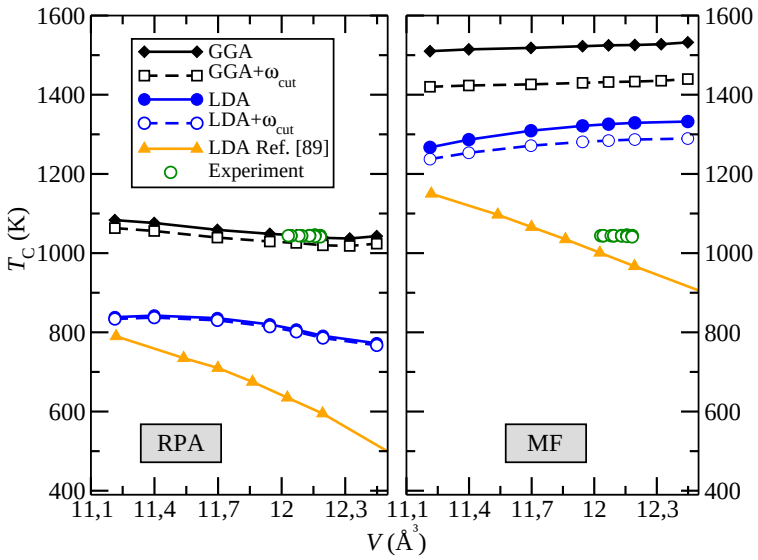

Figure 3.2: The Curie temperatures within the RPA (left panel) and the MF (right panel) approximation, for both LDA (blue lines) and GGA (black lines) exchange-correlation functionals. For comparison the results of Ref. [89] (LDA, orange curves), and the experimental Curie temperatures $T_C^{\mathrm{exp}}(a)$ for different lattice constants a (open green circles) are shown. The transformation of $T_C^{\mathrm{exp}}(p)$ [88] to $T_C^{\mathrm{exp}}(a)$ is described in the text.

is less than 10 K for LDA, and 20 K for GGA. The assumption of the planar spin spirals within RPA only marginally affects the overall accuracy of our calculations. Since the frozen-magnon-torque method [97] should be comparable with the frozen-magnon-approach used in this work, the remaining differences between our results and Ref. [89] are likely related to the different basis sets (plane-wave vs. LMTO basis) used within the DFT calculations.

Since the PAW basis set used in this work allows for consistent convergence with respect to the quality of the basis set, in contrast to the LMTO basis employed in Ref. [89], we focus on the DFT calculations obtained with the PAW basis set in the following. As the scatter of the theoretical predictions for $T_C(V)$ is still significant, we identify the best theoretical model for the prediction of the Curie temperature in bcc iron by comparing the theoretical data with the experiment. Regarding the qualitative behavior we find that all combinations (GGA-PBE/LDA input with RPA/MF) provide a reasonable agreement with experiment by showing a very weak dependence of the Curie temperature on the volume. The combination GGA-PBE and RPA provides moreover a quantitative agreement with experiment. The open debate in Ref. [89] if the model is applicable for bcc Fe is therewith resolved. The different results obtained in [89] can be traced back either to the employed basis set (tight-binding LMTO within ASA) or the frozen-magnon-torque method [97].[4]

Our analytic solutions Eqs. (3.2) and (3.3) allow us to obtain a deeper physical insight into the dependence of the critical temperature on pressure. The two physical quantities determining

[4]In fact, in the description of the method [97] the authors clearly state that their approximation is "reasonable fast and semiquantitative" and "certainly superior to model descriptions like the Debye model". Our PAW approach together with a full self-consistent treatment of the spin-waves goes one step further and allows to systematically overcome some of the approximations necessary in Ref. [89].

Table 3.1: Derivatives of the Curie temperature T_C with respect to lattice constant a and pressure p. $\partial T_C/\partial a$ is obtained by using a linear fit over the entire volume range from $a = 2.82$ Å up to $a = 2.92$ Å. The values in brackets are obtained by the linear fit in a volume range from $a = 2.88$ Å to $a = 2.9$ Å, which corresponds to the pressure range applied in experiment (≈ 20 kbar). The procedure of transforming $T_C(V)$ to $T_C(p)$ is described in the text.

	GGA		LDA		
	$\partial T_C/\partial V$ $\left(\mathrm{K}/10^{-2}\mathrm{Å}^3\right)$	$\partial T_C/\partial p$ (K/kbar)	$\partial T_C/\partial V$ $\left(\mathrm{K}/10^{-2}\mathrm{Å}^3\right)$	$\partial T_C/\partial p$ (K/kbar)	Ref.
MF	1.63(1.25)	-0.14(-0.11)	5.35(3.04)	-0.60(-0.34)	this work
MF+ω_{cut}	1.79(1.58)	-0.13(-0.11)	5.26(2.93)	-0.48(-0.27)	this work
MF+LMTO	-	-	-24.1	1.6	Ref. [89]
RPA	-3.81(-3.30)	0.32(0.28)	-5.60(-11.51)	0.61(1.26)	this work
RPA+ω_{cut}	-4.57(-4.79)	0.31(0.33)	-6.96(-14.31)	0.62(1.27)	this work
RPA+LMTO	-	-	-27.4	1.8	Ref. [89]
Experiment	0.0 ± 0.04	0.0 ± 0.03	0.0 ± 0.04	0.0 ± 0.03	Refs. [88], [96]

its behavior are the spin-wave energies $\omega_{\boldsymbol{q}}$ as well as the local magnetic moments M. To analyze in the following the reason for the weak volume (pressure) dependence of the calculated Curie temperature we consider first the corresponding changes of the magnon spectra. The results are shown in Fig. 3.1 and we observe that the magnon branches become softer with increasing volume of the atomic cell, i.e., the energies of the corresponding magnons become smaller. This can be interpreted as a decrease of the magnetic coupling between the localized magnetic moments. To quantify this effect we show in the inset of Fig. 3.1 (upper panel) the volume-dependent spin-wave stiffness D, derived in the low wavelength limit $\omega^{\mathrm{DFT}}_{\boldsymbol{q}\to 0} \approx D\boldsymbol{q}^2$. According to Eqs. (3.2) and (3.3) the decrease of the magnon energies leads to a decrease of the Curie temperature. For both functionals GGA as well as for LDA the decrease is apparently compensated by another mechanism, since the Curie temperature remains essentially constant with pressure (see Tab. 3.1).

The reason for the stability of T_C versus the applied pressure can be understood recalling that the increase of the atomic volume does not only weaken the magnon excitation energies, but also changes the magnitude of the local moments. We show the local magnetic spin moment $M(V)$ at different atomic volumes in Fig. 3.3 for both DFT functionals. At the theoretical ground-state volumes, i.e. V_0^{LDA} and V_0^{GGA}, LDA underestimates the local spin moment while GGA slightly overestimates the experimental findings $M^{\mathrm{exp}}(T = 0\ \mathrm{K}) = 2.14\mu_B$ [100].[5] (The small contribution to the local magnetic moment due to spin orbit coupling ($< 0.1\mu_B$) is neglected.) Both functionals show a smoothly increasing local magnetic spin moment with increase of the atomic volume, which is due to the increasing distance between the atoms and a consequent enhancement of the localization of the 3*d*-electrons that form the local magnetic moments. According to Eqs. (3.2) and (3.3) the Curie temperature is directly proportional to the magnitude of the local magnetic moment $M(V)$, i.e., the increase of the local moments with increase of the volume should lead to a corre-

[5] At the experimental volume the situation is reversed and $M^{\mathrm{LDA}}(V^{\mathrm{exp}})$ comes closer to the corresponding experimental value.

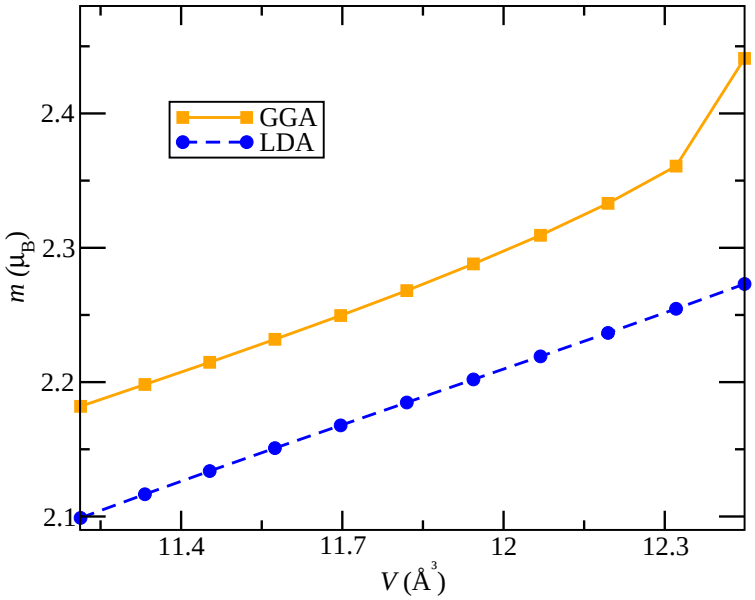

Figure 3.3: The local magnetic spin moment of ferromagnetic bcc iron as function of the volume calculated within GGA (solid orange line) and LDA (dashed blue line) xc-functionals.

sponding increase of the Curie temperature. Therefore, two coupled volume-dependent magnetic effects determine the behavior of the Curie temperature: The increase of the volume (decrease of the pressure) leads to a weakening of the spin-wave energy (reflecting the strength of the magnetic coupling) and simultaneously leads to an increase of the local magnetic moments. The sensitive interplay between these two effects determines the actual dependence of the Curie temperature on the volume (pressure) for a particular material. All calculated volume and pressure dependencies[6] are summarized in Tab. 3.1. The volume dependence is obtained by using a linear fit over the entire atomic volume range from $V = 11.21$ Å^3 up to $V = 12.45$ Å^3. Since the pressure applied in experiment ($\approx$ 20 kbar) corresponds to a change of the volume of only ≈ 0.25 Å^3 (see Refs. [96] and [101]), we also fit the volume dependence of T_C in a volume range starting from $V = 11.94$ Å^3 to $V = 12.19$ Å^3. The corresponding results are also shown in Tab. 3.1 (shown in brackets). Using the smaller fit-range the volume and pressure dependencies are only slightly changed, except for the combination of LDA-RPA where the volume dependence is more pronounced. Regarding the quantitative agreement between theory and experiment, GGA appears to be closer to experiment with respect to the Curie temperature. The constant shift between LDA and GGA is a direct consequence of the higher calculated magnetic moment since the calculated magnon spectra within both GGA and LDA are almost similar. In overall the Curie temperatures calculated with both functionals do not significantly depend on the volume (see Tab. 3.1), and we get within GGA $(\partial T_C^{\mathrm{RPA}}/\partial V) \approx 4.7$ K/10^{-2} Å^3. This corresponds to a change of the Curie temperature of $\Delta T_C \approx 5$ K for the pressure range investigated in the experiment [88] (up to 17.5 kbar).

[6]The pressure dependence of the Curie temperature $T_C(p)$ can be obtained from the corresponding volume dependence $T_C(V)$ via $\partial T_C/\partial p = (\partial T_C/\partial V)(\partial V/\partial p)|_{V=V(T_C)}$, where $(\partial V/\partial p)|_{V=V(T_C)} = -[V/B_0(T_C)]$ is obtained by calculating[7] the temperature dependent bulk modulus B_0, as described in Refs. [16, 80] in detail.

Conclusion

Based on DFT input, the critical temperature can be accurately determined by approximative solutions of the Heisenberg model. This has important consequences: As will be discussed in more detail in Sec. 3.4, T_C can be identified as a key quantity for constructing an alternative, simplified model. A main advantage of the employed analytic access is that the different physical mechanisms which determine T_C can be discriminated. Both analytic approaches provide a promising way for the next step which is consequently the extension of the approach for thermodynamic quantities such as the free energy or the specific heat capacity.

3.2 Thermodynamics of Magnetic Metals: Free Energy and Specific Heat Capacity

A central concern of this work is the study of temperature dependent quantities such as the free energy or the specific heat capacity. These quantities are not only determined by magnetic contributions but require also the incorporation of other excitation mechanisms such as vibronic and electronic excitations.

For this purpose, the Helmholtz free energy surface $F(T, V)$ as a function of the temperature T and the crystal volume V is considered in the adiabatic approximation, see Eq. (2.3):

$$F(T, V) = F^{\mathrm{vib}}(T, V) + F^{\mathrm{el}}(T, V) + F^{\mathrm{mag}}(T, V), \tag{3.4}$$

that treats the vibrational F^{vib}, the electronic F^{el} (including the energy of the static lattice) and the magnetic F^{mag} contribution separately (see also Fig. 2.1). For bcc iron, the adiabatic approximation is well justified since the underlying excitation mechanisms, i.e. phonon, electron and magnon excitations, reside on different time scales [102]. The validity of the adiabatic approximation is further supported by recent explicit *ab initio* calculations of the magnon-phonon coupling in iron [103].

The contributions F^{vib} and F^{el} are calculated within the quasiharmonic approximation and finite temperature DFT [78], respectively, as discussed in Sec. 2.2.4. As the first step, we have therefore calculated the phonon dispersion of ferromagnetic bcc iron which serves as an input to the partition function needed for computing F^{vib}, see Eq. (2.116). The comparison with the experimental phonon spectrum shows a good agreement (Fig. 3.4). The small difference between experimental and our theoretical phonon energies of 5 meV is due to the xc-functional. Using a Born-von Kármán fit to the experimental as well as to the theoretical phonon dispersions we estimate the difference in the free energy to be around 5 meV/atom at 1300 K. Such differences are consistent with the findings in [80] where the uncertainty due to the treatment of the xc-functional on the vibronic free energy was empirically found for a large range of materials to be in the order of 10 meV up to 1000 K.

The electronic contribution F^{el}, Eq. (2.111), is obtained by computing the total energies E^{tot} and the band occupations determined by the Fermi distribution function at a given temperature T, see Eq. (2.112). The resulting combined vibronic and electronic free energy ($F^{\mathrm{vib}} + F^{\mathrm{el}}$) is shown in Fig. 3.5 (orange line) and compared to CALPHAD data. Clearly, the deviation between *ab initio* ($F^{\mathrm{vib}} + F^{\mathrm{el}}$) and CALPHAD data increases rapidly with temperature. For instance, at 1200 K, which corresponds to the experimental bcc to fcc transition temperature, the difference is $\approx$ 45 meV. An even more sensitive physical quantity that allows to check the predictive accuracy of the T dependent *ab initio* calculations is the heat capacity, C_P, which is the second derivative of the free energy surface with respect to temperature. Figure 3.6 shows that the combined vibronic and electronic heat capacity agrees well with experimental data only up to $\approx$ 300 K, in agreement with previous results [6]. At higher temperatures, however, Fig. 3.6 clearly reveals that it cannot account for the rapid increase of the experimental heat capacity. It is therefore obvious that an accurate determination of the free energy contribution from magnetic excitations is crucial.

For this purpose we first employ the analytic approximations, which already showed accurate results for the critical temperature in the previous section. We discuss the known MF solution for the magnetic free energy F^{mag} which we employ in an integrated approach (including F^{vib} and F^{el}).

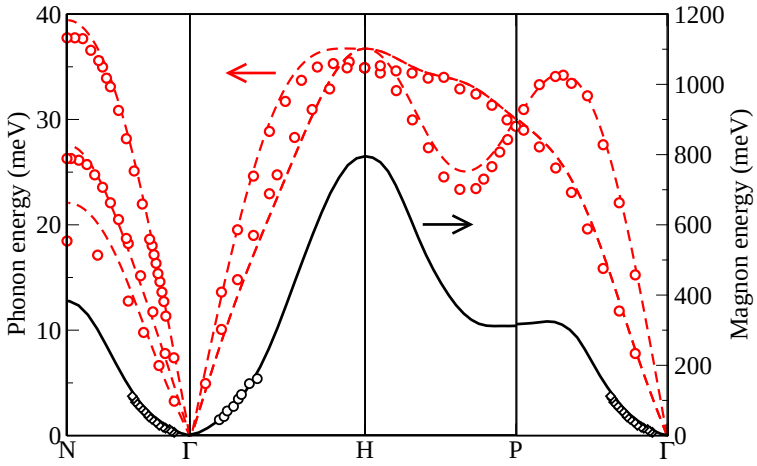

Figure 3.4: *Ab initio* phonon (red dashed line, left axis) and magnon (black line, right axis) spectrum of ferromagnetic bcc iron. The results are respectively compared with available neutron scattering data [98, 99, 104].

In contrast to MF, no consistent RPA solution for F^{mag} existed previous to our work for the case of a general spin system. Consequently, apart from T_C predictions, the RPA has not been applied up to now for F^{mag} predictions of realistic materials systems. The extension and application of the RPA theory is therefore a major subject of the next section.

3.2.1 Analytic Approaches

The key quantity for deriving the magnetic free energy

$$F^{\mathrm{mag}}(T) = U(0) - T\int_0^{T'} dT' \frac{U(T') - U(0)}{T'^2} \tag{3.5}$$

is the internal energy U of the system. Therefore, the expectation value of the magnetic Hamiltonian Eq. (2.83), i.e. $\langle \mathcal{H} \rangle \equiv U$, has to be calculated.

We start with the MF ansatz: $\mathcal{H}^{\mathrm{MF}}$ is given by Eq. (2.85) from which we can directly derive the internal energy $U^{\mathrm{MF}}(T)$. It is proportional to the square of the magnetization,

$$U^{\mathrm{MF}}(T) = J_0^{\mathrm{QM}} \langle S_z \rangle_{\mathrm{MF}}^2 = \frac{S}{S+1} \tilde{J}_0 m_{\mathrm{MF}}^2(S,T), \tag{3.6}$$

where the reduced MF magnetization m_{MF} is given by Eq. (2.87). Inserting Eq. (3.6) into (2.82) yields straightforwardly the MF magnetic free energy $F_{\mathrm{MF}}^{\mathrm{mag}}$.

The exchange coefficients (discussed in the previous section) and the spin quantum number S which enter (3.6) can be derived employing SDFT. The spin number S is connected to the local magnetic moment M by (2.59). For iron, M is almost entirely determined by the strongly localized

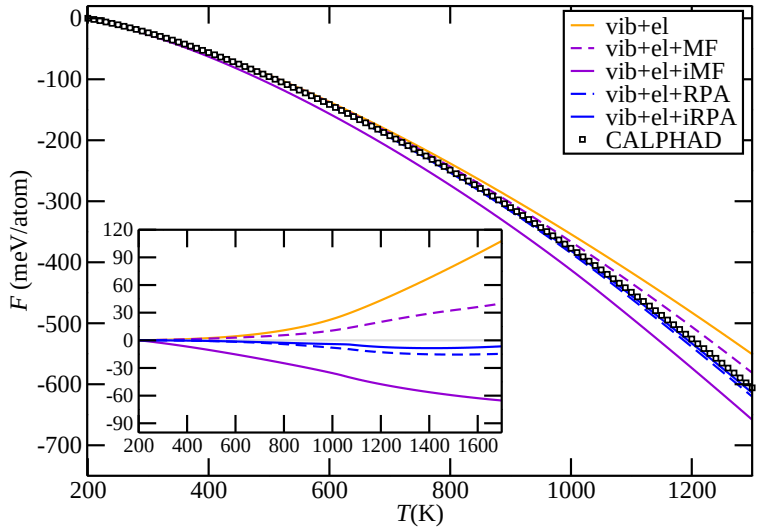

Figure 3.5: *Ab initio* free energy F at zero pressure as a function of temperature T including various combinations of the vibrational (vib), electronic (el), and magnetic contribution. The latter has been calculated within the mean field (MF), improved mean field (iMF), random phase approximation (RPA), and improved RPA (iRPA). The CALPHAD data has been obtained with the THERMOCALC program and the SGTE unary database [105]. Inset: The CALPHAD data is taken as the reference at each temperature.

3d-electrons and is therefore given by the total magnetization scaled by the number of atoms and a Landé factor of $g \approx 2$. Our $T = 0$ K PBE result of the total magnetic moment gives[8]

$$M \approx 2.2\ \mu_\mathrm{B}\ \rightarrow\ S \approx 1.1\ . \tag{3.7}$$

Using the computed spin quantum number and the corresponding exchange coefficients, we calculate the internal energy $U^\mathrm{MF}(T)$ and obtain F^mag by integration, Eq. (2.82). The MF free energy and specific heat capacity are shown in Figs. 3.5 and 3.6 (violett dashed lines), respectively. Up to ≈ 700 K both quantities are reasonably improved with respect to the pure vibrational and electronic contributions, but MF fails to reproduce the qualitative behavior of the heat capacity at the Curie temperature. In addition, as also shown in Fig. 3.2, the calculated T_C^MF is ~ 1.5 times higher than the experimental $T_\mathrm{C}^\mathrm{exp} = 1044$ K.

As discussed in Sec. 3.1, the RPA is known to give more accurate Curie temperatures than MF. We remind that within RPA we obtained a value much closer to experiment: $T_\mathrm{C}^\mathrm{RPA} = 2\left[\sum_{\boldsymbol{q}} 1/(\tilde{J}_0 - \tilde{J}_{\boldsymbol{q}})\right]^{-1}/(3k_\mathrm{B}) = 1082$ K (see also Fig. 3.2). However, in contrast to MF there is no RPA Hamiltonian which can directly be used. Instead the expectation value of the full Heisenberg model Eq. (2.83) needs to be calculated in order to derive the expression for the internal energy $U^\mathrm{RPA} = \langle\mathcal{H}\rangle$. We need two correlation functions, namely the transversal $\langle S_{i+}S_{j-}\rangle$ and the longitudinal $\langle S_{iz}S_{jz}\rangle$ one. Via the corresponding Green's function G_{ij}, an expression for the

[8] We remind that at the theoretical ground-state volumes LDA underestimates the local spin moment while GGA slightly overestimates the experimental findings $M^\mathrm{exp}(T = 0\ \mathrm{K}) = 2.14\mu_B$

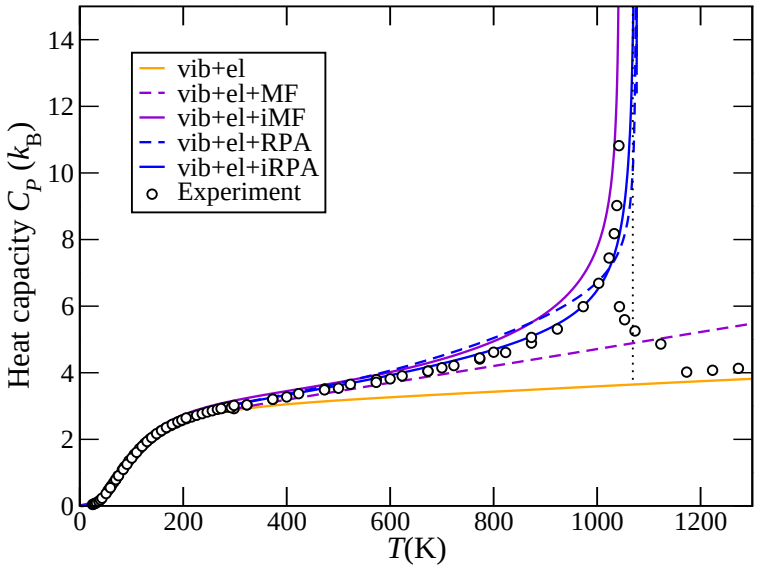

Figure 3.6: Heat capacity C_P in units of the Boltzmann constant k_B at zero pressure p as a function of temperature T. The experimental data is from [106, 107].

transversal correlation function $\langle S_{i+}S_{j-}\rangle$ has already been derived (Sec. 2.2.3) and has been proven [18, 62, 63, 108] to yield a reasonable description for low (limit of spin-wave theory) as well as high temperatures. However, an expression for $\langle S_{iz}S_{jz}\rangle$ is not directly given within the original theory proposed by Tyablikov [18]. In fact, the few years later derived expressions for $\langle S_{iz}S_{jz}\rangle$ based on similar decoupling techniques [108] reveals inconsistencies with respect to rotational invariance.[9] The underlying reason is that established Green's function truncation techniques (as e.g. the RPA decoupling) treat the transversal and longitudinal correlation function on a different level of approximation [108]. Therefore, the accuracy of any given approximation can be in general different for the spin-correlation function of the transverse and longitudinal components [108]. Many different schemes were proposed to obtain an improved description for $\langle S_{iz}S_{jz}\rangle$ (e.g. [62, 108–110]) yielding, however, a huge increase of complexity in the formalism.

However, as we will show in the following, it is still possible to obtain an accurate estimation of the longitudinal correlation with reasonable effort! In the special case of spin $S = 1/2$, exact relations to express the challenging correlation function $\langle S_{iz}S_{jz}\rangle$ in terms of $\langle S_{i+}S_{j-}\rangle$ can be employed and a $S = 1/2$ solution for the internal energy can be derived as was, e.g., shown by Tyablikov [63].[10] Therefore the RPA solution for T_C is available for $S \geq 1/2$, whereas the internal energy (mandatory for deriving the free energy) is only derived for $S = 1/2$ (see also Fig. 3.7). However, since we are interested in systems such as bcc iron, a *pure* $S = 1/2$ theory is of course insufficient (see Eq. (3.7)). To overcome this issue a rescaling factor in the $S = 1/2$ theory can be introduced affecting the exchange coefficients J^{QM} [16].

To obtain the rescaling factor we compare the known expressions for T_C. Regarding the spin dependence within the RPA, the spin dependence within $T_C(S)$ can be transferred to the exchange

[9] For example, above T_C the xx, yy and zz correlation functions are not equivalent.
[10] We present a more general derivation in the Appendix A.3.2.

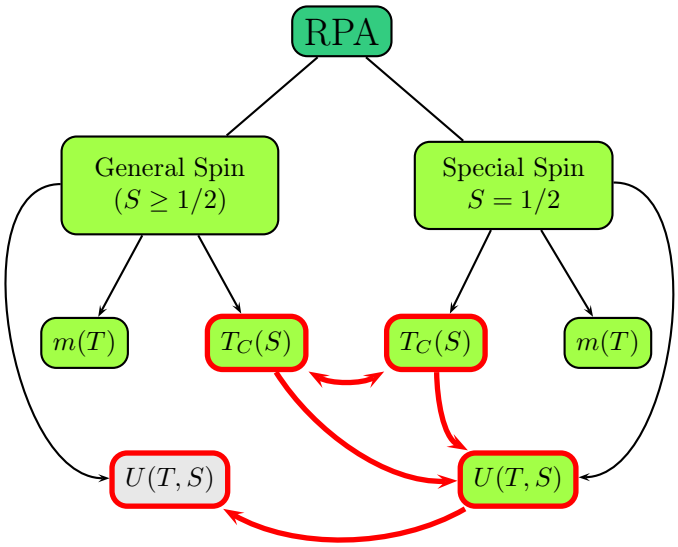

Figure 3.7: Sketch of the RPA solution for $S = 1/2$ and general spin $S \geq 1/2$. The unknown $S \geq 1/2$ solution for the inner energy (grey) is obtained by rescaling the $S = 1/2$ solution for $U(T)$. The rescaling factor is determined by the known scaling of T_C with S.

parameters as $\tilde{J} = S(S+1)J^{\mathrm{QM}}$, see Eq. (2.101). Employing the T_C formula, Eq. (2.101), for $S = 1/2$ yields:

$$k_B T_C^{S=1/2} = S\left(\sum_{\boldsymbol{q}} \frac{1}{J_{\mathbf{0}}^{S=1/2} - J_{\boldsymbol{q}}^{S=1/2}}\right)^{-1}. \tag{3.8}$$

Comparing Eq. (3.8) with the $S \geq 1/2$ expression

$$k_B T_{\mathrm{C}}^{\mathrm{RPA}} = \frac{2}{3} S(S+1)\left(\sum_{\boldsymbol{q}} \frac{1}{J_{\mathbf{0}}^{S\geq 1/2} - J_{\boldsymbol{q}}^{S\geq 1/2}}\right)^{-1} \tag{3.9}$$

we find the following expression for the effective exchange coefficients

$$\tilde{J} = S(S+1)J_{S\geq 1/2}^{\mathrm{QM}} = S J_{S=1/2}^{\mathrm{QM}}/\gamma \tag{3.10}$$

with the scaling factor $\gamma = 2/3$. Using Eq. (3.10) within the $S = 1/2$ solution for the internal energy [63] we finally end up with

$$U_{\mathrm{mag}}^{\mathrm{RPA}}(T) = U_{T=0}^{\mathrm{mag}} + \frac{M_0}{2}\sum_{\boldsymbol{q}} \frac{2m(T)[m(T)+1]\gamma\left[\tilde{J}_{\mathbf{o}} - \tilde{J}_{\boldsymbol{q}}\right]}{\exp\left[2\beta m(T)\gamma\left(\tilde{J}_{\mathbf{o}} - \tilde{J}_{\boldsymbol{q}}\right)\right] - 1} \tag{3.11}$$

where the magnetization is given by Eq. (2.98) for $S = 1/2$:

$$m(T) = \left\{1 + \frac{2}{N}\sum_{\boldsymbol{q}} \exp[2\beta m(T)\gamma(\tilde{J}_{\mathbf{o}} - \tilde{J}_{\boldsymbol{q}})]\right\}^{-1} \tag{3.12}$$

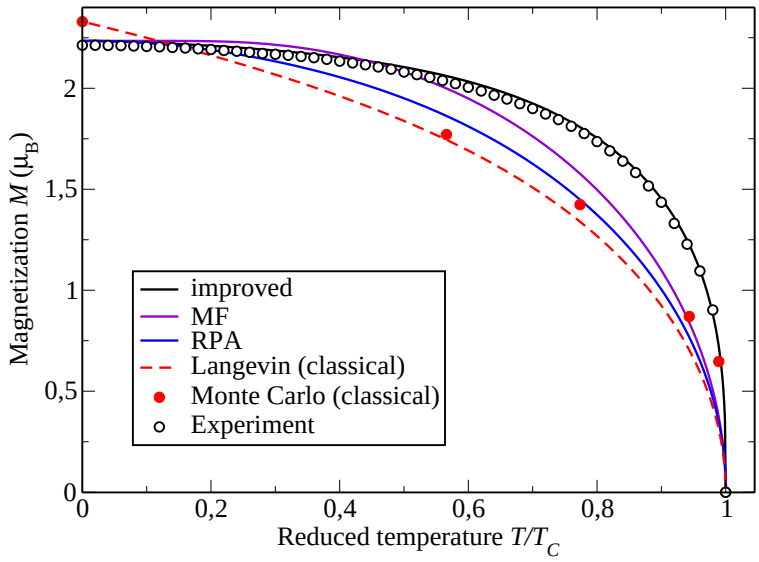

Figure 3.8: Comparison of several theoretical approximations for the magnetization $M(T) = M_0 m(T)$ in comparison with experimental data [100] and Monte Carlo calculations [43]. The results are plotted as a function of the reduced temperature T/T_C.

and the $T = 0$ contribution is given by

$$U^{\text{mag}}_{T=0} = M_0/2\gamma J_{\mathbf{0}}. \tag{3.13}$$

Employing (3.11), the description of the heat capacity is quantitatively and qualitatively improved as compared to MF indicating that RPA allows a more accurate prediction of the discontinuity of the heat capacity (second order phase transition) at T_C (see Fig. 3.6). Being proportional to the magnetization dU^{mag}/dT vanishes within both theories, MF and RPA, above T_C, which, in contrast to experiment, yields a vanishing magnetic contribution to the heat capacity C_P. Both approximations, MF and RPA, are not constructed for describing the region above T_C because these approximations do not capture the local magnetic order which is still present in this temperature region. This restriction does not, however, affect the absolute free energy as strongly as it affects its second derivative, the heat capacity. Figure 3.5 indeed reveals that the integrated RPA free energy together with F^{vib} and F^{el} deviates from the CALPHAD data by less than 15 meV at 1200 K.

Since the magnetization shape $m(T)$ is the central quantity entering the internal energies of both theories, the description of the specific heat is inherently connected with the description of $m(T)$. Therefore, we investigate next whether the remaining differences between *ab initio* and experimental data can be decreased by using an improved description of the temperature-dependent magnetization $m(T)$. The RPA relation between the magnetic internal energy $U^{\text{RPA}}_{\text{mag}}(T)$ and the magnetization $m(T)$ follows from Eq. (3.11). The fact that $m(T)$ is *the central* quantitiy appearing in Eq. (3.11) is related to the important role of $\langle S_z \rangle \sim m(T)$ within the RPA decoupling, see also Eqs. (2.96) and (2.97). In Fig. 3.8, we show the magnetization curves obtained with MF and RPA and compare them with experimental results. The classical solution found by numerically exact Monte-Carlo simulations [43] and a Langevin function are also shown for comparison. Clearly, both

approximations, MF and RPA, are not able to accurately reproduce the experimental data. Aiming at a better description of the free energy and specific heat capacity for fm bcc iron, we, therefore, use an improved magnetization curve

$$m^{\mathrm{imp}}(T) = \left(1 - s(T/T_{\mathrm{C}})^{\frac{3}{2}} - (1-s)(T/T_{\mathrm{C}})^4\right)^{\frac{1}{3}}, \tag{3.14}$$

that was empirically derived from a detailed analysis of the experimental $m(T)$ data for several ferromagnetic systems [111], and fulfills Bloch's famous $T^{3/2}$-law for low temperatures. The only free parameter s in Eq. (3.14) can be calculated using *ab initio* input [112].[11] The obtained shape of the magnetization describes perfectly the experimental data, as shown in Fig. 3.8 (black line).

The improved magnetization given by Eq. (3.14) is now used as input to U^{mag} in MF and RPA (labeled iMF/iRPA).[12] For the improved MF, the calculated specific heat capacity (violet solid line in Fig. 3.6) shows the correct qualitative behavior and comes significantly closer to experiment. Please note that for the improved MF we not only correct for $m(T)$ but also for the critical temperature T_C being significantly overestimated in MF. For the free energy, however, the deviation from experiment becomes more pronounced and even undergoes a sign reversal (Fig. 3.5). Therefore, we conclude that even an application of the improved temperature-dependent magnetization is not sufficient to account for the magnetic contribution to the free energy within MF approximation. In contrast, a noticeable improvement of both, C_P and F, is obtained for the improved RPA. The experimental heat capacity is now nearly perfectly predicted up to T_{C}. The difference between the theoretical integrated free energy with a magnetic contribution calculated with iRPA and the corresponding CALPHAD data decreases to less than 10 meV at 1200 K.

Conclusion

The big advantage of analytic approaches such as MF or RPA is that they allow physical insights into the different mechanism contributing to the magnetic contribution to the thermodynamic properties. We were, e.g., able to quantify the relation between the magnetization shape and the free energy and specific heat capacity.

However, it is also found that RPA as well as MF do not capture the short-range order above T_C properly. Reminding that the structural transition of pure iron at about 1200 K takes place just above the critical temperature $T_C = 1043$ K of bcc Fe, a careful treatment of the short-range order in iron is of particular importance. The inclusion of the short-range order in our concepts will be the content of the next sections.

[11] The calculated s=0.41 is close to the empirical value s=0.35 found by fitting Eq. (3.14) to experimental data [111]. The *ab initio* values used to calculate the theoretical s are: The ground state magnetization $M_0 = 2.23\ \mu_{\mathrm{B}}$; the spin-wave stiffness $D = 249$ meVÅ^2 obtained from the low excitation spectrum $\omega(\boldsymbol{q} \to 0) \approx Dq^2$ (which agrees with other theoretical works [15]); $T_{\mathrm{C}}^{\mathrm{RPA}} = 1082\ K$.

[12] We note that replacing $m(T)$ within MF and RPA yields to internal inconsistency of the theories. However, such an ansatz can be useful to figure out routes for improved theoretical descriptions.

3.2.2 Numerical Approaches

In the previous section two different analytic approximate solutions for the Heisenberg model were discussed. It was thus possible to get a combined *ab initio* concept, which allows a very accurate prediction of thermodynamic properties of magnetic systems up to the critical temperature. In this section we extend the methods and focus on the thermodynamic description in particular above the critical temperature. In the paramagnetic regime, i.e. $T > T_C$, the analytic approximations discussed so far (MF/RPA) are limited due to the neglect of short-range order. Consequently, one important point we would like to address in this section is to obtain a reliable prediction in particular at high temperatures. A second issue is fundamentally rooted in the approximate nature of the analytic approaches: The error due to the approximations are not known *a priori*. Clearly, a numerically exact solution to overcome these issues would be highly desirable.

The QMC introduced in Sec. 2.2.3 is a promising candidate for this purpose. However, as already discussed, its main limitation is the negative sign problem accompanied by an increase of statistical error occurring if magnetic frustration is present. As shown in Sec. 2.2.3, the effective weights $p(c)$ of these configurations c become negative. QMC simulations can still be performed by employing the absolute value $|p(c)|$ to obtain the expectation value, e.g. for the heat capacity (2.108):

$$C_V \equiv \langle C_V \rangle = \frac{\sum_c C_V(c)p(c)}{\sum_c p(c)} = \frac{\sum_c C_V(c)\mathrm{sgn}(p(c))|p(c)|/\sum_c |p(c)|}{\sum_c \mathrm{sgn}(p(c))|p(c)|/\sum_c |p(c)|} = \frac{\langle C_V \mathrm{sgn}\rangle_{|p|}}{\langle \mathrm{sgn}\rangle_{|p|}}. \tag{3.15}$$

The statistical error $\Delta\mathrm{sgn}_{|p|}$ on $\langle \mathrm{sgn}\rangle_{|p|}$ increases, however, exponentially with decreasing temperature T, Eq. (2.110). To illustrate this, we employ QMC calculations using realistic exchange parameters taken from Ref. [15]. Indeed, as shown in Fig. 3.9 (a), we observe a negative sign problem reflected in $\langle \mathrm{sgn}\rangle_{|p|}$ approaching zero for decreasing temperature, if we include more and more interaction shells. This goes along with a dramatic increase of the statistical error on $\langle \mathrm{sgn}\rangle_{|p|}$ resulting consequently in a large statistical error on C_V, Eq. (3.15), shown in Fig. 3.9 (b).

Employing (2.110)

$$\frac{\Delta\mathrm{sgn}_{|p|}}{\langle \mathrm{sgn}\rangle_{|p|}} = \frac{\sqrt{\langle \mathrm{sgn}^2\rangle_{|p|} - \langle \mathrm{sgn}\rangle_{|p|}^2}}{\sqrt{N_{\mathrm{steps}}}} \approx \frac{1}{\sqrt{N_{\mathrm{steps}}}\langle \mathrm{sgn}\rangle_{|p|}}, \tag{3.16}$$

we can estimate how much computational time a "brute force" method would take (i.e. by simply running the simulation longer and increasing the number of iteration steps N_{steps}) to achieve convergence within a reasonable statistical error. Estimating the computational time needed to reduce the statistical error given in Eq. (3.16) to less than 1% (typically needed for an accuracy of < 1 meV of free energy calculations), we end up with infeasible long calculation times in the order of thousands of years on a conventional PC (see Fig. 3.9 (c)).[13] We therefore conclude: A numerically exact quantum solution of the Heisenberg Hamiltonian using realistic exchange parameters (e.g. for bcc iron) is not feasible with the present techniques!

The question arising from the fact is, of course: If we do not have access to the numerically

[13] Conventional PC means here explicitly a computer having 2×AMD Opteron DP 250 2.4 GHz and 4 GB RAM.

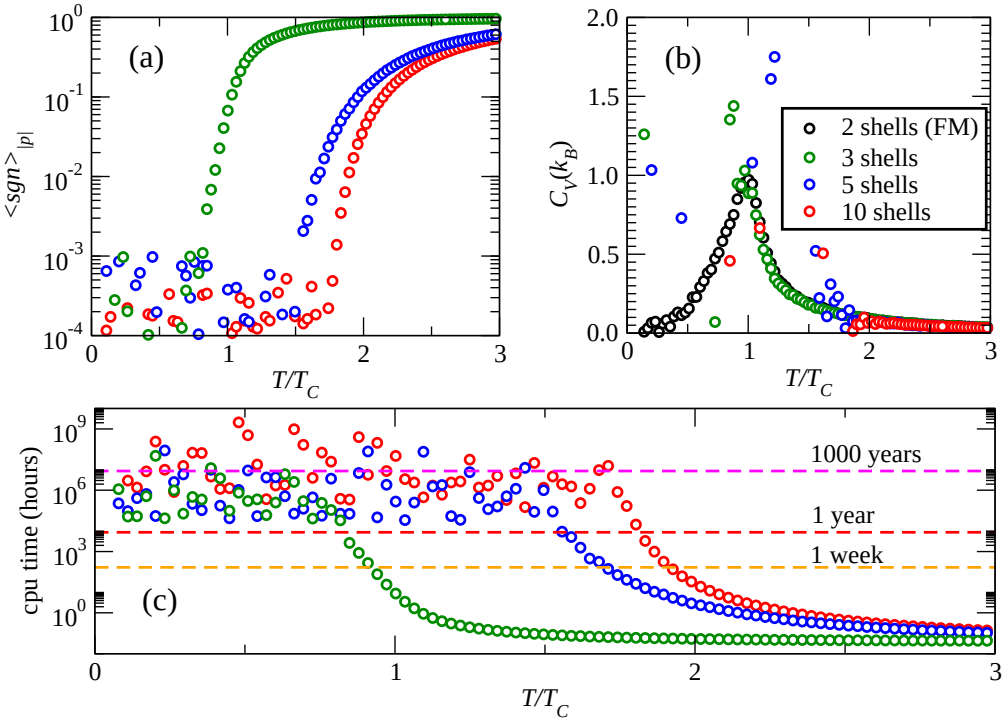

Figure 3.9: (a) Expectation value of the sign $\langle sgn \rangle_{|p|}$ for increasing number of interaction shells. (b) Corresponding heat capacity C_V. (c) Estimated CPU time on a conventional PC for 1% statistical error on $\langle sgn \rangle_{|p|}$. The exchange parameters are taken from [15].

exact *quantum* solution, how much do we gain from deriving a numerically exact *classical* solution instead? In the classical description, the total energy is directly given by

$$E^{\mathrm{CL}} = -\sum_{ij} \tilde{J}_{ij} \boldsymbol{e}_i \boldsymbol{e}_j \tag{3.17}$$

where $\tilde{J}_{ij} = J_{ij}^{\mathrm{CL}} S^2$ are the effective exchange parameters including the length $S = |\boldsymbol{S}|$ of the (continues) spin vectors $\boldsymbol{S}_i = S\boldsymbol{e}_i$ on lattice site i and $\boldsymbol{e}_i$ denoting the unit vectors. Hence, for each configuration of spins the energy (3.17) can be straightforwardly computed. The classical expectation values can be readily obtained via

$$\langle O \rangle^{\mathrm{CL}} = \frac{\sum_i O_i \mathrm{e}^{-\beta E_i^{\mathrm{CL}}}}{\sum_i \mathrm{e}^{-\beta E_i^{\mathrm{CL}}}}, \tag{3.18}$$

where the sum runs over all i possible configurations. To tackle the above equation, cMC techniques are nowadays well established. Typically, the configuration space is sampled using Metropolis importance sampling i.e. a series of configurations is generated following usually the Boltzmann statistics.

The introduced error for a classical treatment is, however, not known in advance. The critical

discussion of the limits of a classical treatment as well as the impact of quantum effects on various thermodynamic properties are in the focus of the next section.

Rescaled Classical Monte Carlo Approach

In the following we propose an alternative scheme to calculate the thermodynamic properties of magnetic Heisenberg systems where magnetic frustrations are weak or absent. The essence of the approach is a numerically exact classical Monte Carlo (cMC) solution of the (classical) Heisenberg model [Eq. (3.17)]. The quantum-mechanical effects which are neglected in the classical treatment of the originally quantum-mechanical Heisenberg model are afterwards approximately included. This inclusion is divided into two parts: On the one hand, we ensure the quantum-mechanically correct high temperature limit of the free energy by aligning the calculated classical entropy to the analytically known quantum solution. On the other hand, the impact of the neglected low temperature quantum effects is estimated by a careful comparison of model systems for which the numerically exact quantum solution via QMC calculations is also accessible (no negative sign problem). The comparison allows to formulate a semi-empirical rescaling approach (in the following denoted as rMC), which modifies the classical solution towards the quantum-mechanical counterpart. To show the performance of the method we finally combine the rMC approach with the *ab initio* computed exchange coefficients of Sec. 3.1 as well as *ab initio* vibronic and electronic free energy contributions and compare with the results obtained in the previous section.

The use of DFT based input parameters in Eq. (2.70) and the subsequent solution of the model by means of classical cMC is nowadays a standard and successful approach [13, 43, 48, 54]. Nevertheless, having in mind that quantum effects are not accounted for within the cMC approach, a number of crucial questions arises: (i) How significant are quantum effects for thermodynamic properties like, e.g. the heat capacity $C_V(T)$, the internal energy $U(T)$ or the magnetic free energy $F^{\mathrm{mag}}(T)$? (ii) Above which temperatures T and for which spin numbers S are classical calculations sufficient? (iii) Is there a practical scheme to estimate the magnitude and influence of quantum effects *without* having the quantum solution available, i.e. based solely on the classical results?

In order to tackle these questions we have evaluated the thermodynamic properties for a set of carefully selected magnetic systems using the exact QMC data as a reference and comparing them with the corresponding data obtained employing the cMC approach. This comparison provides direct insight into the importance of quantum effects as function of spin quantum number and temperature. The choice was limited to magnetically unfrustrated systems to avoid the negative sign problem in the QMC approach. We included both kinds of magnetic interactions (ferromagnetic/antiferromagnetic) for various 3D bulk lattice types (sc, bcc, fcc) and used different numbers of interaction shells (one and two shells).

To allow for a convenient comparison of the results for various spins S, and in particular for the classical limit $S \to \infty$, we use common effective exchange parameters $\tilde{J} = S(S+1)J^{\mathrm{QM}} = S^2 J^{\mathrm{CL}}$, where J^{QM} and J^{CL} are the nearest-neighbor exchange integrals respectively in the quantum and classical case. In the following we express all energies in units of $\tilde{J}$ and temperatures in units of $\tilde{J}/k_B$.

All cMC and QMC calculations were performed using the ALPS code [72]. For both calculations, cMC and QMC (the Loop algorithm [67] in the stochastic series expansion method is used), cluster

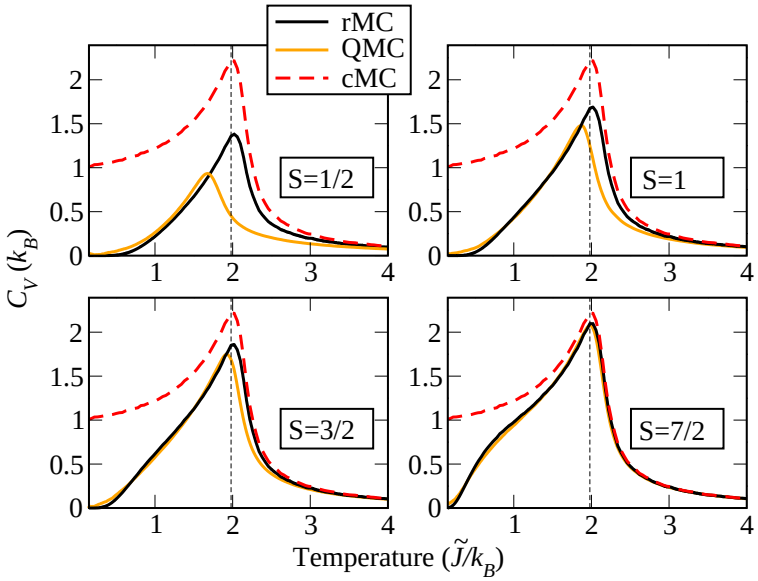

Figure 3.10: Heat capacity vs. temperature for a 8x8x8 bcc lattice with ferromagnetic nearest-neighbor coupling solved using cMC (spin-independent) and QMC for various spin quantum numbers S. For comparison the rMC data (explained in the text) is shown.

updates were employed to calculate at least $2 \cdot 10^5$ steps for equilibrating the system and $2 \cdot 10^6$ steps for thermal averaging. All supercells contained 512 atoms. For each configuration ≈ 400 temperatures were evaluated. These settings ensure statistical errors of less than $0.01 k_B$ on C_V in the considered temperature range except for the region close to the critical temperature. Increasing the supercell to 1728 atoms results in a more pronounced peak in C_V at the critical temperature, but has only a marginal effect on the formalism discussed below. In the following we illustrate our findings on the example of a bcc lattice with ferromagnetic nearest-neighbor coupling. The other investigated systems yield very similar dependencies and conclusions and will be therefore not discussed in detail here.

Within the ALPS code, the specific heat capacity C_V for cMC and QMC is calculated by virtue of the fluctuation-dissipation theorem (see, e.g. Ref. [113]) and shown in Fig. 3.10. The critical temperature T_C was determined by the position of the peak in C_V. For all considered spin quantum numbers ($S = 1/2, 1, 3/2, 7/2$), the classical and quantum solutions for C_V agree well for sufficiently high temperatures ($T \gtrsim 3\tilde{J}/k_B$). Apart from the lower spin quantum numbers, i.e. for $S > 1$, the classical approach provides even a good description of the quantum solution for temperatures above $T_C^{\mathrm{cMC}} \approx 2\tilde{J}/k_B$ implying that the short-range order (dominating in the paramagnetic regime) is well captured by the cMC approach and quantum effects have a minor impact in this temperature regime. At the same time the quantum solution of $T_C(S)$ is rapidly approaching the classical one (indicated by a dashed line in Fig. 3.10) with increasing spin: $T_C(S \to \infty) = T_C^{\mathrm{cMC}} \approx 2\tilde{J}/k_B$. For a detailed discussion of the dependence of $T_C(S)$ we refer to Ref. [114]. The fact that the classical solution for the heat capacity does not vanish for $T \to 0$ (giving rise to a diverging magnetic entropy), is a direct consequence of the classically non-discretized spectrum of magnetic excitations in the Heisenberg model.

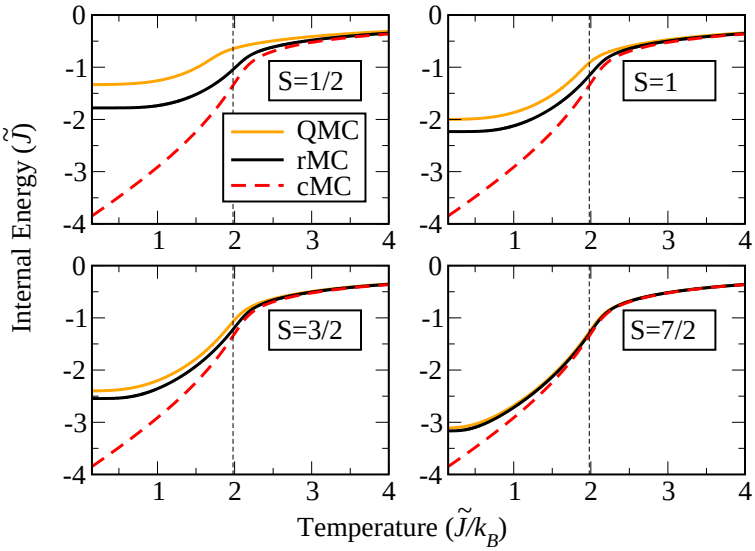

Figure 3.11: Internal energy vs. temperature for a 8x8x8 bcc lattice with ferromagnetic nearest-neighbor coupling solved using cMC and QMC for various spin quantum numbers S. For comparison the rMC data is shown.

From the numerical calculations we further obtain the internal energy shown in Fig. 3.11. The cMC and QMC results agree again for temperatures larger than $T \gtrsim 3\tilde{J}/k_B$. For lower temperatures ($T \lesssim 2\tilde{J}/k_B$) there are dramatic differences between the classical and quantum solutions for the internal energy, which increase with decreasing spin quantum numbers. The largest difference occurs at $T = 0$ and is equal to

$$U^{\mathrm{QM}}_{T=0}(S) - U^{\mathrm{CL}}_{T=0} = -(\tilde{J}_0 S/(S+1) - \tilde{J}_0) = \tilde{J}_0/(S+1) \tag{3.19}$$

with $\tilde{J}_0 = \sum_{i,j} \tilde{J}_{ij}$.

The magnetic entropy S_{m} can be directly calculated from the heat capacity via integration either starting from low temperatures ($T = 0$), or, if the maximum entropy $S^{\max}_{\mathrm{m}} = S_{\mathrm{m}}(T \to \infty)$ is known, from the high temperature limit:

$$S_{\mathrm{m}}(T) = \int_0^T C_V(T')/T' dT' \tag{3.20}$$

$$= S^{\max}_{\mathrm{m}} - \int_T^\infty C_V(T')/T' dT'. \tag{3.21}$$

For the quantum spin system represented by Eq. (2.70), the maximum entropy is spin dependent, $S^{\max}_{\mathrm{m}}(S) = k_B \ln(2S+1)$, reflecting that in the high temperature limit all $2S+1$ spin states are equally occupied.

Due to the above-mentioned non-vanishing classical heat capacity at $T = 0$, the corresponding magnetic entropy is not well defined for $T \to 0$. To compare the classical results with the quantum results, we therefore align the classical maximum entropy to the quantum one using (3.21). The corresponding calculated entropies are shown in Fig. 3.12. With decreasing temperature the entropy

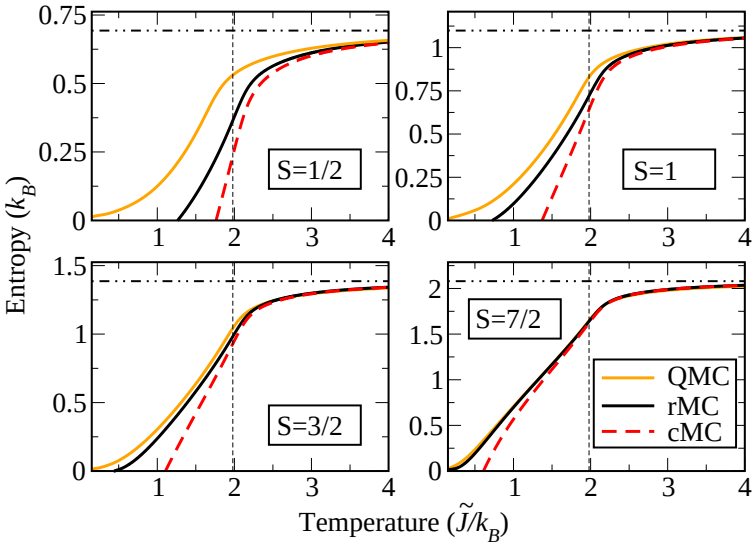

Figure 3.12: Magnetic entropy vs. temperature for a 8x8x8 bcc lattice with ferromagnetic nearest-neighbor coupling solved using cMC and QMC for various spin quantum numbers S. For comparison the rMC data is shown.

decreases from the paramagnetic limit given by $S_{\mathrm{m}}^{\max}(S)$ for fully disordered spins. Due to the treatment of spins as continues vectors, the classical solution overestimates the change in the magnetic entropy with temperature and yields a negative entropy at temperatures below a spin-dependent offset value $T^{\mathrm{off}}(S)$. The range of temperatures $T < T^{\mathrm{off}}(S)$ where cMC predicts a qualitatively wrong physical behavior of the system is shaded in Fig. 3.13 with light-grey color. Nevertheless, the alignment of the classical entropy to the quantum limit ensures that the free energy obtained with cMC for high temperatures ($T > 2\tilde{J}/k_B$) accurately reproduces the quantum solution.

Despite the aligning scheme, the cMC approach still suffers from the neglect of the quantum effects, which turn out to significantly influence the free energy data even at moderate temperatures (up to T_C). Having the importance of the classical approach for realistic materials science problems in mind, one of the central points of the present study is, therefore, the improvement of the cMC scheme in this temperature regime.

To achieve this goal we develop a mean field-based semi-empirical approach, which provides on the one hand a *practical* and efficient way to account for quantum effects and on the other hand keeps the full flexibility of the cMC scheme. We concentrate on C_V since all other thermodynamic quantities can be easily calculated once the heat capacity is known [115]. The two main deviations between the classical and quantum solution are a) the shape of C_V and b) the spin-dependence of the critical temperature. Since the latter would increase the complexity of our approach, we introduce a normalized temperature $t = T/T_C$ and focus on the deviations regarding the shape as a function of temperature and spin quantum number. These can be expressed in a compact form by introducing

$$f(t, S, \sigma) := C_V^{\mathrm{QMC}}(t, S, \sigma)/C_V^{\mathrm{cMC}}(t, \sigma), \tag{3.22}$$

where σ includes other dependencies apart from S and t, such as, e.g. the lattice and/or magnetic

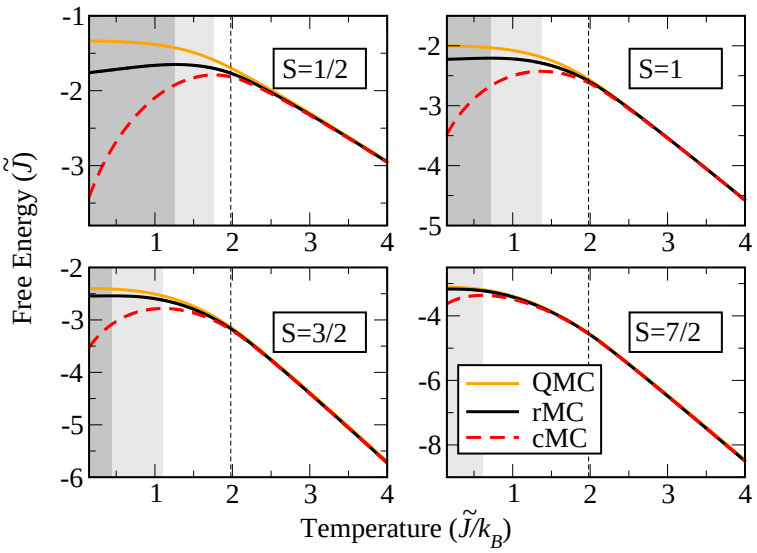

Figure 3.13: Free energy vs. temperature for a 8x8x8 bcc lattice with ferromagnetic nearest-neighbor coupling solved using cMC and QMC for various spin quantum numbers S. For comparison the rMC data is shown. The range where the magnetic entropy of the aligned cMC and the rMC data becomes negative is highlighted by light and dark grey shading, respectively.

configuration (e.g. number of interaction shells). In principle, if f were known, C_V^{QMC} could be computed solely based on the classical C_V^{cMC} solution. A numerical estimate of f can be obtained for the model systems such as those considered in Fig. 3.10, but is not available for configurations present in realistic material systems such as bcc iron.

To analyze the shape and functional dependence of the scaling function f we compute this ratio between the quantum-mechanical and the classical heat capacity for an extensive set of model systems for which QMC results are accessible. The set of chosen configurations σ includes different lattice structures (sc, bcc, fcc) with nearest-neighbor ferromagnetic configurations ($J_1 > 0$) as well as antiferromagnetic configurations ($J_1 < 0$) for bcc and sc [116]. To check the robustness of the approach, we additionally included ferromagnetic configurations with second-nearest-neighbor interactions taking $J_2 = 2.5J_1 > 0$ and $J_2 = 5J_1 > 0$. The numerical results of Eq. (3.22) for two different spins, $S = 1$ and $S = 7/2$, are shown in Fig. 3.14. They show a significant scatter for high temperatures, where the quantum and classical solution should coincide, $f(t \gg 1) \to 1$. This is due to $C_V(t \gg 1) \to 0$ [see Eq. (3.22)] and the connected increase of the statistical errors. For the more important regime below $t = 1$, however, the influence of σ on the function f is surprisingly weak and significantly smaller as compared to that of S and t.

The observed weak dependence of the function f on the specific configuration σ that includes besides the crystal structure and magnetic state, also the range of interaction, is a central insight of this study and allows to neglect the σ dependence in first order. For a practical realization of this scheme we determine the averaged scaling function $\overline{f}(t, S)$ that averages over all considered configurations. This function is expected to provide a good approximation also for realistic material systems, which have not been included in the current set of structures (e.g. due to the not accessible QM solution). A practical example will be given in Sec. 3.2.2 for the material system bcc iron. For

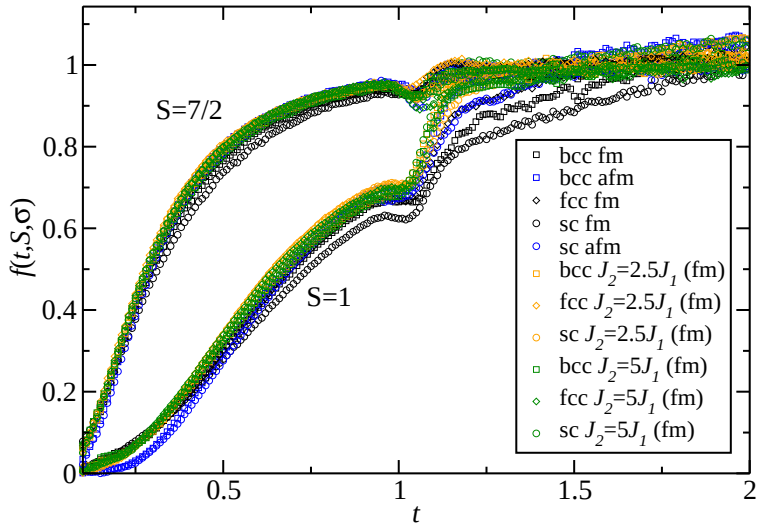

Figure 3.14: Numerically evaluated $f(t, S, \sigma)$ ratio (symbols) [see Eq. (3.22)] vs. temperature for two spins $S = 1$ and $S = 7/2$ and various σ (lattice/magnetic configurations). Symbols: (circles, squares, diamonds)=(sc, bcc, fcc); colorcode: (black, blue, orange, green)=(fm, afm, $J_2 = 2.5J_1$ (fm), $J_2 = 5J_1$ (fm)).

an easy implementation of this approach an analytical expression for $\overline{f}(t, S)$ is desirable. In the following we discuss an empirical ansatz for this function, and test its accuracy/limits by comparing the rescaled cMC data based on the empirical ansatz with numerically exact results.

We start this discussion by considering the mean-field approximation of the Heisenberg model, which is known to describe thermodynamic properties at low temperatures reasonably well (see, e.g. Figs. 3.5- 3.8). An advantage of this approximation is the availability of analytical expressions for the magnetization in the quantum (Brillouin function) and in the classical (Langevin function) case. The resulting ratio of heat capacities, $f^{\mathrm{MF}}(t, S)$, can therefore straightforwardly be computed. The shape of $f^{\mathrm{MF}}(t)$ is in good agreement with that of f in the low temperature regime except of a scaling factor due to the well known overestimation of T_C in the MF approximation. To elaborate this in more detail we analytically expand the low temperature MF ratio (see Appendix A.1.3) and obtain

$$f^{\mathrm{MF}}(t \ll 1, S) \approx \left(\frac{2t_S/t}{\exp(t_S/t)} \right)^2 \tag{3.23}$$

with the spin-dependent temperature

$$1/t_S = \alpha(S + 1). \tag{3.24}$$

α is a proportionality factor. Its MF value is $\alpha^{\mathrm{MF}} \equiv 2/3$.

For temperatures above the critical temperature ($t > 1$) MF predicts $C_V \equiv 0$ due to the neglect of short-range order. Therefore, the analytic function Eq. (3.23) needs to be extended by an additional term, such that the resulting empirical function f^{approx} fulfills the following boundary conditions: First, for high temperatures both solutions (quantum and classical) should coincide, i.e. $f^{\mathrm{approx}}(t \to \infty, S) \to 1$. Second, the same should hold for an infinite spin quantum number, i.e. $f^{\mathrm{approx}}(t, S \to$

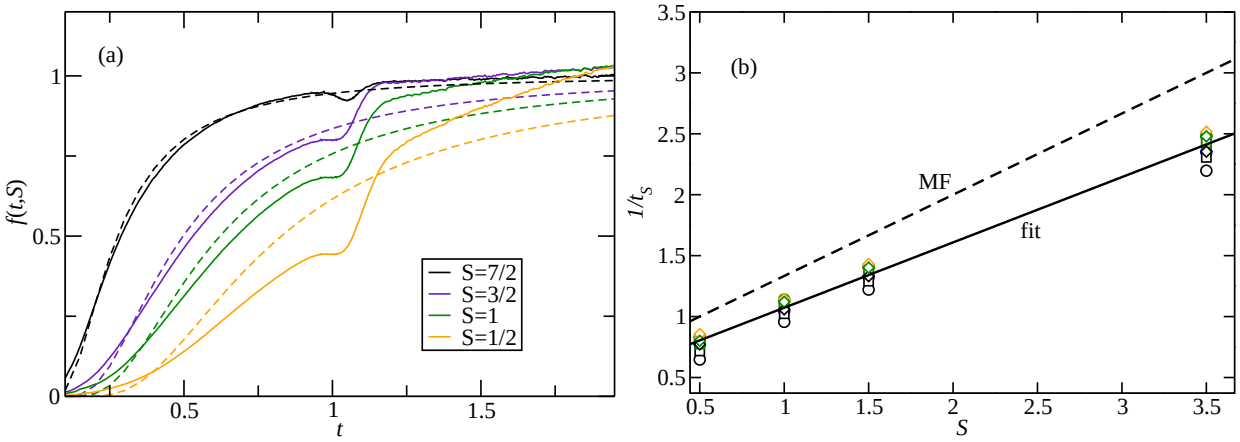

Figure 3.15: (a) Averaged data from Eq. (3.22) for different spin quantum numbers S of a bcc nearest-neighbor ferromagnet calculated using $\approx$ 400 temperature steps (solid lines) and corresponding fit $f^{\text{approx}}(t,S)$ obtained using Eq. (3.25) (dashed lines). (b) Linear relation of $1/t_S$ versus spin S. Symbols: (circles, squares, diamonds)=(sc, bcc, fcc); colorcode: (black, blue, orange, green)=(fm, afm, $J_2 = 2.5J_1$ (fm), $J_2 = 5J_1$ (fm)).

$\infty) \rightarrow 1$, reflecting that the classical model converges to the QM model in the limit of an infinite spin S. The choice

$$f^{\text{approx}}(t,S) \quad := \quad \left(\frac{2t_S/t}{\exp(t_S/t) - \exp(-t_S/t)}\right)^2 \tag{3.25}$$

obeys both conditions and provides a good fit of the data as will be discussed next.

In a second step we fit the numerically exact scaling data Eq. (3.22) to the functional dependence of Eq. (3.25), using t_S as fit parameter. This procedure has first been performed for each of the investigated spin quantum numbers S, each structure (sc, bcc, fcc) and magnetic configuration ($J > 0$, $J < 0$, $J_2 = 2.5J_1 > 0$, $J_2 = 5J_1 > 0$) individually. As can be seen from Fig. 3.15 (b), the used fitting function again appears to be remarkably independent of the configuration σ. Regarding the dependence on S, the parameter $1/t_S$ turns out to be nearly linearly proportional to the spin quantum number, similarly to MF in Eq. (3.24). This is consistent with the observation that the characteristic temperature above which the cMC and the QMC solution agree is inverse proportional to S. Performing a linear regression over all calculated datasets for different systems yields

$$1/t_S \approx 0.54(1)S + 0.54(2), \tag{3.26}$$

close to the mean field value as given by Eq. (3.24). The mean deviation on the last digit is shown in brackets.

The quality of the analytical expressions for the rescaling functions Eqs. (3.25) and (3.26), is demonstrated in Fig. 3.15 (a). Here, we observe for all considered parameters a fair agreement between $\overline{f}(t,S)$ and $f^{\text{approx}}(t,S)$, with the smallest deviations for low temperatures t and high spin values S. In order to test the accuracy of this approach, we apply the rescaling scheme to the previously discussed cMC data of model systems. This allows a direct comparison of the temperature

dependences obtained by the two-step procedure (fitting+linearizing $1/t_S$) resulting in $f^{\text{approx}}(t, S)$ with the numerically exact QMC results. In contrast to Fig. 3.15 (a), it has been performed for all σ individually and would only be trivial if the rescaling function $f(t, S, \sigma)$ were used. Since in practice the quantum solution is usually not known *a priori*, we also do not align the classical and quantum solution with respect to the temperature, i.e. we do not enforce $T_C^{\text{rMC}} = T_C^{\text{QMC}}$. As an example we show the heat capacity for the bcc, ferromagnetic nearest-neighbor case (black line in Fig. 3.10). For all spin quantum numbers the classical results are found to be significantly improved. A similar accuracy is found for all other considered systems.

Based on the rescaled heat capacity we compute, similar to Eq. (3.21), the internal energy

$$U^{\text{rMC}}(T) = U^{\text{cMC}}(T_H) - \int_T^{T_H} C_V^{\text{rMC}}(T) dT. \tag{3.27}$$

Here we have used that $U^{\text{cMC}}(T_H) \approx U^{\text{QMC}}(T_H)$ and $C_V(T_H) \approx 0$ for sufficiently high cutoff temperatures $T_H > T_C$. The rescaled internal energy Eq. (3.27) and the rescaled entropy Eq. (3.21) are compared in Figs. 3.11 and 3.12 with the cMC and QMC results. Altogether, the classical description is again improved for all considered spin quantum numbers and thermodynamic properties. As expected, deviations are larger for small spin quantum numbers (e.g. $S = 1/2$) (see Fig. 3.10). A major source for the remaining discrepancies are the deviations between the Curie temperatures for small spins and in the classical limit $S \to \infty$ [114]. In general, with increasing spin number the predictive accuracy of rMC improves and already for $S \geq 3/2$ the results are very close to the full QMC calculations. A similar behavior is found for the internal energy and magnetic entropy.

Generally we find that the rescaling approach consistently improves the problematic low temperature regime. For integrated quantities such as the entropy, internal, and the free energy, the remaining errors accumulate in the low temperature region due to the backward integration from high to low temperatures by virtue of Eqs. (3.21) and (3.27). A consequence is the presence of unphysical negative entropies at low temperatures (dark shaded temperature range in Fig. 3.13) similarly to the purely classical approach (light shaded temperature range in Fig. 3.13), despite the good description of the rescaled heat capacity both at low and high temperatures with the largest deviations close to the critical temperature.

To quantitatively evaluate the accuracy achievable by the rescaling approach we summarize in Tab. 3.2 the mean deviation in percent (standard deviation of the various structures shown in brackets) between the rMC (first rows) and the cMC (second rows) with the QMC data for different temperature ranges and averaged over all model structures σ considered in this study. For low temperatures (below the critical temperature) the aligned cMC approach is not sufficient to describe the quantum system whereas the rMC approach provides already for $S \geq 1$ a good approximate prediction of the quantum-mechanical free energy with an error of less than 4%. For higher temperatures (above the critical temperature) the rMC reduces the deviations between the cMC and the QMC data for all thermodynamic quantities by almost a factor of two. The fact that the scatter between the different structures, as reflected in the standard deviation shown in Tab. 3.2, is almost always smaller than the mean deviation and that it consistently decreases with S, indicates that the rescaling approach works equally well for all investigated lattice types, magnetic configurations, and number of included interaction shells. We, therefore, expect a similar accuracy

Table 3.2: Mean value of the mean deviation between the rMC/cMC and the QMC calculations for the heat capacity, internal energy, entropy, and free energy in percent using $\Delta A = 1/N_\sigma \sum_{N_\sigma} \Delta A^\sigma$ with $\Delta A^\sigma = 1/N \sum_{t_i} \left| (A_\sigma^{\mathrm{rMC/cMC}}(t_i) - A_\sigma^{\mathrm{QMC}}(t_i))/A_\sigma^{\mathrm{QMC}}(t_i) \right|$ with $N = 100$ in two temperature regimes for all structures σ (sc, bcc, fcc; fm, afm, $J_2 = 2.5J_1$ (fm), $J_2 = 5J_1$ (fm)). The standard deviation of the different structures is shown in brackets.

		$0.1 < T/T_C^{\mathrm{cMC}} < 1$			
	ΔA	$S = 1/2$	$S = 1$	$S = 3/2$	$S = 7/2$
$A = C_V$	rMC	41.2(7.1)	21.9(4.3)	15.8(2.9)	5.5(2.0)
	cMC	1897.3(951.9)	885.5(413.8)	533.3(171.4)	112.3(12.1)
$A = U$	rMC	32.2(11.9)	9.8(5.4)	4.3(3.4)	1.0(1.2)
	cMC	125.5(17.9)	53.9(6.2)	31.5(3.4)	9.(1.0)
$A = S_{\mathrm{m}}$	rMC	226.2(81.0)	48.9(42.8)	28.2(32.7)	9.3(10.3)
	cMC	3630.(1614.4)	1810.3(646.4)	1087.4(343.0)	223.1(57.0)
$A = F$	rMC	12.8(5.0)	3.9(2.2)	1.7(1.4)	0.7(0.7)
	cMC	49.3(6.2)	20.8(2.3)	11.9(1.3)	3.4(0.6)
		$1 < T/T_C^{\mathrm{cMC}} < 2$			
	ΔA	$S = 1/2$	$S = 1$	$S = 3/2$	$S = 7/2$
$A = C_V$	rMC	49.8(25.9)	15.2(9.7)	7.1(5.2)	2.2(3.4)
	cMC	99.7(34.8)	33.4(11.3)	16.9(5.6)	3.7(1.4)
$A = U$	rMC	14.1(9.5)	5.2(4.2)	2.7(2.6)	1.1(1.8)
	cMC	25.7(10.4)	10.7(4.2)	5.9(2.3)	1.5(0.6)
$A = S_{\mathrm{m}}$	rMC	3.7(3.1)	1.3(1.3)	0.8(0.8)	0.7(0.5)
	cMC	6.5(3.3)	2.2(1.4)	1.1(0.8)	0.6(0.5)
$A = F$	rMC	1.1(0.8)	0.5(0.3)	0.5(0.3)	0.6(0.4)
	cMC	1.5(0.9)	0.7(0.4)	0.6(0.4)	0.7(0.4)

of the proposed rescaling approach for other lattice geometries and if interaction shells beyond second-nearest-neighbors are included.

Application of the rMC Approach to FM Bcc Iron

In the following we employ the rMC approach to compute the magnetic contribution of bcc iron as an example of a realistic magnetic material system. Despite its predominant ferromagnetic coupling, positive (i.e. antiferromagnetic) exchange integrals occur in higher-order shells. These exchange integrals cannot be neglected due to the very long-ranged character of the interactions [15] and lead to weak magnetic frustrations which rule out the use of the QMC approach (see also Fig. 3.9) [117].

To compute the thermodynamic properties we use the adiabatic approximation (3.4). In Fig. 3.16 we show once more the sum of F_{vib} and F_{el} and compare it with CALPHAD [86, 87] data. The strong deviations between the calculated and the experimental free energy and heat capacity (Fig. 3.17) above room temperature highlight the significance of magnetic contributions, as we already discussed in Sec. 3.2.1 [16].

In order to evaluate the magnetic contribution, we start with the comparison of the classical

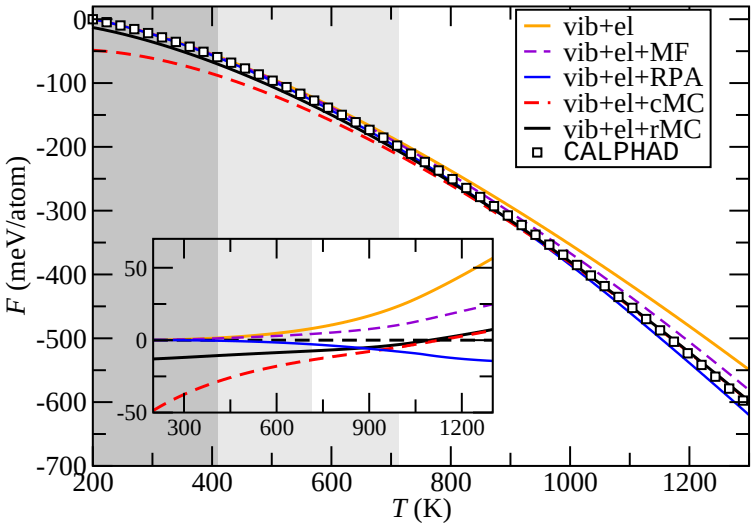

Figure 3.16: The free energy of bcc iron as a function of temperature. Inset: Difference between the different theoretical and the CALPHAD data is shown. For comparison the theoretical MF and RPA results of Sec. 3.2.1 are also shown.

Monte Carlo calculations and the rMC data for the specific heat capacity (Fig. 3.17). Classical Monte Carlo calculations were performed using a 12x12x12 supercell (containing 1728 atoms) including magnetic interactions of up to 25 neighbor shells. The effective real-space exchange coefficients $\tilde{J}_{ij}$ entering the Heisenberg model have been obtained by performing a Fourier transformation of the reciprocal-space exchange integrals, which we have already extensively discussed in Sec. 3.1. The magnetic heat capacity is calculated assuming that the magnetic moments of Fe do not significantly change due to the thermal volume expansion and temperature, resulting in $C_V(T) \approx C_P(T)$. We now add the magnetic contribution to $C_P(T)$ (Fig. 3.17). The peak in the heat capacity (Fig. 3.17) reflects the magnetic transition from the ferromagnetic to the paramagnetic state. The resulting critical temperature is $T_C^{\mathrm{cMC}} \approx 1060$ K which is close to the experimental value $T_C^{\mathrm{exp}} = 1044$ K and similar to the analytic result $T_C^{\mathrm{RPA}} = 1083$ K (Sec. 3.1). In the paramagnetic regime the cMC approach reproduces the experimental behavior very well, confirming our finding in the previous section that magnetic short-range order is well captured within the cMC calculations (for $S > 1$) and that quantum effects are not critical in this temperature regime (see also Fig. 3.10).

To obtain $F_{\mathrm{mag}}^{\mathrm{cMC}}$ we use the calculated cMC internal energy U^{cMC} and the classical entropy S_m^{cMC} aligned to the maximum entropy $S_{\mathrm{m}}^{\mathrm{mag}}(S)$ for the quantum spin system at high temperatures [see Eq. (3.21)]. The effective spin quantum number $S = 1.1$, which corresponds to the *ab initio* calculated ground-state magnetic moment 2.2 μ_B, is used. In order to obtain the magnetic excitation energies (the $T = 0$ K-energy is already included in F_{el}), the $T = 0$ K contribution $U_{T=0}^{\mathrm{QM}}(S)$ is subtracted from the calculated $F_{\mathrm{mag}}^{\mathrm{cMC}}$ after the alignment of F and the CALPHAD data.[14] The resulting free energy F^{cMC} is shown in Fig. 3.16. The obtained agreement at high temperatures is excellent.

[14] As discussed above, the classical treatment of the quantum Heisenberg Hamiltonian fails in particular at low temperatures where, however, the computed free energies are typically aligned to CALPHAD data (i.e. 200 K) for comparison. After the alignment we, therefore, subtract the deviation caused by the neglected quantum effects employing $\Delta F^{\mathrm{DFT-CALPHAD}}(200\ K) = F_{\mathrm{cMC}}^{\mathrm{DFT}}(200\ K) - F^{\mathrm{CALPHAD}}(200\ K) := U^{\mathrm{QMC}}(200\ K) - U^{\mathrm{cMC}}(200\ K) \approx \tilde{J}_0/(S+1)$,

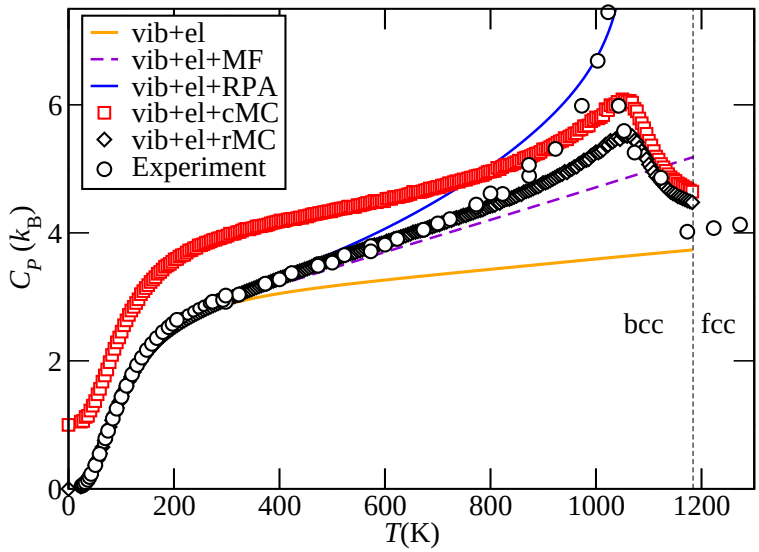

Figure 3.17: Heat capacity vs. temperature for the different theoretical data vs. experiment. The experimental transition temperature (bcc → fcc) $T^{\alpha\gamma} \approx 1184$ K is indicated by a dashed line. For comparison the theoretical MF and RPA results of Sec. 3.2.1 are also shown.

Above the critical temperature, the aligned cMC free energy provides a very good description of the magnetic contribution to the free energy of bcc iron. At lower temperatures, however, the deviations are clearly visible and increase in magnitude with decreasing the temperature. Below ≈ 700 K the aligned cMC entropy becomes negative (highlighted by light grey color), which leads to a wrong asymptotic behavior of the calculated free energy. This region is, therefore, not properly described within the cMC ansatz, although quantitatively the deviations of F^{cMC} from the experimental data remain moderate even at temperatures below 700 K.

We use now the rescaling framework and multiply the cMC data for $C_P(T)$ with the rescaling function given by Eqs. (3.25)-(3.26). The results are shown in Fig. 3.17 (black diamonds) and reveal a significant improvement over the cMC results below the room temperature, yielding an overall excellent agreement of the calculated heat capacity with the available experimental data. The largest deviations occur close to the critical temperature where the finite size effects in the MC calculations hinder an accurate description of the heat capacity in the thermodynamic limit of infinite system size $L \to \infty$ [118]. Applying our rescaling ansatz to the cMC entropy and internal energy we derive the rMC free energy (black straight line in Fig. 3.16). As can be seen, our rescaling approach provides an accurate agreement with the experiment with an error bar of less than 10 meV/atom over the whole temperature range of thermodynamically stable bcc iron. We note that the temperature below which the rMC entropy becomes negative (indicating the breakdown of this approach) is significantly shifted by ≈ 300 K to lower temperatures (marked by the dark shaded region) when compared to the aligned cMC. The results show that the rescaling

see (3.19). In the last step $U^{\mathrm{QM}}_{T=0\ K} \approx U^{\mathrm{QM}}_{T=200\ K}$ is assumed due to the negligible contribution of $C_P(T < 200K) \approx 0 = dU/dT$.

procedure is indeed able to correct for the cMC deficiencies in the low temperature ($T < T_C$) regime and lead to a significant decrease of the errors in the calculated thermodynamic properties.

Conclusion

Classical MC calculations employing realistic magnetic exchange coefficients can be used to accurately determine the Curie temperature T_C as well as to account for magnetic short-range order *above* T_C. The numerical treatment provides therewith a complementary approach in particular to the analytic RPA method (accurate description in the ferromagnetic regime *below* T_C) enabling us to describe bcc iron over the whole temperature range. Below T_C, the cMC method is not sufficient to describe the quantum Heisenberg model. This implies that quantum effects are important even up to T_C, which is in case of bcc Fe already above 1000 K!

The almost universal behavior of the derived rescaling function for the different tested model systems indicates that the overall shape of thermodynamic quantities, such as the specific heat capacity, are largely independent on the specific magnetic configuration *if* considered on a reduced temperature scale. This insight provides the basis for an effective model discussed in Sec. 3.4.

Having tested and verified the developed methods for bcc iron we proceed in the next section with the investigation of fcc iron. A major aim is to resolve the fundamental question of the underlying driving forces of the bcc - fcc phase transitions.

3.3 Structural Phase Transitions in Iron

So far we have concentrated our discussion in particular on *the magnetic transition* in bcc iron, i.e., the transition from the ferromagnetic to the paramagnetic regime at the Curie temperature T_C (lower part in Fig. 3.18). We have developed highly efficient methods to incorporate the magnetic entropy contribution into a combined *ab initio* framework for a parameter-free prediction of the free energy $F(T)$. Since this procedure can be applied to several phases, it now provides the possibility to investigate even *structural phase transitions*.

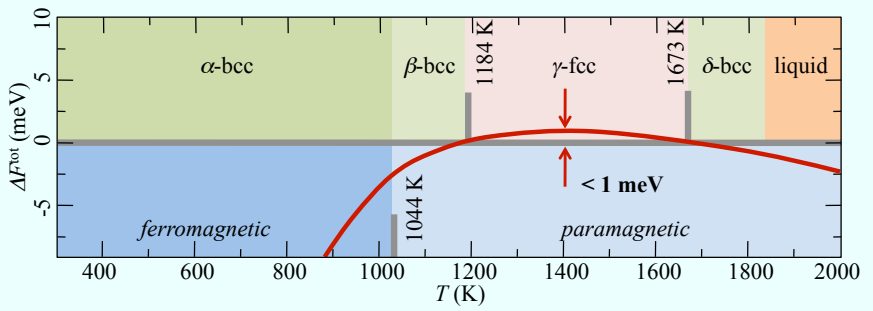

Figure 3.18: The CALPHAD [119] free energy difference ΔF^{tot} between the bcc and fcc phase is shown (red line). For $\Delta F^{\text{tot}} < 0$ the bcc phase is more stable than the fcc phase and for $\Delta F^{\text{tot}} > 0$ vice versa.

The structural transitions in pure iron have been intensively investigated from experimental as well as theoretical sides for more than half a century [7, 8, 120–123]. However, due to the complexity involved in the magnetic degrees of freedom, a full theoretical understanding is still lacking. One of the key issues is the detailed balance between the various entropy contributions and their impact on the structural stability of the bcc and fcc phase, resulting in questions such as: are phonon excitations the driving force of the bcc to fcc transition [120] or are magnetic contributions playing the more significant role [8]? Based on pure geometry one could argue that phonon excitations in a more open structure are softer than in a more close packed lattice structure and that consequently the vibronic entropy should stabilize the bcc structure at high T. If we accordingly assume that vibronic contributions are the driving force for the second transition ($\gamma \rightarrow \delta$), the magnetic contributions are consequently responsible for the first one ($\alpha \rightarrow \gamma$). However, a solely geometric argumentation ("more open structure") does not necessarily apply to magnetic systems, where for instance the amplitude of phonons sensitively depends on the magnitude of the local magnetic moments [124].

As mentioned in the beginning, the bcc-fcc phase transitions in iron were investigated by many authors over the last fifty years: In 1956, within a CALPHAD-type assessment of experimental data, Weiss and Tauer [120] demonstrated the importance of vibronic contributions for the stabilization of the fcc phase. Later, in 1963, Kaufman *et al.* [7] suggested the existence of two spin states in fcc Fe (called ferromagnetic high-spin and low-spin state), which yield an additional entropy contribution which is responsible for the stabilization of the fcc phase (sometimes also denoted as the

phenomenological two-state-hypothesis).[15] Twenty years later, Hasegawa and Pettifor [8] proposed a purely theoretical ansatz based on a mean field single-band Hubbard model. In this way they were able to show that *both* phase transitions could be explained qualitatively solely by magnetic contributions. However, the proposed theory included a number of approximations (no spin-wave contributions, ignoring short-range order, etc.) and a final answer regarding the impact of magnetic contributions compared to the vibronic ones was not possible. Instead, a few years later, Zarestky and Stassis reanimated the discussion of the impact of vibronic contributions by performing neutron scattering experiments for annealed fcc iron [122]. Based on these experiments, the Debye temperature of fcc Fe was estimated to be about 25% below the bcc Fe Debye temperature strengthening the initial CALPHAD evaluation of Weiss and Tauer. In 2010, Lavrentiev *et al.* [125] employed a newly developed magnetic cluster expansion [126] to investigate the phase transitions in iron. The authors combined the computed magnetic entropy with *empirically* derived vibronic contributions[16] and were able to reproduce the experimentally observed phase transitions. Their approach relies, however, on a number of assumptions as well as experimental input.[17] Furthermore, important contributions such as the electronic entropy were neglected. A fully theoretical understanding of the impact of different contributions (electronic, vibronic, and magnetic) on the phase transitions is obviously not yet established.

The following section is divided into two parts: The first part is devoted to the treatment of the fcc phase. Previous DFT calculations reveal a non-collinear spin spiral ground state for fcc iron (see e.g. Ref. [19]). In this case, the developed RPA theory in Sec. 3.2.1 needs to be extended and generalized to non-collinear magnetic configurations. We apply the more general analytic expression as well as the rescaled Monte Carlo approach from Sec. 3.2.2 to fcc Fe and compare them with each other. The results are further combined with vibronic and electronic entropy contributions and compared with the results obtained by the CALPHAD approach. Having obtained a reliable prediction of the fcc phase, we discuss in the second part in detail the temperature dependent free energy difference of both phases, $\Delta F_{\mathrm{bcc-fcc}}$, as well as the impact of the various entropy contributions.

3.3.1 Thermodynamics of γ-Iron

The experimental investigation of the fcc phase of iron is complicated due the fact that it is thermodynamically stable only in a rather high and narrow temperature window between 1184 K and 1673 K, see Fig. 3.18. Experimentally fcc iron is stabilized mostly in combination with fcc Cu, e.g., by annealing Fe alloys in Cu (forming Fe precipitates of the parent (fcc Cu) lattice structure) [128–130] or by epitaxial growth of thin Fe layers on Cu(001) (up to a critical layer thickness) [131–138].

[15] We note that although the existence of the two spin states is nowadays well established by electronic structure calculations, see e.g. Ref. [121], it is usually not considered as an additional source of entropy.

[16] The contribution of bcc Fe is derived from experimental elastic constant measurements at 1173 K [127]. For fcc Fe, a force-constants model is employed to fit experimental inelastic neutron scattering data taken at 1428 K [122].

[17] Concerning the magnetic model, the long-ranged exchange interactions are ignored and only the first two (three) nearest-neighbor exchange coefficients for bcc (fcc) Fe are included. The error introduced due to the classical treatment of the magnetic Hamiltonian is not known and also not discussed by the authors. The vibronic contribution is determined by fitting experimental data at *fixed* temperature which is even not the same for the bcc and fcc phase. The dependence of the vibronic contribution on volume and temperature is not included. Finally, the electronic entropy is completely neglected.

For precipitates sizes up to 150 $\mathring{A}$, a simple type-I antiferromagnetic (afm) structure is found [139]. In the ultrathin films, a nonmonotonous variation of the magnetization was found, which was assigned to the formation of a helical spin-wave (characterized by $Q^{\text{exp}} = 2\pi/a(0.1, 0, 1)$) in the deeper layers being close to an afm configuration $Q^{\text{afm}} = 2\pi/a(0, 0, 1)$ in (001)-direction. The experimental results (for the precipitates as well as the layered structures) show a strong tendency of antiferromagnetic order accompanied with potential distortions (modulations) depending in a crucial way on the external constraints (e.g. the experimental film growing technique or precipitate size).

To investigate the magnetic ground state of fcc iron, several DFT studies have been performed, see e.g. Ref. [19] and references therein. Regarding collinear magnetic configurations [121], ferromagnetic high-spin and low-spin phases are found to be energetically more stable than the nonmagnetic (nm) phase. The lowest energies are found for antiferromagnetic phases, in particular for the antiferromagnetic single-layer (afm) and antiferromagnetic double-layer (afmd) configurations in (001)-direction. In a previous work [19], which includes different spin spiral configurations in the total energy calculations, two local energy minima are found for spin spirals $Q_1 = 2\pi/a(0.2, 0, 1)$ (close to the experimental one found in ultrathin films, see above) and $Q_2 = 2\pi/a(0, 0, 0.6)$. At rather low volumes (about 7% lower than the experimental volume) the spin spiral state Q_1 turns out to be more stable than Q_2, whereas for larger volumes the latter is found to be energetically more favorable.

To compute the magnetic entropy we employ in the following a theory similar to bcc Fe, which covers the *full* Q-space, i.e., the energies corresponding to all possible spin spiral configurations. Therefore, similar calculations as in [19] are performed. Regarding the vibronic entropy, phonon calculations for different spin spirals may become computational very expensive[18]. We, therefore, perform phonon calculations in two representative collinear phases, i.e., the afm and afmd phase discussed above.

Ground-state Properties

We first consider the $T = 0$ K total energy calculations for various magnetic phases (including the above introduced afm and afmd phase) of fcc Fe in Fig. 3.19. For the considered collinear magnetic phases, the afmd phase represents the energetically lowest magnetic structure. We performed in addition total energy calculations for different non-collinear spin spiral structures Q and find that the Q_2 structure is lower in energy than the collinear phases in the considered volume range. We note, however, that all magnetic phases are very close in energy indicating that the specific magnetic arrangements of the magnetic moments in fcc Fe have only small influence on the total energy compared to bcc Fe, see Fig. 3.19. Since the energy difference ΔE between the fm and afm phase is in first order approximation[19] proportional to the nearest-neighbor exchange coefficient $\tilde{J}_{12}$, the magnetic exchange in fcc Fe ($\Delta E \approx 50$ meV≈ 580 K$\cdot k_B$) is about one order of magnitude smaller than in bcc Fe ($\Delta E \approx 450$ meV≈ 5200 K$\cdot k_B$).

[18] For the spiral state $Q_2 = 2\pi/a(0, 0, 0.6)$ at least 10 atomic layers in the (0,0,1)-direction are required to construct the unit cell. In addition, the symmetry breaking in non-collinear calculations renders such calculations to be at least one order of magnitude more expensive than common collinear phonon calculations.

[19] For a classical Heisenberg system defined by the energy $E = 1/N \sum_{ij} J_{ij} \vec{e}_i \vec{e}_j$, the energy difference at $T = 0$ K between the fm and afm configuration is $\Delta E = \sum_j J_{1,2j} \approx J_{1,2}$.

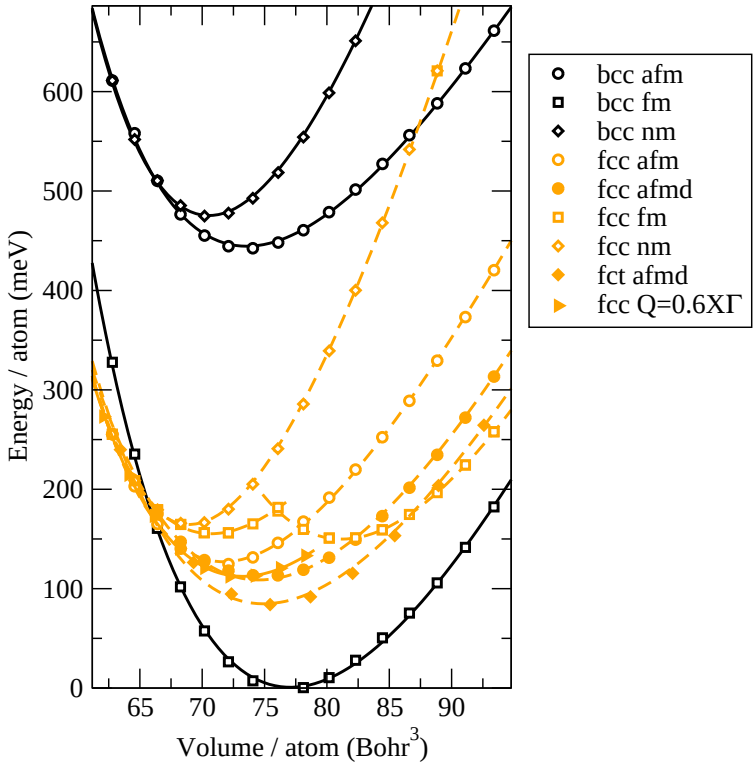

Figure 3.19: The total energy ground-state phase diagram of Fe in the fcc as well as the bcc structure for various magnetic phases. The energy difference between the different magnetic configurations is much larger in bcc than in fcc Fe indicating a smaller magnetic exchange in the latter, see text for details.

We included in the ground-state search the tetragonal distorted fct structure. Allowing in addition relaxations (internal coordinates as well as cell shape) in the total energy calculations, the afmd fct structure (breaking the axial symmetry) shown in Fig. 3.19 is pronounced as the lowest magnetic phase resulting in $c/a \approx 1.09$.

To illustrate that in the *ideal* fcc structure the Q_2 state provides the lowest spin spiral structure of all possible $\boldsymbol{q}$-spirals, we show in Fig. 3.20 (b) the computed spin spiral spectra at two volumes $V = 10.61$ Å^3 and $V = 11.19$ Å^3. As mentioned above, a second local minimum occurs at $Q_1 = 2\pi/a(0.2, 0, 1)$ close to the experimental as well as previous theoretical findings [19]. Comparing the spin spiral spectra for fcc Fe (Fig. 3.20 (b)) with the previously obtained spectra for bcc Fe (Fig. 3.20 (a)) we directly observe that the effective magnetic exchange coefficients $\tilde{J}_{\boldsymbol{q}}$ are indeed about one order of magnitude smaller in the fcc than in the bcc phase. This is consistent with the various magnetic phases in Fig. 3.19 being close in energy. Also the Γ-point (ferromagnetic phase) represents no longer the energetic minimum, which reflects the fact that the system is magnetically unstable in the ferromagnetic phase. At both considered volumes the spin spiral with the wave vector Q_2 represents the magnetically most stable configuration.

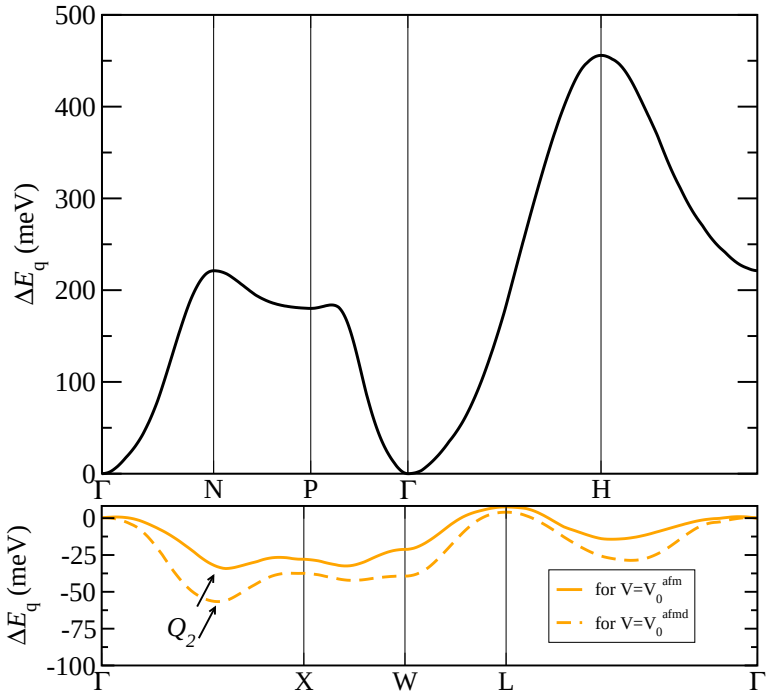

Figure 3.20: Total energy of different spin spirals $\boldsymbol{q}$ as given by Eq. (2.61). Above: bcc Fe for $V = 11.21\text{Å}^3$. Below: fcc Fe for two different volumes $V_0^{\text{fcc,afm}} = 10.61\text{Å}^3$ and $V_0^{\text{fcc,afmd}} = 11.19\text{Å}^3$, see text for details.

Analytic Approximations

We start the investigation of the magnetic entropy and the magnetic critical temperature of fcc Fe by considering analytic approaches, i.e., the RPA and the MF solution. In the context of the RPA, the main difficulty for a system showing a non-collinear spin spiral ground state arises from the fact that there is no *global* quantization axis available anymore (see Fig. 3.21). A common approach for analytic approaches in such a case is to express the Hamiltonian in a *locally rotated* coordinate system which allows eventually again to work with *one* global quantization axis. As proposed in Ref. [140], we rotate the local coordinate system Σ_i of each spin $\boldsymbol{S}_i$ into a new one $\Sigma_i^{'}$ parallel to the z-axis. The spins in the unrotated system Σ_i can be expressed in the rotated coordinates via

$$\begin{pmatrix} S_{ix} \\ S_{iy} \\ S_{iz} \end{pmatrix} = \begin{pmatrix} \cos(\boldsymbol{Q}\boldsymbol{R}_i)S'_{ix} + \sin(\boldsymbol{Q}\boldsymbol{R}_i)S'_{iz} \\ S'_{iy} \\ -\sin(\boldsymbol{Q}\boldsymbol{R}_i)S'_{ix} + \cos(\boldsymbol{Q}\boldsymbol{R}_i)S'_{iz} \end{pmatrix}, \tag{3.28}$$

where S'_{ik} is the k-component of the spin $\boldsymbol{S}'_i$ at lattice site i in the rotated system and $\boldsymbol{R}_i$ is the lattice vector. We remark that such a general solution naturally includes the ferromagnetic solution $Q = (0, 0, 0)$ which we already applied in Sec. 3.2.1. The Heisenberg Hamiltonian (2.83) in this

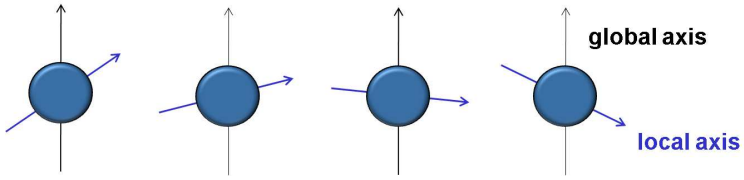

Figure 3.21: Sketch of non-collinear spin spiral state.

(locally rotated) coordinates reads as [140]

$$\mathcal{H}' = -\sum_{ij}\left(K_{ij}S'_{ix}S'_{jx} + L_{ij}S'_{iy}S'_{jy} + M_{ij}S'_{iz}S'_{jz}\right) + 2\sum_{ij} N_{ij}S'_{ix}S'_{jz}, \tag{3.29}$$

with anisotropic exchange constants

$$K_{ij} = M_{ij} = J_{ij}\cos\left[Q(R_i - R_j)\right], \tag{3.30}$$
$$N_{ij} = J_{ij}\sin\left[Q(R_i - R_j)\right], \tag{3.31}$$
$$L_{ij} = J_{ij}. \tag{3.32}$$

Analogously to the case of the ferromagnet, the free energy F^{mag} we are interested in can be obtained by deriving the internal energy U and integrating it afterwards, see Eq. (2.82).

The key idea is exactly the same as for the ferromagnet, i.e., to rescale a $S = 1/2$ RPA solution. For the sake of clarity we will discuss the main results for the non-collinear RPA solution. The intermediate steps are discussed in the appendix in detail. We proceed in a similar way as in Sec. 3.2.1:

In the first step we derive a rescaling factor γ which allows to rescale the RPA internal energy solution for $S = 1/2$ into a general spin solution. For this purpose we consider first the expression for the critical temperature T_N of a non-collinear magnet for $S = 1/2$ as well as $S \geq 1/2$ and obtain (see Sec. A.3.1 for a detailed derivation):

$$S \geq 1/2 \qquad k_B T_N = \frac{4}{3}S(S+1)\left(\sum_{\boldsymbol{q}}\left[\frac{1}{K_{\mathbf{o}} - K_{\boldsymbol{q}}} + \frac{1}{K_{\mathbf{o}} - J_{\boldsymbol{q}}}\right]\right)^{-1}, \tag{3.33}$$

$$S = 1/2 \qquad k_B T_N = 2S\left(\sum_{\boldsymbol{q}}\left[\frac{1}{K_{\mathbf{o}} - K_{\boldsymbol{q}}} + \frac{1}{K_{\mathbf{o}} - J_{\boldsymbol{q}}}\right]\right)^{-1}. \tag{3.34}$$

Comparing the solutions of T_N, the rescaling factor γ for the normalized exchange coefficients $\tilde{J}$ is deduced as

$$S(S+1)J \equiv \tilde{J} \Rightarrow SJ =: \gamma\tilde{J}, \tag{3.35}$$

with $\gamma = 1/(S+1) = 2/3$ for $S = 1/2$. We want to point out that the known expression for the critical temperature above in terms of commonly employed effective exchange coefficients $\tilde{J}$,

$$k_B T_{\text{Néel}}^{\text{RPA}} = \frac{4}{3}\left(\sum_{\boldsymbol{q}}\left[\frac{1}{\tilde{K}_{\mathbf{o}} - \tilde{K}_{\boldsymbol{q}}} + \frac{1}{\tilde{K}_{\mathbf{o}} - \tilde{J}_{\boldsymbol{q}}}\right]\right)^{-1}, \tag{3.36}$$

has already been derived and successfully applied to europium [140, 141] and is consistent with the conventional solution Eq. (2.101) of the ferromagnet ($Q = (0,0,0)$, i.e., $\tilde{K}_{\boldsymbol{q}} \equiv \tilde{J}_{\boldsymbol{q}}$), which we employed to investigate the pressure dependence of $T_C(p)$ in the bcc phase in Sec. 3.1. The major task for the next step is to derive a $S = 1/2$ expression for the internal energy and replace all SJ by $\gamma\tilde{J}$.

To compute the magnetic entropy, we need in the second step an expression for the RPA internal energy for $S = 1/2$ within the rotated coordinate system (3.29), which could be afterwards combined with Eq. (3.35). We want to stress that such a theory is not available in the literature. In principle our derivation is similar to the one for the ferromagnet, but involves a more lengthy derivation due to the rotated coordinate system. For the sake of readability we present here the final results only and provide the full derivation in the appendix A.3.2. For the internal energy U we obtain

$$U^{\text{RPA}}(T) = U_0 + \frac{M}{2} m(T) \sum_{\boldsymbol{q}} \left(A_{\boldsymbol{q}}^{+} + A_{\boldsymbol{q}}^{-} + B_{\boldsymbol{q}}^{+} + B_{\boldsymbol{q}}^{-}\right), \tag{3.37}$$

where $A_{\boldsymbol{q}}^{\pm}$ and $B_{\boldsymbol{q}}^{\pm}$ are given by

$$A_{\boldsymbol{q}}^{\pm} = \chi_{\boldsymbol{q}\pm} \frac{\pm\omega_{\boldsymbol{q}} + 2\gamma(\tilde{K}_{\mathbf{o}} - \tilde{J}_{\boldsymbol{q}})}{\exp(\pm\beta\omega_{\boldsymbol{q}} - 1)}, \tag{3.38}$$

$$B_{\boldsymbol{q}}^{\pm} = \pm \frac{2\gamma m(T)(\pm\omega_{\boldsymbol{q}} - 2\gamma\tilde{J}_{\boldsymbol{q}})(\tilde{K}_{\mathbf{o}} - \tilde{J}_{\boldsymbol{q}})}{4E_{\boldsymbol{q}} \exp(\pm\beta\omega_{\boldsymbol{q}} - 1)}, \tag{3.39}$$

and with anisotropic exchange coefficients

$$\tilde{K}_{\boldsymbol{q}} = 1/2(\tilde{J}_{\boldsymbol{Q}+\boldsymbol{q}} + \tilde{J}_{\boldsymbol{Q}-\boldsymbol{q}}). \tag{3.40}$$

Here, the reduced magnetization is given by

$$m_{\text{RPA}}^{S=1/2}(T) = \frac{1}{1+2\varphi}, \tag{3.41}$$

with the effective magnon occupation

$$\varphi(T) = \frac{1}{N}\sum_{\boldsymbol{q}}\left(\frac{\chi_{\boldsymbol{q}+}}{e^{\beta\omega_{\boldsymbol{q}}} - 1} + \frac{\chi_{\boldsymbol{q}-}}{e^{-\beta\omega_{\boldsymbol{q}}} - 1}\right). \tag{3.42}$$

The effective magnon excitation energies are given by

$$\omega_{\boldsymbol{q}} = 2\gamma m_{\text{RPA}}^{S=1/2} \sqrt{\left(\tilde{K}_{\mathbf{o}} - \tilde{K}_{\boldsymbol{q}}\right)\left(\tilde{K}_{\mathbf{o}} - \tilde{J}_{\boldsymbol{q}}\right)} \tag{3.43}$$

and

$$\chi_{\boldsymbol{q}\pm} = \frac{1}{2}\left(1 \pm \frac{a_{\boldsymbol{q}}}{\omega_{\boldsymbol{q}}}\right) \tag{3.44}$$

represent the weights for magnon creation ("+") and annihilation ("-") respectively with

$$a_{\boldsymbol{q}} \;=\; 2\gamma m(T)(\tilde{K}_{\mathbf{o}} - 1/2(\tilde{K}_{\boldsymbol{q}} + \tilde{J}_{\boldsymbol{q}})). \tag{3.45}$$

Eqs. (3.37)-(3.45) form a closed system of equations which can be solved self-consistently. It represents the generalization of the theory proposed in Sec. 3.2.1 and is equivalent to the latter for $Q = (0, 0, 0)$ (ferromagnetic ground state).

For comparison we also employ a known MF theory for non-collinear spin systems, where the internal energy is given as [31]

$$U^{\mathrm{MF}}(T) = M_0\langle S_z'\rangle^2 = \frac{S}{S+1}\tilde{M}_0 m^2_{\mathrm{MF}}(T) = \frac{S}{S+1}\tilde{J}_Q m^2_{\mathrm{MF}}(T). \tag{3.46}$$

The reduced magnetization $m_{\mathrm{MF}}(T)$ can be determined in full analogy to (2.87), resulting in a Brillouin function which is characterized by the MF critical temperature

$$k_B T'^{\mathrm{MF}}_{\mathrm{Néel}} = \frac{2}{3}\tilde{J}_Q. \tag{3.47}$$

The Néel Temperature of Fcc Iron

Before discussing the different entropy contributions (vibronic, electronic, and magnetic) we consider first the Néel temperature by employing the derived expressions within MF and RPA, Eq. (3.47) and (3.36). Similar to fm bcc Fe, we employ the effective exchange coefficients $\tilde{J}$ obtained at the ground-state volume. As discussed above, there are many, nearly degenerate, energetically metastable magnetic phases. We consider, therefore, in the following two representative structures, i.e., the afm and the afmd case and perform the spin spiral calculations at the corresponding ground-state volumes, which are $V_0^{\mathrm{afm}} = 10.61$ Å^3 and $V_0^{\mathrm{afmd}} = 11.19$ Å^3. Within MF, $T^{\mathrm{MF}}_{\mathrm{Néel}}$ is only determined by the lowest spin spiral energy, Eq. (3.47), and we obtain $T^{\mathrm{MF,afm}}_{\mathrm{Néel}} = 183$ K and $T^{\mathrm{MF,afmd}}_{\mathrm{Néel}} = 235$ K. We recall that an experimental measurement of $T_{\mathrm{Néel}}$ for pure bulk fcc iron is not possible because it is not stable at low temperatures. Fcc iron is often stabilized by alloying it with manganese (Mn). For this reason, we compare in Fig. 3.22 the MF results with the phenomenological CALPHAD prediction as well as experimental data for fcc Fe-Mn alloys and different Mn-concentrations. Consistent with our findings for ferromagnetic (fm) bcc iron, the MF approximation provides an upper limit for $T_{\mathrm{Néel}}$ being slightly above the CALPHAD estimation.

The RPA approximation provided a very reasonable estimation of T_C for the ferromagnetic systems. Employing (3.36), we obtain $T^{\mathrm{RPA}}_{\mathrm{Néel}} = 141$ K/199 K for the exchange coefficients extracted at the ground-state volumes of the afm and afmd phase, respectively. Due to the weaker $\tilde{J}_{ij}$ in fcc iron compared to the bcc phase, both approximations (MF/RPA) provide very similar predictions. The much lower critical temperature in the austenite compared to the ferrite is a direct consequence of the much flatter spin spiral dispersion in Fig. 3.20. The results for $T^{\mathrm{RPA}}_{\mathrm{Néel}}$ are smaller than the corresponding MF values and also closer to the CALPHAD prediction, see Fig. 3.22. Apart from the analytic methods, the classical Monte Carlo approach provided for bcc iron also a very

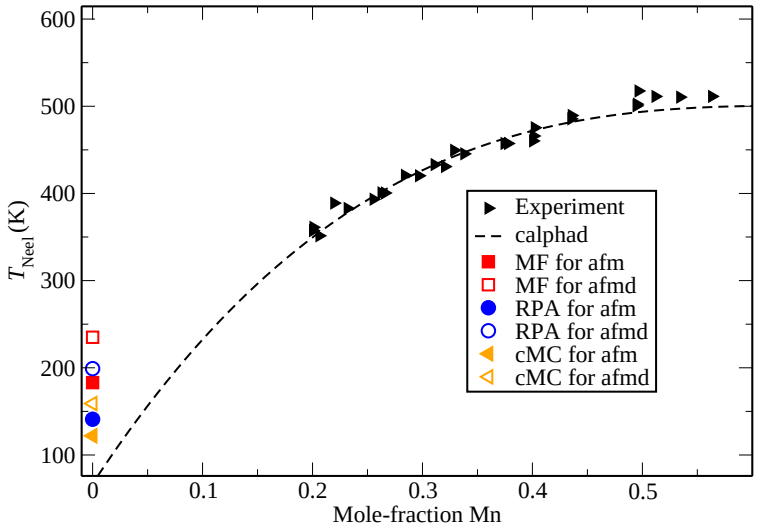

Figure 3.22: Computed Néel temperature in fcc iron in comparison with experimental data [142] for different Mn-concentrations. The empirical CALPHAD estimation [142] is shown for comparison.

reasonable estimation of the critical temperature. As a crosscheck, cMC calculations were also carried out for fcc[20] based on the computed exchange coefficients in real space (obtained by a Fourier transformation). The critical temperatures we obtain are, as in the bcc case, similar to the ones obtained using the analytic RPA approach. Explicitly, we obtain $T_{\text{Néel}}^{\text{cMC}} = 122$ K/159 K for the afm/afmd phase. To estimate the theoretical uncertainty on the $T_{\text{Néel}}$ prediction we average over the three approximations and the two magnetic structures and obtain

$$T_{\text{Néel}}^{\gamma,\text{theo}} \approx 173 \ \pm 41 \text{ K}, \tag{3.48}$$

where 41 K denotes the standard deviation.

The Helmholtz Free Energy of Fcc Iron

After achieving a reliable description of the magnetic phase transition temperature we pass over to the Helmholtz free energy, Eq. (3.4). For this purpose we identify first the afmd tetragonal distorted fct structure as the energetically lowest collinear magnetic phase from the the total energy calculations in Fig. 3.19. To estimate the uncertainty due to the chosen magnetic ground-state configuration, we performed (similarly to the determination of the critical temperature) each of the steps for the afm phase as a crosscheck as well.

To derive the vibronic contribution to the total free energy within the quasiharmonic approximation (Sec. 2.2.4), phonon calculations were carried out at different volumes for both magnetic phases (afm/afmd). Since there are different atom types in the unit cell (spin-up and spin-down), optical branches appear in addition to the acoustic ones.[21] We show in Fig. 3.23 the phonon density

[20] The cMC calculations involve 4×10^6 steps including thermalization and thermal averaging. The calculations are performed for a system containing $N = 1728$ spins and taking into account up to 25 interaction shells.

[21] For the afm structure, a small part of the phonons were imaginary (less than 3%), ruling out the direct use of the

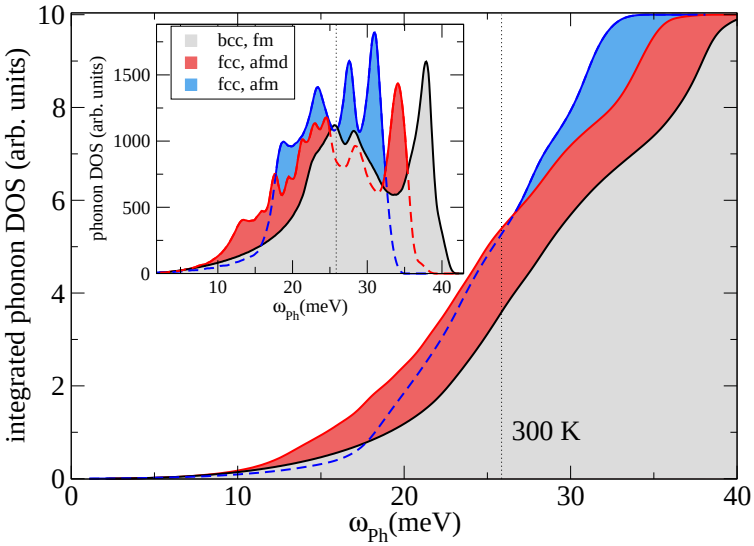

Figure 3.23: Phonon DOS of fcc iron deduced from the antiferromagnetic single- (red shaded areas) as well as double-layer phase (blue shaded area). The DOS of the fm bcc phase is shown for comparison. The vertical dotted line corresponds to the thermal energy at room temperature (300 K $k_B \approx 25$ meV).

of states (DOS) deduced from the fcc afm and afmd phases (inset) as well as the integrated phonon DOS. We directly observe that the DOS of the afm phase are shifted to lower energies compared to the afmd phase indicating a higher vibronic contribution. In order to quantify the impact of the chosen magnetic phase (afm or afmd) on the vibronic free energy contribution, we compare in Fig. 3.24 the results of the qh approximation with CALPHAD data. Within the qh approximation the impact of the chosen magnetic phase (solid and dashed green line) is in the order of 10 meV. This indicates the robustness of the approach with respect to the chosen magnetic ground-state configuration. Regarding the absolute agreement strong deviations ($\sim$ 150 meV at 1800 K) between the vibrational analysis and the empirical CALPHAD data are found. Based on our previous investigations for bcc Fe, a considerable amount of entropy stems from the electronic degree of freedom which has to be taken into account for free energy considerations.

After calculating the electronic contribution, we also compare the free energy of both (phonon + electronic) contributions in Fig. 3.24 with the CALPHAD data. It is worth mentioning that with respect to the starting configuration (afm or afmd) the difference of the total free energy between the two considered phases is less than 30 meV at 1800 K which corresponds to a relative deviation of less than 3%. However, in contrast to the bcc phase, the missing magnetic contribution to the total free energy compared to the CALPHAD data is already visible at relatively low temperatures. This is consistent with the computed Néel temperature, Eq. (3.48), being in the order of the room temperature.

To compute the magnetic contribution to the free energy we apply the derived expressions for the

qh approximation (negative argument of logarithm in Eq. (2.116)), and indicating that the afm structure is unstable for certain distortions. Since only a small part of the computed phonon frequencies are affected, we apply a common first order approximation and ignore such phonon modes for the evaluation of the vibronic free energy.

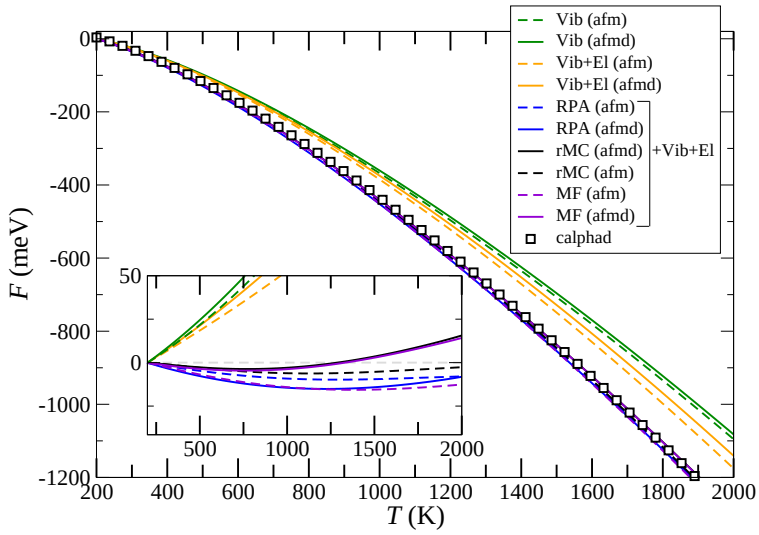

Figure 3.24: Free energy of fcc iron vs. CALPHAD data for different treatments of the magnetic contribution. Inset: The CALPHAD data is taken as the reference at each temperature.

MF and RPA, Eqs. (3.47) and (3.36), and employ in addition the developed rMC ansatz (Sec. 3.2.2) based on the cMC data (which has been employed to derive $T_{\text{Néel}}^{\text{cMC}}$). For the latter, the spin quantum numbers derived from the ground-state moments $M_0^{\text{fcc,afm}} = 1.39\mu_B$ and $M_0^{\text{fcc,afmd}} = 1.67\mu_B$ are used for the rescaling function $f(S,t)$ provided in Eq. (3.25). The computed total free energies including the magnetic contributions are also shown in Fig. 3.24. For both considered phases the free energy significantly improves with respect to the experimental data. It is interesting to note that, in contrast to bcc iron, even the MF approximation allows an excellent estimation of the magnetic entropy contribution. This is related to the much lower critical temperature of fcc compared to bcc iron and the fact, that MF reproduces the high temperature limit of fully disordered spins.

We can conclude that the developed methodologies allow a promising (even quantitative) prediction of the full Helmholtz free energy of γ-iron. Starting the analysis from two representatives (afm and afmd phase), the total computed free energies provide a confidence interval for the true experimental energy with an energy window of about $\sim$ 20 meV per atom. Starting from other (magnetic) phases (e.g. paramagnetic phase) should therefore not change the obtained results crucially. We proceed in the next section with the discussion of the relative difference between the bcc and the fcc phase and the discussion about the different impact of vibronic, magnetic, and electronic contributions on the phase stability of these phases, respectively.

3.3.2 Impact of Vibronic, Electronic, and Magnetic Contributions on the Structural Phase Transition in Iron

In thermodynamic equilibrium the phase transitions between bcc and fcc correspond to a double crossing of the underlying Helmholtz free energies of Fe, i.e., of the bcc phase, $F_{\text{bcc}}(T)$, and the fcc phase, $F_{\text{fcc}}(T)$. Defining the free energy difference $\Delta F^{\text{tot}} = F_{\text{bcc}} - F_{\text{fcc}}$, a positive value $\Delta F^{\text{tot}} > 0$ corresponds to a stabilization of the fcc phase whereas a negative value $\Delta F^{\text{tot}} < 0$ indicates a stable

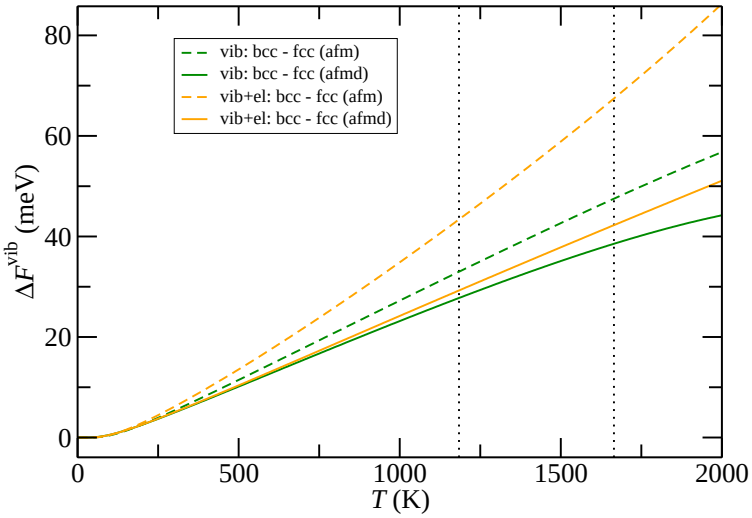

Figure 3.25: Impact of electronic and vibronic contributions on the stabilization of the bcc and fcc phase of iron. The dotted lines denote the experimental observed transition temperatures between the bcc and fcc structure.

bcc structure. We show in Figs. 3.18 the free energy difference ΔF^{tot} obtained by the CALPHAD method [119]. It provides very important information for our further analysis: the observed difference clearly shows that the theoretical accuracy needed to reproduce the experimental findings is in the order of ~ 1 meV for temperatures up to 2000 K.

Regarding the thermodynamic methods to capture the magnetic entropy contributions we have developed so far, a *numerical* accuracy of ~ 1 meV is indeed feasible (accompanied with extremely accurate and expensive calculations though). With the term "*numerical* accuracy" we specifically denote all errors which can be controlled ensuring sufficiently high convergence parameters, for instance for the DFT calculations the chosen k-point grid, cutoff energy or supercell, or for the Monte Carlo simulations the total number of measurement steps, number of included interaction shells and chosen supercell. All these parameters can be chosen such that the required convergence criterion (~ 1 meV) is fulfilled.

We denote the remaining source of uncertainty as *methodological* errors which can not be decreased by choosing "better" convergence parameters. Regarding the treatment of the magnetic entropy, this includes the error due to the simplification of the magnetic system (mapping onto an effective Heisenberg Hamiltonian) as well as the necessary approximations to solve the model (rMC, MF or RPA). In addition, on the DFT level, the potential error due to the approximative treatment of the xc-functional. For bcc and fcc iron we found empirically that the methodological errors are at the considered high temperatures in the order of $\sim 10 - 20$ meV. Regarding the DFT input, similar methodological limits are found for the quasiharmonic and electronic entropy considerations (see e.g. [5, 80]). We, therefore, do not aim at a quantitative agreement with the CALPHAD data in the following but rather concentrate on balance and impact of the different entropy contributions which is still a open question in the literature.

Different authors [120, 122, 143] suggested that the vibronic contribution of the fcc phase has an important impact on the stabilization of the fcc phase and hence on the bcc-fcc transition (at

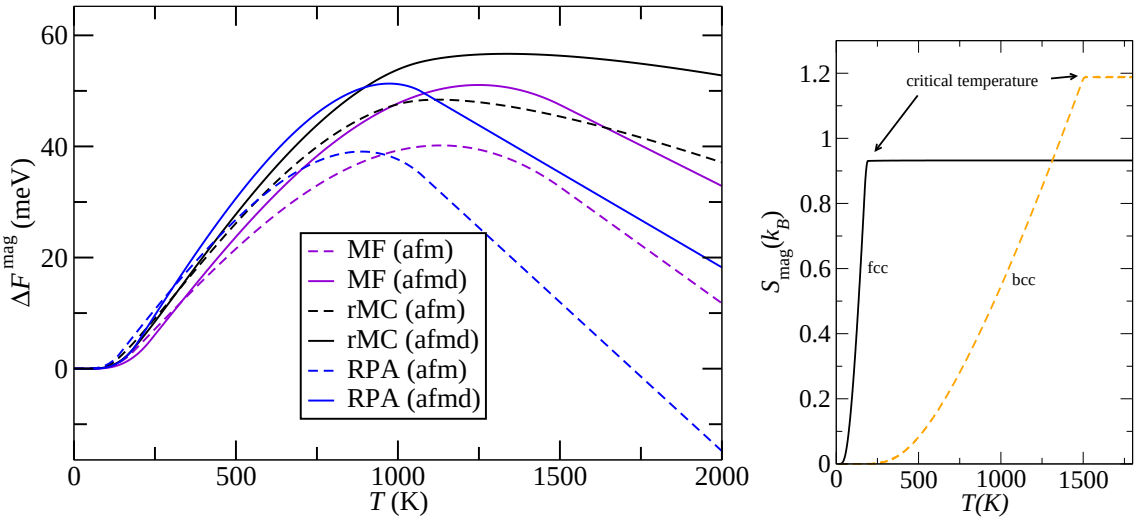

Figure 3.26: Left side: Impact of magnetism on the stabilization of the bcc and fcc phase of iron for different treatments of the magnetic contribution. Right side: Magnetic entropy obtained within MF for the fcc afm and the bcc phase.

1200 K). On the other hand, as mentioned above, from purely geometric arguments, the atoms in the more open bcc structure should have more space to vibrate and hence it should be easier to excite phonons. However, as shown in Fig. 3.23, the bcc phonon DOS is in fact altogether higher in energy than the DOS of the fcc phase. This finding is consistent with recent fixed spin moment phonon calculations for bcc iron [124]. It is shown that the magnetic moment of bcc iron has an considerable impact on the phonon spectra. As a consequence, the computed phonon modes for bcc iron decrease in energy with decreasing moment [124]. Since the bcc phase has a higher magnetic moment than the fcc phase, one can conclude that the smaller vibronic contribution to the total free energy of the bcc phase can be attributed to its larger magnetic moments.

In order to elucidate its quantitative impact on the phase transition, we show in Fig. 3.25 the difference of the vibronic contribution $\Delta F^{\mathrm{vib}} = F^{\mathrm{bcc}}_{\mathrm{vib}} - F^{\mathrm{fcc}}_{\mathrm{vib}}$. For both considered magnetic phases of the fcc structure, the vibronic contribution is indeed larger than for the bcc phase, i.e., it stabilize the fcc phase. This is consistent with the obtained phonon densities shown in Fig. 3.23 and strengthens again the fact that a geometric argumentation is not sufficient in case of magnetic systems. The impact of the electronic contribution on the phase transition is similar as found for the vibronic one, stabilizing the fcc phase with increasing temperature (also shown in Fig. 3.25). Considering the impact of both contributions on the phase stability leads us to a very important conclusion: Vibronic and electronic contributions definitely drive the transition bcc→fcc, but neither the vibronic nor the electronic contribution can explain the observed second transition (fcc → bcc). This clearly shows the importance of magnetic contributions which have to be taken into account.

To clarify their role, we show in Fig. 3.26 the difference of the magnetic contribution of the bcc and fcc phase, $\Delta F^{\mathrm{mag}} = F^{\mathrm{bcc}}_{\mathrm{mag}} - F^{\mathrm{fcc}}_{\mathrm{mag}}$. All theoretical treatments show qualitatively the same behavior, i.e., both transitions could be explained on qualitative level *solely* by taking into account the magnetic contributions, which is in agreement with the results of Ref. [8]. The qualitative behavior

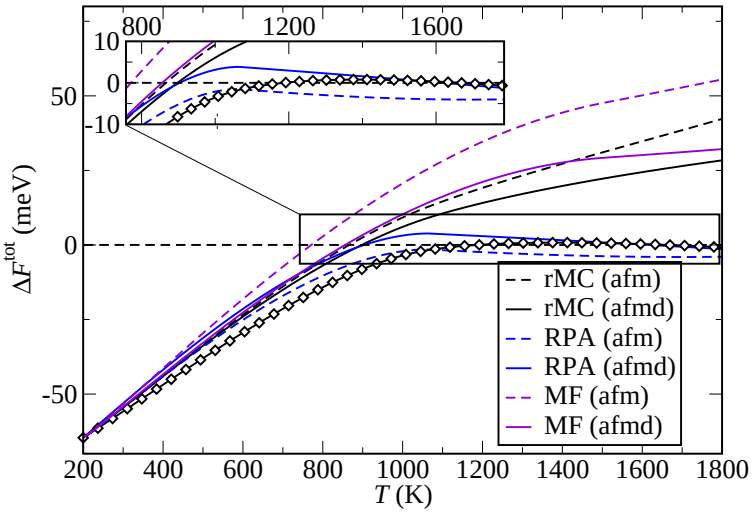

Figure 3.27: Difference of the Helmholtz free energies of the fcc and the bcc phase of pure iron in comparison with CALPHAD data (shown as black diamonds) [119]. The theoretical results are aligned to the CALPHAD data at 200 K.

can be understood as follows: In general, the magnetic entropy of both phases increases rapidly when approaching the critical temperature (maximum entropy for full disorder). However, since the critical temperature of the fcc phase is much lower than that of the bcc phase ($T_{\text{Néel}} \ll T_{\text{Curie}}$), the contribution of the fcc phase dominates the difference up to $\approx T_C$. At these high temperatures the fcc phase already reached its maximum entropy while in the bcc phase a substantial amount of magnetic entropy is still conserved in the magnetic order (shown in Fig. 3.26 for the MF result). At very high temperatures, however, the bcc phase finally overcomes the magnetic contribution of the fcc phase due to the higher magnetic moment, i.e., higher maximum entropy. Therefore, the magnetic contributions tend to stabilize the fcc phase at low temperatures (due to the lower critical temperature) and hence support (in combination with the vibronic contribution) the first phase transition (bcc→fcc). For higher temperatures the stronger local magnetic moments of the bcc phase are responsible for the, in the end, higher magnetic contribution as well as the weaker vibronic contribution of the bcc phase, both being responsible for the second phase transition (fcc→bcc). We note that the *quantitative* impact of these effects differs for the different theoretical approaches (MF, RPA and rMC), since the latter provide slightly different magnetic entropy contributions.

We finally compare in Fig. 3.27 the absolute free energy differences with the CALPHAD data. Since errors in the theoretical prediction accumulate with increasing temperature, the spread between different methods increases at high temperatures. Overall, the theoretical calculations are in fair agreement with experiment and correctly describe the first transition from the bcc to the fcc phase (apart from the fcc RPA afm result). However, regarding the second transition, a final conclusion whether the transition back to the bcc phase takes place or not, is - solely based on the theoretical predictions - not possible. In fact, the error bar provided by the different methods allows either a transition back to the bcc phase as well as a stabilization of the fcc phase within an energy window consistent with the methodological accuracy limits of the employed schemes.

Conclusion

The scatter between the results of the different theoretical treatments for the magnetic entropy contribution of fcc Fe is much smaller compared to bcc Fe. The reason is that the critical temperature and effective spin moment of iron in the fcc lattice is much lower than in the bcc lattice. As a consequence, a mean field treatment already provided a reasonable description of the magnetic free energy of the austenite above room temperature.

Regarding the impact of magnetism on the structural transitions, the two most important factors are (again) the effective spin quantum number (determining the high temperature entropy limit) as well as the critical temperature. Both quantities were sufficient to understand *qualitatively* the phase transitions in iron.

3.4 Nearest-Neighbor Approach: Application to Fe, Co, and Ni

In the beginning of Chapter 3 we discussed two possibilities for solving the Heisenberg model for realistic systems namely (a) approximative solutions for a full (long-ranged) Hamiltonian and (b) an exact solution of an effective (simplified) one. In the previous sections we developed and applied different approaches for (a). In doing so we learned that, apart from the crystal structure and the spin quantum number, also the critical temperature critically affects many aspects of the underlying magnetic model Hamiltonian. In addition, we observed a universal behavior of the thermodynamic properties of the Heisenberg model in Sec. 3.2.2, if the critical temperature is kept fixed. In the following we employ this insight to propose an appropriate ansatz (b), which is more convenient than solving the *full* Hamiltonian and provides a similar accuracy. For this purpose we introduce an auxiliary, effective nearest-neighbor Hamiltonian. The model is characterized by a nearest-neighbor exchange parameter J, as well as the crystal structure and spin S of the system, and can be solved numerically exact by QMC. The previously discussed negative sign problem does not apply here, since magnetic frustration does not occur for a nearest-neighbor ferromagnet. The effective J parameter is constructed such that it contains the long-ranged interactions[22] J_{ij} in a mean field manner. Our previous investigations in Sec. 3.2.2 have revealed that the critical temperature T_C is the decisive quantity in this context and it needs to be ensured that it does not alter during the mapping. Such an approach has the big advantage of decoupling the evaluation of T_C (for which the approximative methods such as RPA and the cMC work very well) from the computation of the other thermodynamic properties, see Fig. 3.28.

If the critical temperatures are provided, such an approach is computational much less expensive (due to the reduction to just one J-parameter) compared to a full cMC simulation (including long-ranged exchange parameters). To test the transferability of the approach we include in the following all 3d ferromagnets, namely Fe, Co, and Ni. Finally, the computed magnetic contribution is combined with *ab initio* derived vibronic, and electronic contributions to access the full free energy and heat capacities. To account for the full free energy we employ the adiabatic approximation and separate the electronic, vibronic and magnetic contributions as in the previous sections. As for bcc iron, electronic and vibronic contributions have been determined using the quasiharmonic approximation and finite temperature DFT respectively, as in [6, 16, 58]. All QMC calculations are done employing the direct-loop algorithm in the stochastic series expansion as implemented in the ALPS code [72]. Monte Carlo calculations involve 2.5×10^6 steps including thermalization and statistical averaging.

The theoretical ground-state magnetic moments[23] M_0 are used to define the spin quantum number $\tilde{S} = M_0/(g\mu_B)$ where $g \approx 2$ denotes the Landé factor, see Eq. (3.7). We note that in systems containing itinerant electrons the value of M_0 and hence of $\tilde{S}$ is not restricted to those of the (ideally localized) quantum spin model ($S = 1/2, 1, 3/2, \cdots$), i.e., $\tilde{S}$ could be any real number $\tilde{S} \in \Re$. In practice we compute the exact solutions for both neighboring spin numbers of a given $\tilde{S}$,

[22] Since by construction the exchange interactions are reduced using a single parameter (i.e. T_C), the extension to multi-magnetic alloys (systems containing different magnetic species in the unit cell and hence several effective parameters) is not straightforward.

[23] The computed ground-state moments are: 2.21 μ_B (Fe), 1.64 μ_B (Co), and 0.63 μ_B (Ni).

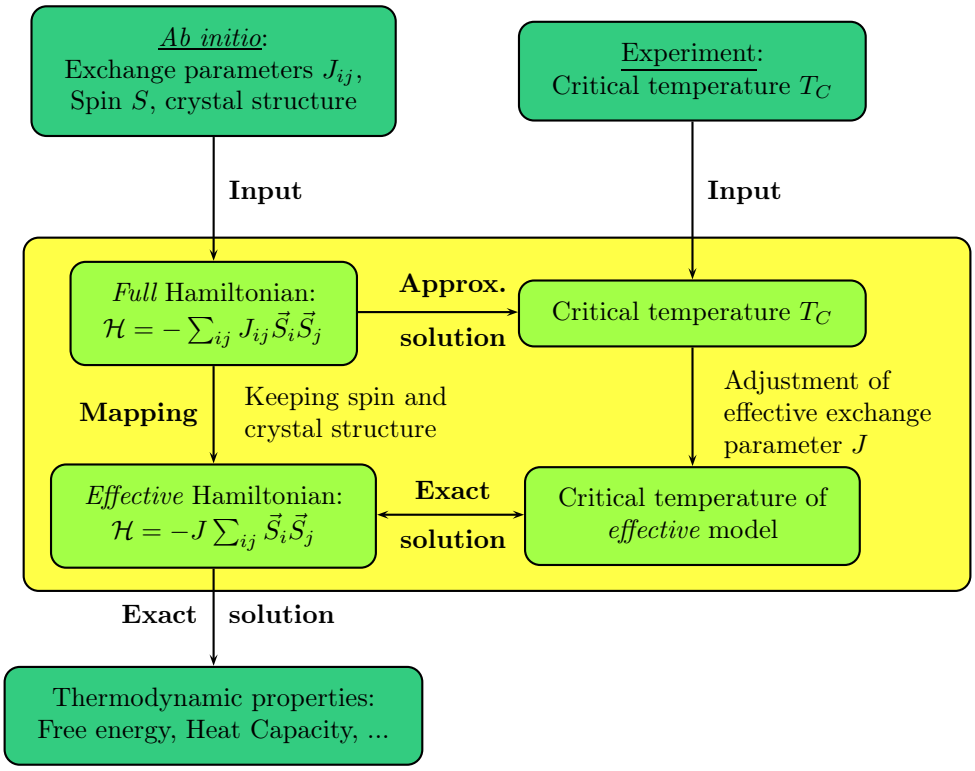

Figure 3.28: Sketch of the effective nearest-neighbor approach. The DFT data is used as input for the full Hamiltonian which is solved approximately to obtain T_C. Alternatively, the critical temperature can be taken from experiment. The effective nearest-neighbor exchange parameter J is chosen as such that it reproduces the provided T_C. Based on this, the effective Hamiltonian is solved exactly providing the thermodynamic properties.

$S_1 \leq \tilde{S} \leq S_2$ ($S_2 - S_1 = 1/2$). The physical quantities $\tilde{f}(T, \tilde{S})$ (e.g. heat capacity or magnetization) are computed employing a linear interpolation afterwards, i.e.,

$$\tilde{f}(T, \tilde{S}) = \alpha f(T, S_2) + (1 - \alpha) f(T, S_1), \tag{3.49}$$

with $\alpha = 2(\tilde{S} - S_1)$. In practice we performed calculations for $S = 1$ and $S = 3/2$ for bcc Fe, and for $S = 1/2$ and $S = 1$ for fcc Co and fcc Ni. For the latter a linear extrapolation instead of an interpolation is used in order to estimate the solution for $\tilde{S} = 0.3$.

Apart from $\tilde{S}$ the remaining input parameters for Eq. (2.83) are the crystal structure and the critical temperature T_C. As explained above, the latter is used to determine the *effective* nearest-neighbor exchange coupling J. T_C could be taken either from a theoretical estimation [15, 48] or from experiment. Here, the experimental[24] T_C is chosen ($T_C^{\text{exp}} \rightarrow J$). In practice, we first perform the model calculations for an arbitrary J^{start} parameter. The results of the specific heat capacity C_P are subsequently fitted to the given T_C by the position of the peak in C_P.

We start the discussion by investigating C_P. Its computed temperature dependence is shown in Fig. 3.29 in comparison with experimental data obtained under ambient pressure. We first focus on

[24] We use the experimental values: 1044 K (Fe), 1388 K (Co), and 631 K (Ni).

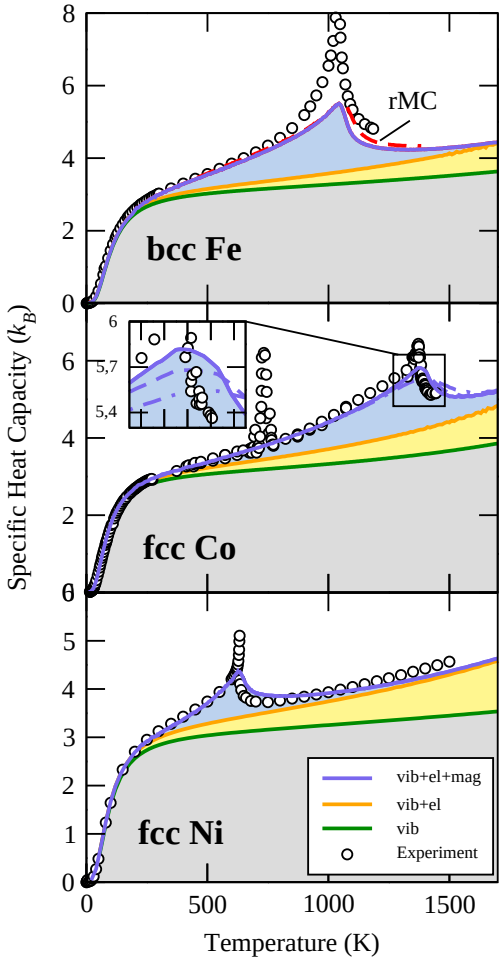

Figure 3.29: The specific heat capacity $C_P(T)$ *vs.* temperature in comparison with experimental data [107, 144–146]. The magnetic contribution is computed in a QMC calculation for $N = 5832$ spins.

the sum of the vibronic and electronic contributions (orange line). The fact that this sum reproduces the experimental heat capacities very well up to ≈ 300 K nicely indicates that the systems are still close to the magnetic saturation in this temperature regime. However, above room temperature the importance of the magnetic contribution is clearly visible for all three magnets in agreement with our previous findings for bcc iron. Please note that the first peak in the case of Co at ≈ 700 K occurs due to the hcp-fcc transition, which is not accounted for in the present approach (since both phases are very similar [147] and the fcc phase is the dominant one at T_C, we only consider fcc Co here). It is worth mentioning that the electronic contribution increases from Fe to Co and is highest for Ni. This is inherently related to the smallest band splitting in case of Ni ($\sim 0.2 - 0.3$ eV), which is in the order of the thermal energy at the considered temperatures. In this case, electrons of both 3d sub-bands (spin-up and spin-down) can be thermally activated and contribute to the total electronic entropy.

Within the QMC calculations the magnetic contribution to the heat capacity is directly com-

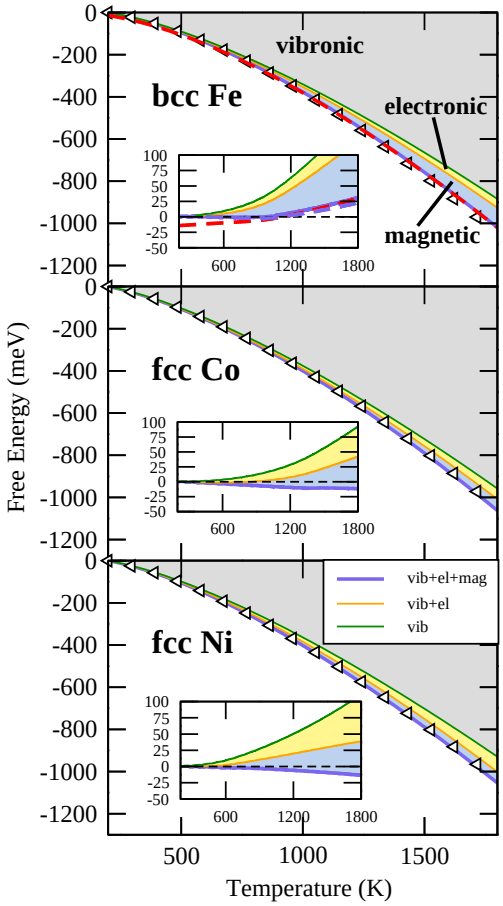

Figure 3.30: The free energy $F(T)$ *vs.* temperature T (solid line) in comparison with CALPHAD data (symbols). The electronic and magnetic contributions are indicated by orange and blue shading, respectively. The inset shows the difference between the computed and CALPHAD values. For bcc Fe, the results obtained by the rMC approach are shown.

puted employing the fluctuation-dissipation theorem. All three ferromagnets are well described, both below and above T_C (see Fig. 3.29). Compared to Fe and Co, the magnetic contribution to C_P is smallest in the case of Ni due to the smallest spin quantum number ($\tilde{S} \approx 0.3$), see Fig. 3.29. The most significant deviations from experiment are observed close to the critical temperature and are most pronounced for bcc Fe. Increasing the system size in the QMC calculations yields a more pronounced peak in C_P (see inset in Fig. 3.29) but has only marginal influence on the overall shape.[25] We note that from the numerical point of view it is challenging to estimate the maximum peak via a finite size scaling ansatz (see e.g. Refs. [148–151]).[26] At the same time the experimental scatter is strongest around T_C due to the rapid change in C_P around the critical point [144].

[25] The impact of the system size N on the free energy turns out to be negligible (i.e. well below 1 meV) for the considered N and temperatures T.

[26] There is a long-standing debate whether the heat capacity of the 3D Heisenberg model shows a finite cusp or diverges. This is inherently connected to the critical exponent α for which different signs (cusp/divergent) have been found. [148–151] However, even if the heat capacity shows a finite cusp, finite-size scaling approaches are very difficult in practice [148].

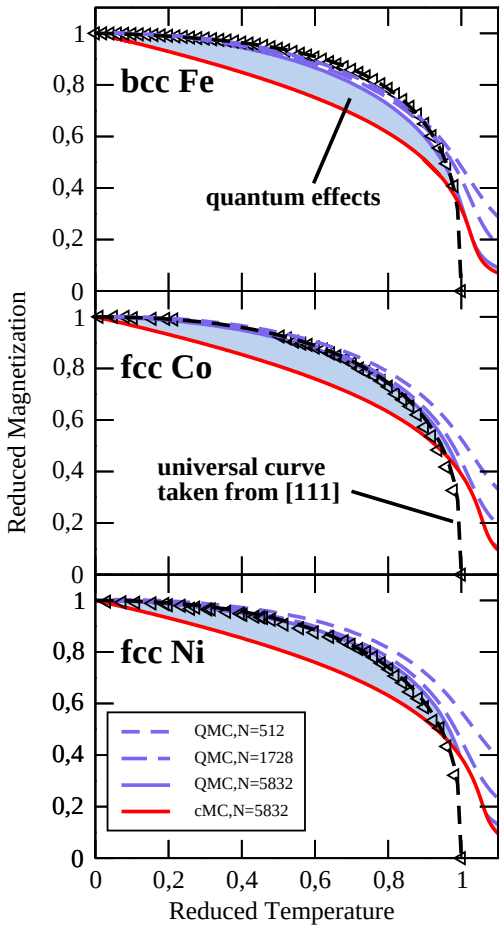

Figure 3.31: The reduced magnetization $m(t) = M(t)/M_0$ *vs.* the reduced temperature $t = T/T_C$ for Fe, Co, and Ni in comparison with experimental data [152]. The numerical calculations are carried out for three different system sizes ($N = 512, 1728, 5832$).

We now turn to the discussion of the Helmholtz free energy Eq. (3.4). The results are shown in Fig. 3.30 in comparison with CALPHAD data. In order to compare the CALPHAD with the *ab initio* derived values we align them at 200 K as before. Similarly to the behavior of the heat capacity, the electronic contribution to the total free energy increases from Fe to Co and reaches its maximum for Ni ($\approx$ 70 meV at 1800 K) due to the smallest band splitting in Ni as discussed above. The remaining differences to the CALPHAD free energy (lower orange line in insets of Fig. 3.30) clearly reveal the necessity to account for the magnetic contribution F^{mag}.

The quantitative impact of F^{mag} on F is reversed compared to the electronic contribution F^{el} (see Fig. 3.30). The strongest magnetic contribution is obtained in the case of bcc Fe ($\approx$ 100 meV at 1800 K) due to the highest spin quantum number ($\tilde{S} \approx 1.1$). Although Co has a larger spin quantum number than Ni, the magnetic contributions in these systems is comparable. The reason for this is that the lower T_C renders the Ni spin system close to the fully disordered state at the high temperatures considered here, whereas in Co a noticeable amount of magnetic free energy remains in the magnetic short-range order. Comparing the total free energies (including all contributions) with

the CALPHAD values we observe a very good agreement for all three ferromagnets. The strongest deviations are observed for bcc Fe ($\approx$ 30 meV at 1800 K) due to the poor description of C_P around T_C (see Fig. 3.29) whereas a nearly perfect quantitative agreement is obtained for Co and Ni ($\approx$ 10 meV at 1800 K).

In Sec. 3.2.1 it has been shown that even sophisticated approaches like the RPA which give a very good qualitative description of C_P and F, can fail to accurately describe the magnetization shape. We made similar observations for classical MC approaches [58]. It is therefore remarkable that our effective model, which reduces the long-ranged magnetic interactions responsible for the magnetization to nearest-neighbor interactions only, also performs very well for $m(t)$. The results are shown in Fig. 3.31 for different system sizes ($N = 512, 1728, 5832$) in comparison with experimental data. The overall shape is in very good agreement for all three ferromagnets. For low temperatures the exact solution of the quantum Heisenberg model ensures that the Bloch $T^{3/2}$-law for $M(T)$ is fulfilled in agreement with experiment. For $T \to T_C$ finite size effects are responsible for the remaining tail in $M(T)$ in the numerical results whereas the second order phase transition (spontaneous symmetry breaking) is obtained in the thermodynamic limit of $N \to \infty$ only. Increasing the system size N reveals a steeper decrease of $M(T \to T_C)$ (similar to the more pronounced peak in C_P in Fig. 3.29) but has only marginal effect on the overall shape.

The fact that classical MC fails to accurately describe the magnetization shape indicates that finite temperature magnetization is substantially affected by spin quantization effects. By performing classical MC calculations using a nearest-neighbor Hamiltonian, which reproduces the same T_C, we have a unique opportunity to quantify the quantum effects. As can be seen in Fig. 3.31, the magnetic contributions (light blue regions) are substantial even at high temperature (i.e. close to T_C) where quantum effects are often assumed to be negligible.

Conclusion

The approach provides a straightforward mapping procedure that transforms the full magnetic Hamilton operator of realistic systems (with long-ranged and oscillating interactions) onto an effective Hamiltonian with nearest-neighbor effective interactions only. It allows to decouple the estimation of T_C - for which approximative methods (e.g., RPA or cMC) work very well - from the determination of other thermodynamic properties. Particular important, the scheme provides a high degree of transferability and performs equally well for Fe, Co, and Ni. This indicates that not only the magnetization shape follows in a wide temperature window an universal behavior [111], but also other thermodynamic properties such as, e.g., the specific heat capacity.

Whereas the considered systems are experimentally well studied, the proposed approach can also be employed to study more complex magnetic systems for which experimental data is missing. In the next section we apply our approach to such a system, i.e., cementite [153, 154], an industrially important ferromagnetic Fe-C alloy.

3.5 Impact of Magnetism on the Phase Stability of Cementite

In the previous section we employed a nearest-neighbor Heisenberg model to compute the magnetic entropy. In combination with the quasiharmonic approximation (vibronic entropy) and finite-temperature DFT (electronic entropy), this approach provided accurate predictions of thermodynamic data for (simple) ferromagnetic systems. In addition, the transferability of the method was shown (all 3d ferromagnets were well described). The approach becomes therewith an ideal candidate to study even more complex ferromagnetic systems. In the following we employ this method to gain a deeper insight into the phase diagram of Fe-C by investigating cementite (Fe_3C).

Fe_3C is one of the key structures which appears in the Fe-C phase diagram, being the predominant carbide in carbon steels [155]. Among others, it allows to control the mechanical properties of steels by mixing the hard and brittle cementite phase with the soft and ductile phase of $\alpha - Fe$ (ferrite). Fe_3C has also attracted significant attention in geophysics due to a recent suggestion that it can be contained in the Earth core [156, 157]. An experimental evaluation of the cementite properties is, however, non-trivial since at ambient pressure it is a metastable phase up to ∼1000 K [158], and experimental samples are typically contaminated with ferrite and bulk carbon phases [159]. This leads to a sizable scatter of the measured data between different experimental studies when considering thermodynamic properties of cementite, such as the thermal volume expansion, the heat capacity, and the heat of formation. Consequently, an unambiguous parametrization of thermodynamic databases within CALPHAD concept becomes cumbersome. In this situation, supplementing experimental datasets, which cannot be easily characterized with existing experimental setups, with results of the first-principles calculations becomes particularly important. So far, however, published first-principles studies are focused on the T=0 K properties only [160–164], and do not take temperature effects into account.

We employ in the following the nearest-neighbor approach to study the thermodynamic properties of cementite. Afterwards we compare our results with a recent thermodynamic assessment of Fe_3C, with an emphasize on the accurate description of the free energy. In addition we discuss the thermodynamic stability of cementite versus the spinodal decomposition into bulk carbon and iron phases by calculating the T-dependent heat of formation of Fe_3C with a particular focus on the magnetic contribution.

3.5.1 Thermodynamic Properties of Fe_3C

To compute the free energy F we apply the adiabatic approximation as we did to compute the thermodynamic properties of bcc and fcc Fe, Co, and Ni. The convergence parameters are chosen such that they ensure a convergence of the final contributions to F to less than 1 meV per atom.[27]

In contrast to experimental data for quantities such as the heat capacity, the critical temperature of Fe_3C is experimentally well known [165]. These preconditions for Fe_3C allow us to employ the nearest-neighbor approach, i.e., it is not necessary to calculate the exchange coefficients for the real system. However, this requires additional approximations for the considered system: Since the

[27] The convergence of the calculated vibrational contribution is ensured by using a supercell consisting of 2x2x2 Fe_3C unit cells (128 atoms), a plane-wave energy cutoff $E_{\text{cut}} = 400$ eV, ∼ 13000 **k**-points per atom in homogeneous Monkhorst-Pack sampling of the Brillouin zone. For the electronic contribution the **k**-point mesh with ∼ 40000 **k**-points per atom was used.

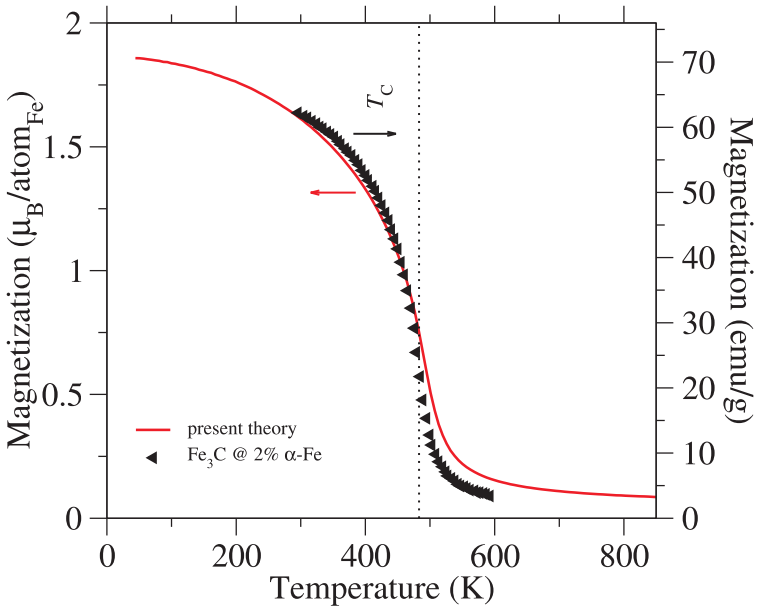

Figure 3.32: Dependence of the simulated Fe_3C magnetization on temperature as compared to the experimental data from Ref. [159]. The experimental data are acquired at a magnetic field of 5 kOe for a mixture of Fe_3C nanoparticles of size 40±10 nm with residual carbon and about 2 wt% α-Fe.

approach is developed for systems containing single magnetic species only, we neglect the magnetic contribution of C atoms. This is justified since their local magnetic moments are much smaller ($\leq 0.01\mu_B$) compared to that of Fe species ($\approx 2\mu_B$). The effective nearest-neighbor Heisenberg model contains therefore Fe-type atoms only. Further, we assume that the Fe atoms are magnetically indistinguishable (carry the same spin).[28]

To employ the nearest-neighbor approach three parameters are needed: the positions of the effective spins, the effective nearest-neighbor exchange parameter J, and the effective spin quantum number. The cell geometry and the atomic positions are taken from the DFT calculations and a model containing a 6x6x6 supercell (3456 atoms) is build up. The effective nearest-neighbor exchange parameter J is determined by ensuring the correct experimental value of $T_C^{\text{exp}} = 483$ K [165]. From the DFT calculations the equilibrium local magnetic moments of Fe atoms are computed as $M_{\text{Fe}}^0 \approx 1.9\ \mu_B$ providing an effective spin $\tilde{S} \approx 0.95$ of the Fe_3C system. According to (3.49) the QMC simulations are performed using the spin quantum number $S = 1$ and $S = 0.5$ and an interpolation afterwards.

The theoretical temperature dependence of the magnetization in comparison with the corresponding experimental data is shown in Fig. 3.32. Please note the different scales on the right and left axis. A quantitative comparison of the theoretical and the experimental data is hindered by the presence of a mixture of Fe_3C and carbon in the experiments. Figure 3.32 shows, however, that qualitatively the magnetization in Fe_3C is well reproduced consistent with the results for the pure ferromagnets Fe, Co, and Ni (see also Fig. 3.31).

[28] Strictly speaking, there are two types of Fe-atoms in the unit cell which differ in the local magnetic moment by less than $0.1\mu_B$.

In Fig. 3.33 the calculated specific heat capacity, the corresponding available experimental data and the results of different empirical assessments are presented. The theoretical heat capacity is further split into the vibronic, electronic and magnetic contributions.[29] As for the other studied systems (Fe, Co, Ni), we find that the dominating contribution originates from the vibronic excitations showing a typical Debye behavior at low temperatures ($\sim T^3$) and a linear increase at high temperatures. We also observe a significant contribution due to electronic excitations which is due to the high density of electronic states close to the Fermi level in Fe_3C [160]. The magnetic contribution of the heat capacity is largest at T_C due to the break down of the long-range magnetic order. Below 200 K (close to ferromagnetic saturation) as well as high temperatures (paramagnetic state), it smoothly vanishes to zero. We can conclude that for temperatures larger than $\approx$ 1000 K, the electronic and vibronic contributions are responsible for the linear increase in the theoretical C_P.

Comparing our results with the available measurements of the heat capacity at constant pressure (Fig. 3.33) below the Curie temperature we find that our predicted theoretical curve falls within the scatter interval between different measurements[30]. Above T_C, our curve is located practically on-top of the measurements of Naeser [166], and reproduces the presence of a local minimum at $T \sim 600$ K and the increase at higher temperatures. These results are also consistent with the empirical CALPHAD assessments by Chipmann [158] and Darken *et al.* [167]. There is a strong deviation between the above described behavior and the recent measurements by Umemoto and coworkers where C_P steeply increases with the temperature above T_C [165]. The latest empirical assessment of C_P by Hallstedt *et al.* [153], where the heat capacity above 600 K is assumed to be constant and which is on-top of the experiments by Seltz *et al.* [168] below the Curie temperature, is within the 10 J mol^{-1}K^{-1} from first-principles results up to T=1500 K.

In Fig. 3.34 we compare the calculated free energy $F_{Fe_3C}(T)$ with the CALPHAD data of Hallstedt *et al.* [153].[31] Due to the different description of C_P for the computed data and the empirical assessment (Fig. 3.33), both datasets slightly and linearly deviate above $\approx$ 200 K. Considering the magnetic free energy of Fe_3C, substantial differences in the balance exist compared to our results of pure bcc Fe. In the considered temperature window (up to 1500 K) the magnetic contribution in pure iron is weaker than the one of Fe_3C. Although both systems exhibit a similar maximum magnetic entropy $S_{\mathrm{mag}}^{\mathrm{max}}$ (due to the similar magnetic moments), $S_{\mathrm{mag}}^{\mathrm{max}}$ in Fe_3C is reached at lower temperatures due to the significantly lower T_C when compared to that of bcc iron. In general we obtain an excellent agreement of the theoretical and the experimental free energies with deviations below 15 meV/atom up to T=1500 K.

[29] Data for vibronic and electronic contributions for Fe_3C and diamond are taken from Alexey Dick.

[30] The large discrepancy at $T > T_C$ of the measured heat capacity in Ref. [165] is unclear and is likely to do with the quality of the samples and/or their preparation procedure.

[31] We note, that due to the large scatter in the experimental data that underlies the Hallstedt *et al.* assessment, these results which we use as benchmark are subject to an uncertainty that should be reduced in the future by improved experimental setups.

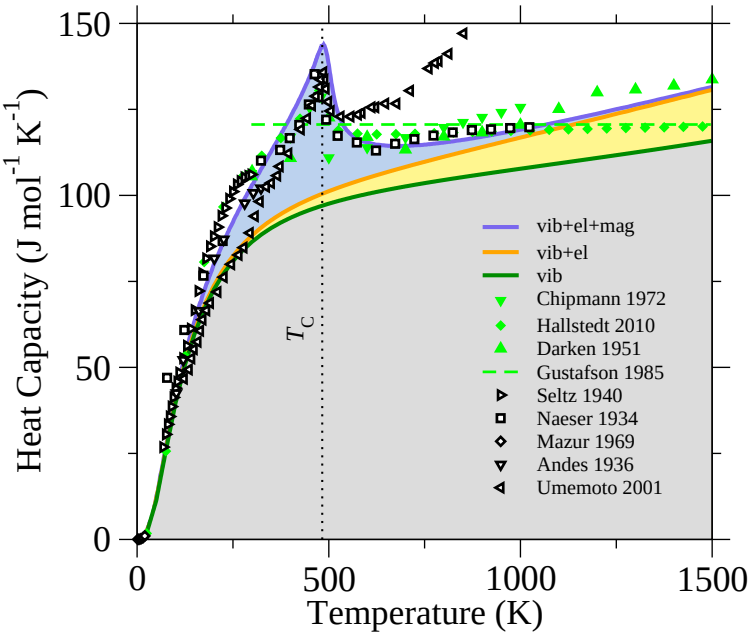

Figure 3.33: Calculated heat capacity of cementite in comparison with available experimental data (open black symbols) and thermodynamic assessments (filled green symbols). The different theoretical contributions are indicated by shaded areas (vibronic grey, electronic orange, magnetic blue).

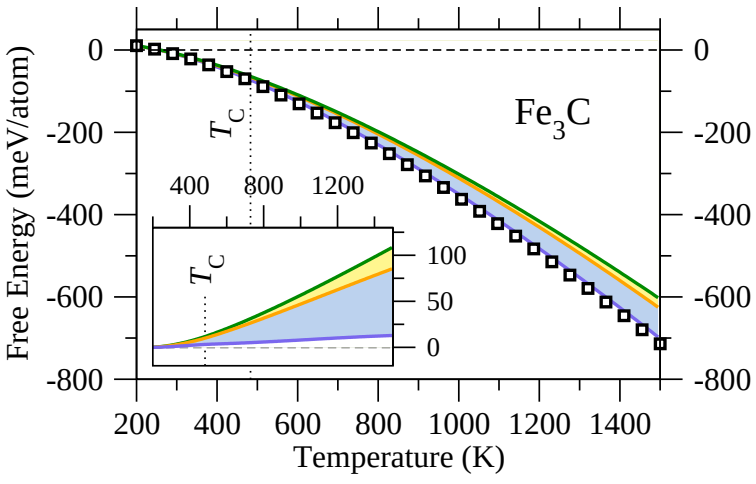

Figure 3.34: Calculated free energy for Fe_3C in comparison with the available thermodynamic assessment from Ref. [153]. The first-principles (blue line) and the CALPHAD curves (open black squares) are aligned at $T = 200$ K. The calculated electronic and magnetic contributions to the free energy are indicated by shaded orange and blue areas correspondingly. Inset: Difference between *ab initio* and CALPHAD result.

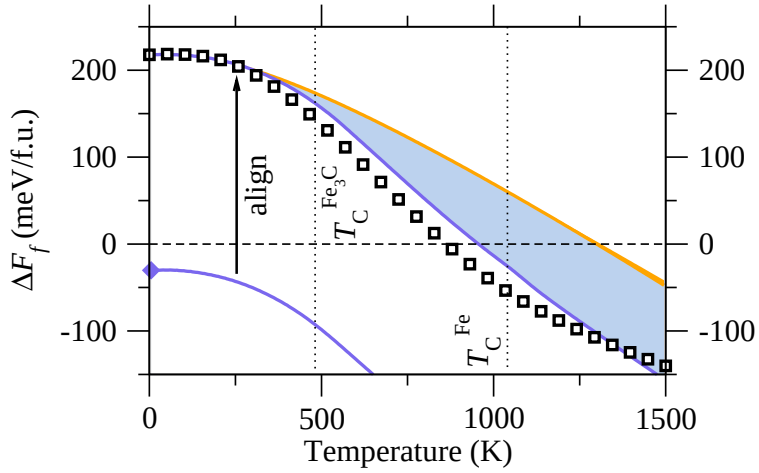

Figure 3.35: Calculated free energy of formation of cementite from α-Fe and diamond as a function of temperature. For comparison the CALPHAD assessment as given in [153] is shown. For an easier comparison of the temperature dependence, the present theoretical curves aligned to the empirical value at $T = 0$ K are also shown. The calculated electronic and magnetic contributions to the free energy are shown as shaded orange and blue areas correspondingly.

3.5.2 Phase stability of Fe_3C

In order to analyze the stability of Fe_3C versus bulk iron and carbon phases, and to compare it with available CALPHAD assessments, we consider the free energy of formation of Fe_3C:

$$\Delta F_f^{Fe_3C}(T) = F_{Fe_3C}(T) - (3F_{Fe}(T) + F_C(T)) \,. \tag{3.50}$$

Here, $F_{Fe}(T)$ is the free energy of bcc Fe taken from Sec. 3.4. $F_C(T)$ in the above equation denotes the free energy of bulk carbon. Typically, in experimental and empirical models only the thermodynamically stable phase of graphite is considered [153]. It is well known, however, that conventional exchange-correlation functionals used in DFT calculations fail to accurately describe the weak correlation forces of van de Waals type present in graphite. Therefore, instead of graphite only the diamond phase is considered here. The results obtained using graphite as reference reveal, however, qualitatively the same findings. For a detailed discussion we refer to [154].

Employing (3.50) we analyze now the phase stability for Fe_3C. A positive formation energy indicates that Fe_3C is thermodynamically unstable versus spinodal decomposition into bulk Fe and C phases. The resulting calculated heat of formation $\Delta F_f^{Fe_3C}(T)$ is shown in Fig. 3.35. At $T = 0$ K the predicted energy of formation is significantly lower (by $\approx$ 250 meV per formula unit) than the empirical assessment. The calculations predict Fe_3C to be thermodynamically stable at all temperatures.[32]

In order to separate the accuracy of describing ground-state properties from the finite temperature effects, we align the theoretical ΔH_f with the empirical curves at T=0 K. The aligned curves

[32] In [154] it is shown that the results are not improved by taking all-electron methods into account. The failure can be traced back to the used xc-functional which performs particular bad for the cohesive energies of Fe and Fe_3C.

are also shown in Fig. 3.35. We separate the magnetic and electronic contributions in order to illustrate their impact on the stable-unstable transition temperature $\Delta T_{\mathrm{Fe_3C}}$.

Considering the aligned ΔH_f and taking only vibronic contributions into account, we observe a stabilization of Fe_3C at about 1300 K which is significantly larger than the empirical predicted $\Delta T^{\mathrm{emp}}_{\mathrm{Fe_3C}} = 860$ K. The electronic excitations are almost vanishing for ΔH_f and have practically no influence on $\Delta T_{\mathrm{Fe_3C}}$. This is due to the almost compensating contributions for α-Fe and Fe_3C, whereas the diamond phase has a negligible electronic contribution.[33] In contrast to the electronic excitations, a strong impact of the magnetic entropy contribution can be expected, since the critical temperatures of α-Fe and Fe_3C strongly differ. Adding the magnetic excitations to the vibronic and electronic heat of formation leads to a significant decrease of the transition T by more than ~ 350 K and we obtain ultimately a theoretical predicted temperature $\Delta T^{\mathrm{theo}}_{\mathrm{Fe_3C}} = 950$ K at which the cementite becomes thermodynamically stable over the α-Fe and bulk carbon.

Conclusion

Using our developed combined *ab initio* approach employing the nearest-neighbor ansatz (Sec. 3.4) it is possible to calculate the thermodynamic properties of Fe_3C with a high degree of accuracy. The quantitative deviations from the available experimental measurements are found to be smaller than 0.1% and 10 $\mathrm{mol^{-1}K^{-1}}$ for temperatures up to 1500 K for the atomic volume and the heat capacity, respectively. Noteworthy, that the magnitude of these deviations is comparable with the one between different experimental data themselves. Comparing the results for the free energy with the recent empirical assessment shows that up to T=1500 K these energies differ by less than 10 meV/atom over the whole considered temperature range.

To investigate the impact of magnetic contributions on the thermodynamic stability of Fe_3C against decomposition into bulk Fe and C phases the free energy of formation is calculated. Aligning the heat of formation at T=0 K to the corresponding experimental value we show that the thermal excitations are accurately described within the present theory, providing a prediction of the transition temperature $\Delta T_{\mathrm{Fe_3C}}$ only $\sim$100 K above the corresponding empirical value. Such an agreement is remarkable when taking into account the uncertainty which persists in the empirical assessment.

The calculations further indicate that the largest deviation from the empirical assessment occur for the zero-temperature heat of formation (in the order of 200 meV per formula unit). On the other hand the T-dependence of the theoretical heat of formation is described with a high degree of accuracy. A similar result was found in Ref. [80] by investigating a large set of non-magnetic materials employing similar methods for vibronic and electronic excitations. It shows that the accuracy of the existing exchange-correlation functionals for prediction of the heat of formation at T=0 K should be improved in the first place. For complex ferromagnetic systems, when the temperature-dependent properties and trends are of importance, the existing approach can already be used as complementary (or substituting) method to existing empirical and experimental schemes. An incorporation into the CALPHAD approach is planned.[34]

[33] Since diamond is an insulator, the electronic entropy contribution is much smaller than for α-Fe and Fe_3C.
[34] Private discussions with Dr. B. Hallstedt, RWTH Aachen.

Chapter 4

Summary and Outlook

In the present work a major challenge in computationally guided materials design has been addressed and to a large part solved: the *ab initio* prediction of *finite-temperature* properties of *magnetic* materials. The accurate description of the magnetic contribution makes an interplay of various theoretical treatments mandatory. For this purpose, a careful and profound analysis of different solution techniques of the Heisenberg model has been performed. The developed methods have been evaluated for a well studied magnetic material, namely bcc iron, but have been also extended to more complex magnetic materials like cementite. The presented techniques build up a firm basis to compute the magnetic entropy contribution from first principles and to address present questions in materials design.

For iron-based materials, the Heisenberg model has proven to yield a numerically efficient yet sufficiently accurate description of magnetic excitations. It provides an elegant way to couple ground state *ab initio* calculations, which are used to determine the exchange integrals, with concepts of many-body theory to describe the full temperature dependence of excited magnetic states and to predict critical temperatures (Sec. 3.1). Beyond efficiency, the big advantage of the analytic solutions is that they allow to decouple the different physical mechanisms contributing to the Curie temperature T_C. Utilizing this, we revealed that the dependence of T_C on pressure results from an interplay between two competing pressure-dependent mechanisms: the *increase* of the *magnetic coupling* between the localized magnetic moments and the simultaneous *decrease* of their magnitude under the increase of the external pressure. While the first mechanism tends to increase the Curie temperature, the second mechanism acts against it. In the particular case of bcc iron they nearly completely compensate each other. It is expected that such a nearly perfect compensation for bcc iron is not an universal feature of all ferromagnetic materials, but is, likely, an exception. Nevertheless, the proposed picture of two competing magnetic mechanisms can be used for an intuitive interpretation of the physical reasoning underlying different behaviors of the pressure-dependent Curie temperature in other ferromagnetic materials.

In order to use the combination of DFT and the Heisenberg model for realistic materials, a number of analytical and numerical approaches have been implemented and carefully checked with respect to numerical efficiency and predictive power. In this context, the specific heat capacity C_p has been identified as a critical quantity, which provides also a close link to experiments and in addition to empirical CALPHAD simulations. An analytical approach to the free energy of the Heisenberg spin system (Sec. 3.2.1), which is based on the random phase approximation (RPA), in

combination with vibronic (quasiharmonic approximation) and electronic (finite temperature DFT) contributions, has allowed us to obtain a remarkably accurate description of C_p below the critical temperature. For a proper description of the region above the critical temperature, however, short range correlations are critical and needed to be taken into account. Therefore, various Monte Carlo (MC) schemes have been explored. Classical MC calculations that neglect quantum effects, yield significant short comings below the critical temperature (Sec. 3.2.2). This implies an important (and surprising) conclusion: Quantum effects are important even at temperatures up to T_C, which is for bcc iron already about 1000 K!

Therefore, a rescaling scheme has been derived from an extensive set of quantum and classical Heisenberg model systems, which provides the accuracy of quantum MC calculations, yet keeping the full flexibility of the classical MC approach. The proposed analytic rescaling function fulfills exact high-temperature and high-spin limits and transforms at low temperatures into an analytic mean field solution. Employing the rescaling function significantly improves the deficiencies of the original classical MC data at low temperatures even for realistic systems such as bcc iron. Due to its straightforward applicability, it could be used whenever classical MC calculations are carried out and allows a good estimation of the expected quantum effects. In contrast to the analytic RPA as well as the classical MC results, the rescaled MC approach has proven to allow a complete and consistently good description of the magnetic entropy at temperatures below *as well as* above T_C.

Applying the methods to antiferromagnetic fcc iron, classical MC calculations and the analytic RPA method have provided similar predictions for the Néel temperature. Combining the derived magnetic entropy contribution with electronic and vibronic excitations, a free energy of fcc iron is obtained similar to the results provided by the CALPHAD approach. Due to the possibility of deriving free energies of single phases (here, bcc and fcc iron), the investigation of phase transitions has become feasible. The impact of different entropy contributions on the phase transitions of iron has been analyzed. It was thus possible to settle down a long standing debate regarding the impact of vibronic contributions. They are (together with electronic contributions) equally important for the stabilization of the fcc crystal phase as magnetic contributions. Based on the magnetic entropy contributions, an intuitive explanation of the phase transitions could be provided: on the one hand, the austenite is stabilized at intermediate temperatures due to the lower critical temperature compared to ferrite. At high temperatures, on the other hand, the backward transition from the austenite to the paramagnetic δ-iron is driven by the larger magnetic entropy of bcc iron due to the larger spin moment compared to the fcc phase.

Analyzing the classical and quantum results for various model systems of the previous comparison in more detail (Sec. 3.2.2), a universal behavior of the thermodynamic properties with respect to the kind of the interaction (long- vs. short-ranged, ferro- vs. antiferromagnetic) and the lattice structure has been discovered for the Heisenberg model. This universality has motivated the definition of an effective nearest-neighbor Heisenberg model with just one interaction parameter. The latter is, e.g., related to T_C, which can be either determined by *ab initio* calculations (Sec. 3.1) or taken from experiment. Treating this effective model with quantum MC has provided for bcc Fe an excellent agreement with experimental C_p data and free energies (Sec. 3.4). The application of the same approach to the 3d ferromagnets cobalt and nickel has demonstrated its excellent transferability to other magnetic systems containing a single magnetic species. Therefore, the developed methodology has been applied to more complex systems, such as, e.g., cementite (Fe_3C), which is

a highly relevant phase for steel design (Sec. 3.5). Due to a large scatter in the experimental $C_p(T)$ an unambiguous thermodynamic assessment (e.g., CALPHAD) of this system is challenging. As it has been demonstrated in Sec. 3.5, the method has not only provided a clear prediction of $C_p(T)$ particularly in the high temperature regime, it also has provided a hitherto not achieved insight into the impact of magnetic contributions to the phase stability of Fe_3C.

In conclusion, the set of *ab initio* based methodologies developed in this work has allowed a reliable and parameter-free prediction of the magnetic contribution to the free energy of materials, a systematic separation from other physically relevant contributions to the thermodynamic properties, and can be applied to a wide range of materials.

The developed methods in this study open up a huge number of potential investigations which can now be tackled. Still, several aspects of the developed methodologies can be improved or extended. In order to give a flavor of the possible next steps we summarize in the following the most important issues:

Multi-magnetic species systems:
In order to treat systems containing more than one kind of magnetic atom (such as FeMn-compounds), the developed theories have to be extended. Concerning the analytic approaches, a corresponding theory for obtaining T_C based on the RPA scheme already exists [169]. To extend the developed theory to describe thermodynamic properties such as free energy and heat capacity, principally a similar approach as in Sec. 3.2.1 could be used. Such an extension should be straightforward, although likely requiring a considerably longer analytic derivation.

Regarding the rescaled Monte Carlo approach, the model calculations should be extended to the case of multi-spin lattices in the first place. After a detailed model comparison between the classical and quantum results, a modified rescaling ansatz may be derived. In order to apply the nearest-neighbor approach to a multi-magnetic-species system, most likely an additional effective exchange coefficient is needed. This could be problematic regarding that the mapping of the long-ranged onto the effective nn-model is currently done by just one conserving parameter i.e. T_C. As a first order approximation one could assume that the exchange between different kind of magnetic atoms as well as the different spin moments can be described by one effective (averaged) exchange parameter and one effective spin quantum number, respectively. Under this assumption, both methods can be straightforwardly applied without further methodological extensions, and are equally well suited to treat such systems.

Noteworthy, that regarding the DFT input, the computation of exchange-parameters for multi-component-systems is already well established [169].

Inclusion of longitudinal spin fluctuations:
The impact of longitudinal spin fluctuations, i.e., the change of the magnitude of the local magnetic moments, is not clarified. One should distinguish between the explicit and implicit temperature dependence of the local moments and exchange coefficients. The first one is determined by explicit temperature dependent excitation processes such as, e.g., single-spinflip processes of electrons or flip processes of electrons between different bands. Their inclusion into the proposed Heisenberg model ansatz is conceptually difficult and requires most likely band-model based theories (Hubbard model) [39, 170] and an additional mapping onto effective exchange coefficients. The extension to multi-magnetic material systems is expected to be rather difficult. A straightforward first step

could be, to employ the already developed methods using different electronic temperatures (Fermi smearing) within the DFT formalism.[1]

The implicit dependence of the local moments and effective exchange coefficients, i.e., their change due to volume expansion or magnetic disorder, can be simulated by DFT calculations directly. Different methodologies are nowadays available (e.g., the so-called disordered local moment method [171]) to simulate the paramagnetic state at $T = 0$ K. Based on these calculations, effective and implicitly temperature dependent (via the coupling of the local moment to the magnetic state) exchange coefficients can be computed. A recent incorporation of the latter into the classical Heisenberg model reveals promising results for Fe and Ni [48]. The inclusion of these implicit LSF could be straightforwardly done in the rescaled MC approach (via the spin-dependent rescaling function). Based on the findings in [48], it is expected that incorporating the LSF into the methodologies might be potentially important for systems showing small band splitting like Ni, but should not have significant impact on results of strong-moment systems such as Fe.

Coupling terms:
In the present study, the different types of excitations are treated in an adiabatic approximation. In addition, the electronic and vibronic contributions were performed for the magnetic ground-state configuration, e.g., for the ferromagnetic state of bcc Fe. This implicitly ignores the dependence of vibronic excitations on the magnetic state.

To account for this coupling (phonons in different magnetic states etc.), a very promising route was very recently proposed by Shang and Liu [172]. They propose to perform total energy and phonon calculations for a number of different magnetic states and to average afterwards following a Boltzmann statistic. Physically, this corresponds to the situation that the system at a given temperature is determined by the occupation of different (magnetic) micro states. Naturally, coupling terms between electronic-magnetic and vibronic-magnetic contributions are in such an approach implicitly included. Whereas the recent approach ignores the explicit magnetic contributions [172], a complete approach can be immediately employed using our developed methods.

Impurity dependent trends of the critical temperature:
Since T_C is taking an important role in the developed methods, it would be interesting to investigate how it is affected by different impurities such as, e.g., carbon. This would thus provide the next step towards a complete theoretical prediction of the Fe-C phase diagram. For the study of the thermodynamic properties of cementite for example, the *ab initio* determination of T_C, which here has been taken from experiment, is a natural next step to achieve a fully first-principles Fe_3C prediction. This itself would be already an important issue since very little is known about the dependence of T_C of Fe_3C on different impurities, particularly, considering the fact that the different critical temperatures of ferrite and cementite play a crucial role for the stabilization of Fe_3C. Since the underlying methods have been developed, such a study could be immediately started.

[1] This could only simulate the different occupations within the spin bands. However, such an ansatz can not account for temperature induced electronic intra- or inter-band flips.

Pressure-temperature phase diagrams:
Although an *absolute quantitative* agreement between theory and experiment for total free energies of pure Fe is not achieved, an investigation of physical *trends* is possible such as, e.g., the dependence of different physical mechanisms on pressure. Regarding the rather complex dependencies for the stability of different Fe crystal phases on pressure, a simple mean-field ansatz could in principle already provide important insights. Employing MF, the required ingredients for the different crystal phases λ are the critical temperatures $T_C^\lambda(V)$ as well as the local magnetic moments $M^\lambda(V)$ (both may depend on volume).

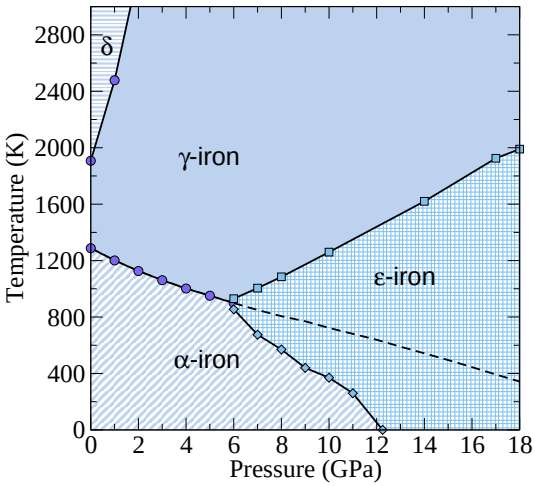

Assuming as a first order approximation $T_C^\lambda(V) \approx T_C^\lambda$, the MF free energy $F_{\mathrm{MF}}^{\mathrm{mag}}(T, V, \lambda)$, Sec. 3.2.1, can be straightforwardly employed and combined with the ground state energies $E^\lambda(V)$. Preliminary results are already available and shown in the figure above. The dashed line indicates the theoretical ferrite to austenite transition temperatures. Further development in this direction is planned, in particular to elucidate the impact of the different contributions with respect to pressure.

Appendix A

Appendix

A.1 Mean Field Approximation for Ferromagnets

The employed mean field (MF) theory is derived as, e.g., found in Ref. [56].

A.1.1 The Mean Field Hamiltonian

The mean field approximation is realized by the following treatment for operator products AB

$$\begin{aligned} AB &= A\langle B\rangle + \langle A\rangle B - \langle A\rangle\langle B\rangle + (A - \langle A\rangle)(B - \langle B\rangle) && \text{(A.1)} \\ &\rightarrow A\langle B\rangle + \langle A\rangle B - \langle A\rangle\langle B\rangle. && \text{(A.2)} \end{aligned}$$

Within MF, fluctuations of A and B are neglected, i.e.

$$(A - \langle A\rangle)(B - \langle B\rangle) \quad \rightarrow \quad 0. \tag{A.3}$$

Thus, the Heisenberg Hamiltonian transforms into

$$\begin{aligned} \mathcal{H} &= -\sum_{ij} J_{ij}\mathbf{S}_i\mathbf{S}_j && \text{(A.4)} \\ &= -\sum_{ij} J_{ij}(S_i^+ S_j^- + S_i^z S_j^z) && \text{(A.5)} \\ &\xrightarrow{\text{MF}} -\sum_{ij} J_{ij}(\langle S_i^z\rangle S_j^z + S_i^z\langle S_j^z\rangle) + \sum_{ij} J_{ij}\langle S_i^z\rangle\langle S_j^z\rangle. && \text{(A.6)} \end{aligned}$$

Due to spin conservation at each lattice site, $\langle S_i^+\rangle = \langle S_i^-\rangle \equiv 0$, collective spin-wave excitations (correlations) are supressed

$$\langle S_i^+ S_j^-\rangle \quad \xrightarrow{\text{MF}} \quad 0. \tag{A.7}$$

Assuming homogeneous magnetization,

$$\langle S_i^z\rangle \equiv \langle S^z\rangle, \tag{A.8}$$

the Hamiltonian reads as

$$\mathcal{H}_{\mathrm{MF}} \;:=\; J_0\langle S^z\rangle^2(T) - B_{\mathrm{EX}}(T)\sum_i S_i^z, \tag{A.9}$$

with an effective (mean field) exchange field,

$$B_{\mathrm{EX}}(T) \;:=\; 2J_0\langle S^z\rangle(T), \tag{A.10}$$

which is proportional to the magnetization $\langle S^z\rangle$.

A.1.2 The Mean Field Magnetization

Within mean field, the partition sum Z separates into one-spin partition sums z_1, i.e.

$$Z = Tre^{-\beta\mathcal{H}} = z_1^N C, \tag{A.11}$$

with

$$z_1 = \sum_{S_i^z=-S}^{+S} e^{\beta B_{\mathrm{EX}}(T)S_i^z} \tag{A.12}$$

and the constant

$$C = \sum_{S_i^z=-S}^{+S} e^{-\beta J_0\langle S^z\rangle^2(T)} = (2S+1)e^{-\beta J_0\langle S^z\rangle^2(T)}, \tag{A.13}$$

which cancels when calculating observables (see derivation below).
The procedure is equivalent to Weiss theory of ferromagnetism (see e.g. [56]),

$$\begin{aligned}
\langle S_i^z\rangle/S &= \frac{TrS_i^{z'}e^{-\beta\mathcal{H}^{\mathrm{MF}}}}{STre^{-\beta\mathcal{H}^{\mathrm{MF}}}} && \text{(A.14)}\\
&= \frac{\sum_{-S}^{+S} S_i^{z'}e^{-\beta(J_0\langle S^z\rangle^2(T) - B_{\mathrm{EX}}(T)\sum_i S_i^{z'})}}{S\sum_{-S}^{+S} e^{-\beta(J_0\langle S^z\rangle^2(T) - B_{\mathrm{EX}}(T)\sum_i S_i^{z'})}} && \text{(A.15)}\\
&= \frac{\sum_{-S}^{+S} S_i^{z'}e^{\beta B_{\mathrm{EX}}(T)\sum_i S_i^{z'}}}{S\sum_{-S}^{+S} e^{\beta B_{\mathrm{EX}}(T)\sum_i S_i^{z'}}} && \text{(A.16)}\\
&= B_S(\frac{2S^2J_0}{k_BT}\frac{\langle S^z\rangle}{S}), && \text{(A.17)}
\end{aligned}$$

where the Brillouin function $B_S(x)$ is given by

$$B_S(x) \;:=\; \frac{2S+1}{2S}\coth(\frac{2S+1}{2S}x) - \frac{1}{2S}\coth(\frac{x}{2S}). \tag{A.18}$$

A.1.3 Mean Field Solution of $f(t,S)$ for Low Temperatures

Within mean field, the internal energy is proportional to the squared magnetization,

$$U^{\mathrm{MF}}(t,S) \sim m^{\mathrm{MF}}(t,S)^2, \tag{A.19}$$

where the latter is given by

$$m^{\mathrm{MF}}(t,S) \sim B_S\left(\frac{3S}{S+1}\frac{m(t,S)}{t}\right), \tag{A.20}$$

including the Brillouin function

$$B_S(x) = \frac{2S+1}{2S}\coth\left(\frac{2S+1}{2S}x\right) - \frac{1}{2S}\coth\left(\frac{1}{2S}x\right). \tag{A.21}$$

For $S \to \infty$, above function transforms into the Langevin function

$$B_{S\to\infty}(x) = L(x) = \coth(x) - \frac{1}{x}. \tag{A.22}$$

For low temperature, i.e. $x \gg 1$, one obtains

$$B_S(x \gg 1) = 1 - \frac{\exp(-x/S)}{S} \tag{A.23}$$

$$L(x \gg 1) = 1 - 1/x. \tag{A.24}$$

Combining Eqs. (A.19)-(A.24), one obtains straightforwardly the low temperature expansion for the heat capacity,

$$C^{\mathrm{MF}}(t,S) = -\frac{3}{2}k_B\frac{S}{S+1}\frac{dm^2(t,S)}{dt}, \tag{A.25}$$

as

$$C^{\mathrm{MF}}(t\to 0,S) \approx k_B\left(\frac{2t_S^{\mathrm{MF}}/t}{\exp(t_S^{\mathrm{MF}}/t)}\right)^2 \tag{A.26}$$

$$C^{\mathrm{MF}}(t\to 0,S\to\infty) \approx \frac{k_B}{2}\left(1+\frac{1}{\sqrt{1-4/3t}}\right), \tag{A.27}$$

with the spin-dependent variable

$$1/t_S^{\mathrm{MF}} \equiv 2/3(S+1). \tag{A.28}$$

Therewith, the ratio of the quantum and classical ($S \to \infty$) heat capacity in the low temperature limit $t \to 0$,

$$\lim_{t\to 0} f^{\mathrm{MF}}(t,S) = \lim_{t\to 0} C^{\mathrm{MF}}(t,S)/C^{\mathrm{MF}}(t,S\to\infty), \tag{A.29}$$

can be readily computed and we obtain

$$f^{\mathrm{MF}}(t\to 0,S) = \left(\frac{2t_S^{\mathrm{MF}}/t}{\exp(t_S^{\mathrm{MF}}/t)}\right)^2. \tag{A.30}$$

A.2 Random Phase Approximation for Ferromagnets

The magnetization is derived as in Ref. [61] employing the random phase approximation (RPA) and using a parametrized Green's function.

We start with the following identity:

$$\langle S_i^- S_i^+ \rangle = \hbar^2 S(S+1) + \hbar \langle S_i^z \rangle - \langle (S_i^z)^2 \rangle. \tag{A.31}$$

The operator product $(S_i^z)^2$ on the right site of the equation above requires a Green's function which provides the relation between the expectation values of the power set of $(S_i^z)^n$. For this purpose, we employ a parametrized Green's function and follow a procedure proposed by Callen [61].

To determine the magnetization we introduce the following retarded Green's function:

$$G_{ij}^{(a)} = \langle\langle S_i^+ ; B_j^{-(a)} \rangle\rangle = \langle\langle S_i^+ ; e^{aS_j^z} S_j^- \rangle\rangle. \tag{A.32}$$

Thus, we obtain for the equation of motion

$$E G_{ij}^{(a)}(E) = \hbar \langle [S_i^+ ; B_j^{-(a)}]_- \rangle + \langle\langle [S_i^+, \mathcal{H}]_- ; B_j^{-(a)} \rangle\rangle_E. \tag{A.33}$$

For the solution we need the inhomogeneity

$$\langle [S_i^+ ; B_j^{-(a)}]_- \rangle = \langle \left[S_i^+, e^{aS_i^z} S_i^- \right]_- \rangle \delta_{ij} = \eta^{(a)} \delta_{ij}, \tag{A.34}$$

as well as the commutator $[S_i^+, \mathcal{H}]_-$. Employing the RPA yields

$$\frac{1}{\hbar} \frac{1}{N} \sum_i e^{i\boldsymbol{q}\boldsymbol{R}_i} [S_i^+, \mathcal{H}]_- = \left[S_{\boldsymbol{q}}^+, \mathcal{H} \right]_- \overset{RPA}{\longrightarrow} 2 \left(J_0 - J_{\boldsymbol{q}} \right) \langle S^z \rangle =: E_{\boldsymbol{q}}. \tag{A.35}$$

With Eqs. (A.34) and (A.35) we can write down the equation of motion

$$\frac{1}{\hbar} G_{\boldsymbol{q}}^{(a)} = \frac{\eta^{(a)}}{E - E_{\boldsymbol{q}}}. \tag{A.36}$$

The spectral density, $S_{\boldsymbol{q}}^{(a)} = -\frac{1}{\pi} \Im G_{\boldsymbol{q}}^{(a)+-}$, can be written as a delta-function:

$$S_{\boldsymbol{q}}^{(a)} = \hbar \eta^{(a)} \delta(E - E_{\boldsymbol{q}}). \tag{A.37}$$

Using the spectral theorem and Eq. (A.37) we can determine the expectation value

$$p(\boldsymbol{q}, a) = \frac{1}{N} \sum_{ij} e^{i\boldsymbol{q}(R_i - R_j)} \langle e^{aS_j^z} S_j^- S_i^+ \rangle \tag{A.38}$$

$$= \frac{\eta^{(a)}}{e^{\beta E(\boldsymbol{q})} - 1}. \tag{A.39}$$

We sum over all wave vectors $\boldsymbol{q}$ and end up with:

$$\overline{p}(a) = \frac{1}{N}\sum_{\boldsymbol{q}} p(\boldsymbol{q}, a) = \langle e^{aS^z} S^- S^+ \rangle =: \eta^{(a)}\varphi, \tag{A.40}$$

where we define the effective Magnon occupation number

$$\varphi = \frac{1}{N}\sum_{\boldsymbol{q}} \frac{1}{e^{\beta E(\boldsymbol{q})} - 1}. \tag{A.41}$$

We obtain the desired Eigenvalue $\langle S^z \rangle$ using a differential equation

$$\begin{aligned} \Omega(a) &= \langle e^{aS^z} \rangle & \text{(A.42)} \\ \langle S^z \rangle &= \frac{d}{da}\Omega(a)\Big|_{a=0}. & \text{(A.43)} \end{aligned}$$

To derive the relation between $\overline{p}(a)$, $\eta(a)$ and a we use the identity (proof by induction)

$$\left[S_i^+, (S_i^z)^n\right]_- = \left((S_i^z - \hbar)^n - (S_i^z)^n\right) S_i^+ \tag{A.44}$$

which yields

$$\begin{aligned} \left[S_i^+, e^{aS_i^z}\right]_- &= \sum_n \frac{1}{n!} a^n \left[S_i^+, (S_i^z)^n\right]_- & \text{(A.45)} \\ &= \sum_n \frac{1}{n!} a^n \left((S_i^z - \hbar)^n - (S_i^z)^n\right) S_i^+ & \text{(A.46)} \\ &= \left(e^{-a\hbar} - 1\right) e^{aS_i^z} S_i^+. & \text{(A.47)} \end{aligned}$$

We can now write down $\eta(a)$

$$\begin{aligned} \eta(a) &= \langle \left[S_i^+, e^{aS_i^z} S_i^-\right]_- \rangle & \text{(A.48)} \\ &= \langle e^{aS_i^z} \left[S_i^+, S_i^-\right]_- + \left[S_i^+, e^{aS_i^z}\right]_- S_i^- \rangle & \text{(A.49)} \\ &= 2\hbar \langle e^{aS_i^z} S_i^z \rangle + \left(e^{-a\hbar} - 1\right) \langle e^{aS_i^z} S_i^+ S_i^- \rangle. & \text{(A.50)} \end{aligned}$$

Using the identity

$$\hbar S_i^z = \hbar^2 S(S+1) - (S_i^z)^2 - S_i^- S_i^+ \tag{A.51}$$

it follows

$$\begin{aligned}
\eta(a) &= \left(e^{-a\hbar}-1\right)\langle e^{aS_i^z}\rangle\hbar^2 S(S+1)+ \\
&+ \langle e^{aS_i^z}S_i^z\rangle\left(2\hbar+\hbar e^{-a\hbar}-\hbar\right)- \\
&- \left(e^{-a\hbar}-1\right)\langle e^{aS_i^z}\,(S_i^z)^2\rangle \qquad (A.52)\\
&= \hbar^2 S(S+1)\left(e^{-a\hbar}-1\right)\Omega(a)+ \qquad (A.53)\\
&+ \hbar\left(e^{-a\hbar}+1\right)\frac{d}{da}\Omega(a)-\left(e^{-a\hbar}-1\right)\frac{d^2}{da^2}\Omega(a). \qquad (A.54)
\end{aligned}$$

With (A.51) its possible to write (A.40) as a function of $\Omega(a)$:

$$\begin{aligned}
\overline{p}(a) &= \langle e^{aS^z}S^-S^+\rangle \qquad (A.55)\\
&= \hbar^2 S(S+1)\Omega(a)-\hbar\frac{d}{da}\Omega(a)-\frac{d^2}{da^2}\Omega(a)=\eta(a)\varphi \qquad (A.56)
\end{aligned}$$

Using (A.54) we can set up a differential equation for $\Omega(a)$:

$$\begin{aligned}
&\left[-\left(e^{-a\hbar}-1\right)\varphi+1\right]\frac{d^2}{da^2}\Omega(a)+\left[\hbar\left(e^{-a\hbar}+1\right)\varphi+\hbar\right]\frac{d}{da}\Omega(a)+ \\
&\qquad+\left[\hbar^2 S(S+1)\left(e^{-a\hbar}-1\right)\varphi-\hbar^2 S(S+1)\right]\Omega(a)=0 \qquad (A.57)
\end{aligned}$$

$$\Rightarrow \quad \frac{d^2}{da^2}\Omega(a) - \hbar\frac{\left(e^{-a\hbar}+1\right)\varphi+1}{\left(e^{-a\hbar}-1\right)\varphi-1} - \hbar^2 S(S+1)\Omega(a) = 0. \qquad (A.58)$$

The solution of this differential equation of second order requires two limiting conditions. One follows directly from the definition (A.42)

$$\Omega(0)=1. \qquad (A.59)$$

With $S^z=-\hbar S,\ldots,\hbar S$ we obtain the second condition

$$\prod_{m_s=-S}^{+S}(S^z-\hbar m_S)=0 \Rightarrow \prod_{m_s=-S}^{+S}\left(\frac{d}{da}-\hbar m_S\right)\Omega(a)\Big|_{a=0}=0. \qquad (A.60)$$

Having the limiting conditions (A.59) and (A.60) we finally derive the solution (see e.g. [56]):

$$\Omega(a)=\frac{\varphi^{2S+1}e^{-a\hbar S}-(1+\varphi)^{2S+1}e^{\hbar(S+1)a}}{(\varphi^{2S+1}-(1+\varphi)^{2S+1})((1+\varphi)e^{\hbar a}-\varphi)}. \qquad (A.61)$$

We now obtain the desired expectation value $\langle S^z\rangle$

$$\langle S^z\rangle=\frac{d}{da}\Omega(a)\Big|_{a=0}=\frac{(1+\varphi)^{2S+1}(S-\varphi)+\varphi^{2S+1}(S+1+\varphi)}{(1+\varphi)^{2S+1}-\varphi^{2S+1}}, \qquad (A.62)$$

with

$$\varphi = \frac{1}{N}\sum_{\boldsymbol{q}} \frac{1}{e^{\beta E(\boldsymbol{q})}-1}. \tag{A.63}$$

A.3 Random Phase Approximation for Noncollinear Magnets

A.3.1 Magnetization and Néel temperature

In analogy to the ferromagnetic case we set up the equation of motion for the Green's function G_{ij}^{+-}, but now in the locally rotated coordinate system Σ'. Therefore, the following commutators have to be solved for the higher order Green's functions:

$$\begin{aligned}\left[S_m^{+\prime},\mathcal{H}'\right]_- = -\hbar\sum_j \{&K_{jm}(S_m^{z\prime}S_j^{x\prime}+S_j^{x\prime}S_m^{z\prime}) + iL_{jm}(S_m^{z\prime}S_j^{y\prime}+S_j^{y\prime}S_m^{z\prime})\\ &- M_{jm}(S_m^{+\prime}S_j^{z\prime}+S_j^{z\prime}S_m^{+\prime}) - 2\sum_j N_{jm}(-S_j^{x\prime}S_m^{+\prime}+S_m^{z\prime}S_j^{z\prime})\}.\end{aligned} \tag{A.64}$$

Applying the random phase approximation (RPA)

$$\left[S_m^{+\prime},\mathcal{H}'\right]_- \overset{\text{RPA}}{\longrightarrow} -2\hbar\langle S^z\rangle\sum_j\left\{K_{jm}S_j^{x\prime}+iL_{jm}S_j^{y\prime}-M_{jm}S_m^{+\prime}\right\} \tag{A.65}$$

$$= -\hbar\langle S^z\rangle\sum_j\left\{K_{jm}(S_j^{+\prime}+S_j^{-\prime})+L_{jm}(S_j^{+\prime}-S_j^{-\prime})-2M_{jm}S_m^{+\prime}\right\}. \tag{A.66}$$

Analogously one obtains:

$$\left[S_m^{-\prime},\mathcal{H}'\right]_- \overset{\text{RPA}}{\longrightarrow} -\hbar\langle S^z\rangle\sum_j\left\{-K_{jm}(S_j^{+\prime}+S_j^{-\prime})+L_{jm}(S_j^{+\prime}-S_j^{-\prime})+2M_{jm}S_m^{-\prime}\right\}. \tag{A.67}$$

Equation of Motion: Writing down the equation of motion for Green's functions G_{ij}^{+-} and G_{ij}^{-+}, and employing a Fourier transformation, e.g. $\frac{1}{N}\sum_i e^{i\boldsymbol{q}\boldsymbol{R}_i}S_{i+'} = S_{\boldsymbol{q}}^{+\prime}$, one ends up with the following coupled system of equations:

$$\frac{1}{\hbar}\begin{pmatrix} G_{\boldsymbol{q}}^{+-} & G_{\boldsymbol{q}}^{--}\\ G_{\boldsymbol{q}}^{++} & G_{\boldsymbol{q}}^{-+}\end{pmatrix} = \begin{pmatrix} 2\langle S^{z\prime}\rangle & 0\\ 0 & -2\langle S^{z\prime}\rangle\end{pmatrix}\left(E\underline{\underline{I}}-\underline{\underline{\Omega}}\right)^{-1}, \tag{A.68}$$

where the excitation energies of the system are determined by the eigenvalues of the matrix

$$\underline{\underline{\Omega}}(\boldsymbol{q}) = \langle S^{z'}\rangle\begin{pmatrix} 2M_{\mathbf{o}}-K_{\boldsymbol{q}}-L_{\boldsymbol{q}} & K_{\boldsymbol{q}}-L_{\boldsymbol{q}}\\ -(K_{\boldsymbol{q}}-L_{\boldsymbol{q}}) & -(2M_{\mathbf{o}}-K_{\boldsymbol{q}}-L_{\boldsymbol{q}})\end{pmatrix} = \begin{pmatrix} A & B\\ -B & -A\end{pmatrix}, \tag{A.69}$$

and explicitly given by

$$E_{\boldsymbol{q}\pm} = \pm 2\hbar\langle S^{z'}\rangle\sqrt{(M_{\mathbf{o}}-K_{\boldsymbol{q}})\,(M_{\mathbf{o}}-L_{\boldsymbol{q}})} \equiv E_{\pm}. \tag{A.70}$$

Here, the exchange coefficients are given by

$$K_{\boldsymbol{q}} = M_{\boldsymbol{q}} = \frac{1}{2}\left(J_{\boldsymbol{q}+\boldsymbol{Q}} + J_{\boldsymbol{q}-\boldsymbol{Q}}\right) \tag{A.71}$$

and

$$L_{\boldsymbol{q}} = J_{\boldsymbol{q}}. \tag{A.72}$$

Magnetization and critical temperature:
The magnon excitation energies and corresponding weights directly determine the effective magnon occupation number φ [56], given by

$$\varphi(T) = \frac{1}{N}\sum_{\boldsymbol{q}} \frac{\chi_{\boldsymbol{q}+}}{e^{\beta E_{\boldsymbol{q}+}} - 1} + \frac{\chi_{\boldsymbol{q}-}}{e^{\beta E_{\boldsymbol{q}-}} - 1}, \tag{A.73}$$

where the first term describes magnon creation and the second magnon annihilation, respectively. The weights $\chi_{\boldsymbol{q}+}$ are determined by the eigenvectors of (A.69) and given by

$$\chi_{\boldsymbol{q}\pm} = \frac{1}{2}\left(1 \pm \frac{a}{b}\right), \tag{A.74}$$

with

$$a := M_{\mathbf{o}} - 1/2K_{\boldsymbol{q}} - 1/2L_{\boldsymbol{q}} \tag{A.75}$$

$$b := \sqrt{(M_{\mathbf{o}} - K_{\boldsymbol{q}})(M_{\mathbf{o}} - L_{\boldsymbol{q}})}. \tag{A.76}$$

Eq. (A.73) can be rewritten as

$$\varphi(T) = \frac{1}{2}\frac{1}{N}\sum_{\boldsymbol{q}} \left(\frac{a}{b}\coth\left[1/2\beta E_{\boldsymbol{q}}\right] - 1\right), \tag{A.77}$$

which turns out to be faster and more efficient for numerical evaluation. The magnetization for the general spin system ($S \geq 1/2$) is given by

$$\langle S^{z\prime}\rangle = \frac{(1+\varphi)^{2S+1}(S-\varphi) + \varphi^{2S+1}(S+1+\varphi)}{(1+\varphi)^{2S+1} - \varphi^{2S+1}}, \tag{A.78}$$

with φ as defined in (A.73).
For $S = 1/2$ above equation simplifies to

$$\langle S^{z\prime}\rangle = \frac{S}{1+2\varphi}. \tag{A.79}$$

Critical temperature:
For $T \to T_{\mathrm{crit}}$, the magnetization vanishes and $\varphi \to \infty$. Hence we can expand the right-hand site of Eq. (A.78) in terms of $\mathcal{O}(\varphi^{-n})$ and obtain:

$$\begin{aligned}
\langle S^z \rangle &= \frac{1}{3} S(S+1)\varphi^{-1} + \mathcal{O}(\varphi^{-2}) && \text{(A.80)}\\
&\overset{\langle S_z\rangle \to 0}{\longrightarrow} \frac{1}{3} S(S+1) \left(\sum_{\boldsymbol{q}} \frac{1}{\beta 4 \langle S^z \rangle} \left[\frac{1}{M_{\mathbf{o}} - K_{\boldsymbol{q}}} + \frac{1}{M_{\mathbf{o}} - L_{\boldsymbol{q}}} \right] \right)^{-1} && \text{(A.81)}\\
\Rightarrow k_B T_{\mathrm{crit}} &= \frac{4}{3} S(S+1) \left(\sum_{\boldsymbol{q}} \left[\frac{1}{M_{\mathbf{o}} - K_{\boldsymbol{q}}} + \frac{1}{M_{\mathbf{o}} - L_{\boldsymbol{q}}} \right] \right)^{-1} && \text{(A.82)}\\
&= \frac{4}{3} \left(\sum_{\boldsymbol{q}} \left[\frac{1}{\tilde{M}_{\mathbf{o}} - \tilde{K}_{\boldsymbol{q}}} + \frac{1}{\tilde{M}_{\mathbf{o}} - \tilde{L}_{\boldsymbol{q}}} \right] \right)^{-1}, && \text{(A.83)}
\end{aligned}$$

which corresponds to the Néel temperature T_N employed in Ref. [140, 141]. In the last step we have absorbed the factor $S(S+1)$ into the exchange constants.

A.3.2 Internal energy

To derive the internal energy we use, similar as for the ferromagnetic case, exact $S = 1/2$ relations. In the first step we rewrite the Hamiltonian (2.70) in terms of correlation functions, which we access by the Green's function matrix Eq. (A.68).
From Eq. (A.68) we obtain:

$$\frac{1}{\hbar} \begin{pmatrix} G^{+-}_{\boldsymbol{q}} & G^{--}_{\boldsymbol{q}} \\ G^{++}_{\boldsymbol{q}} & G^{-+}_{\boldsymbol{q}} \end{pmatrix} \begin{pmatrix} E - A & -B \\ +B & E + A \end{pmatrix} = \begin{pmatrix} 2\langle S^{z\prime} \rangle & 0 \\ 0 & -2\langle S^{z\prime} \rangle \end{pmatrix} \tag{A.84}$$

Yielding:

$$\begin{aligned}
G^{+-}_{\boldsymbol{q}} &= \frac{E + A}{E^2 - (A^2 - B^2)} 2\langle S^z \rangle = \frac{E + A}{(E - E_+)(E + E_+)} 2\langle S^z \rangle && \text{(A.85)}\\
&= 2\langle S^z \rangle \left(\frac{1/2[1 + A/E_+]}{E - E_+} + \frac{1/2[1 - A/E_+]}{E + E_+} \right) && \text{(A.86)}
\end{aligned}$$

From the matrix solution (e.g. first row times second column) we obtain:

$$G^{+-}_{\boldsymbol{q}} B = (E + A) G^{--}_{\boldsymbol{q}} \tag{A.87}$$

and with (A.85):

$$G^{--}_{\boldsymbol{q}} = 2\langle S^z \rangle \frac{B}{2E_+} \left(-\frac{1}{E - E_+} + \frac{1}{E + E_+} \right) \tag{A.88}$$

and

$$G^{++}_{\boldsymbol{q}} = -2\langle S^z \rangle \frac{B}{2E_+} \left(-\frac{1}{E - E_+} + \frac{1}{E + E_+} \right). \tag{A.89}$$

The internal energy

In order to rewrite the internal energy in terms of the correlation functions $\langle S_{i\pm} S_{j\pm}\rangle$, we replace all operators S_{ik} $(k = x, y, z)$ in the Hamiltonian Eq. (3.29),

$$\mathcal{H}' = -\sum_{ij}\left(K_{ij}S'_{ix}S'_{jx} + L_{ij}S'_{iy}S'_{jy} + M_{ij}S'_{iz}S'_{jz}\right) + 2\sum_{ij} N_{ij}S'_{ix}S'_{jz}, \tag{A.90}$$

by creation and annihilation operators:

$$\mathcal{H} = -\sum_{ij}\{1/4(K_{ij} - J_{ij})S_i^{+\prime}S_j^{+\prime} + 1/4(K_{ij} - J_{ij})S_i^{-\prime}S_j^{-\prime} + 1/2(K_{ij} + J_{ij})S_i^{+\prime}S_j^{-\prime} + \\ + K_{ij}S_i^{z\prime}S_j^{z\prime} - N_{ij}S_i^{+\prime}S_j^{z\prime} - N_{ij}S_i^{-\prime}S_j^{z\prime}\}. \tag{A.91}$$

Please be aware of the definitions of the N, K, J, i.e.

$$J_{ij} = J_{ji} \qquad K_{ij} = \cos(\phi_i - \phi_j)J_{ij} = K_{ji} \qquad \underline{N_{ij} = \sin(\phi_i - \phi_j)J_{ij} = -N_{ji}}. \tag{A.92}$$

For $S = 1/2$, the longitudinal correlation function can be expressed in terms of the transversal correlation function:

$$S_i^{-\prime}\left[S_i^{+\prime}, \mathcal{H}\right]_- = -\sum_{m}\{1/2(K_{im} - J_{im})S_m^{-\prime}S_i^{-\prime} + 1/2(K_{im} + J_{im})S_m^{+\prime}S_i^{-\prime} - \\ 2K_{im}S_m^{z\prime}(S - S_i^{z\prime}) + N_{mi}S_m^{+\prime}(S - S_i^{z\prime}) + N_{mi}S_m^{-\prime}(S - S_i^{z\prime}) - N_{im}S_m^{z\prime}S_i^{-\prime}\} \tag{A.93}$$

and

$$-\sum_{im} K_{im}\langle S_m^{z\prime}S_i^{z\prime}\rangle = \frac{1}{2}\sum_i \langle S_i^{-\prime}\left[S_i^{+\prime}, \mathcal{H}\right]_-\rangle + \sum_{im}\{1/4(K_{im} - J_{im})\langle S_m^{-\prime}S_i^{-\prime}\rangle + \\ + 1/4(K_{im} + J_{im})\langle S_m^{+\prime}S_i^{-\prime}\rangle - K_{im}\langle S_m^{z\prime}\rangle S - 1/2N_{mi}\langle S_m^{+\prime}S_i^{z\prime}\rangle - N_{mi}\langle S_m^{-\prime}S_i^{z\prime}\rangle\}. \tag{A.94}$$

Inserting above relation into $\mathcal{U} = \langle\mathcal{H}\rangle$, only the term $1/2\sum_{im} N_{mi}\langle S_m^{+\prime}S_i^{z\prime}\rangle$ remains unknown. We derive the missing correlation function using

$$S_i^{+\prime}\left[S_i^{+\prime}, \mathcal{H}\right]_- = -\sum_{m}\{-1/2(K_{im} - J_{im})S_m^{-\prime}S_i^{+\prime} - 1/2(K_{im} + J_{im})S_m^{+\prime}S_i^{+\prime} + N_{im}S_m^{z\prime}S_i^{+\prime}\}. \tag{A.95}$$

and obtain (please be aware of $N_{ij} = -N_{ji}$)

$$1/2\sum_{im} N_{mi}\langle S_m^{+\prime}S_i^{z\prime}\rangle = -1/2\sum_i \langle S_i^{+\prime}\left[S_i^{+\prime}, \mathcal{H}\right]_-\rangle + \\ \sum_{im}\{1/4(K_{im} - J_{im})\langle S_m^{-\prime}S_i^{+\prime}\rangle + 1/4(K_{im} + J_{im})\langle S_m^{+\prime}S_i^{+\prime}\rangle\}. \tag{A.96}$$

Now we are able to express the internal energy purely in terms of the correlation functions $\langle S^{\pm\prime} S^{\pm\prime}\rangle$ and $\langle S^{\pm\prime} S^{\mp\prime}\rangle$:

$$\begin{aligned}
U = \langle\mathcal{H}\rangle \quad &= \quad \sum_{ij} -1/4(K_{ij} - J_{ij})\langle S_i^{+\prime} S_j^{+\prime}\rangle - 1/4(K_{ij} - J_{ij})\langle S_i^{-\prime} S_j^{-\prime}\rangle - \\
&- \quad 1/2(K_{ij} + J_{ij})\langle S_i^{+\prime} S_j^{-\prime}\rangle - K_{ij}\langle S_i^{z\prime} S_j^{z\prime}\rangle + N_{ij}\langle S_i^{+\prime} S_j^{z\prime}\rangle + N_{ij}\langle S_i^{-\prime} S_j^{z\prime}\rangle \\
&\overset{(A.94)}{=} \quad \frac{1}{2}\sum_i \langle S_i^{-\prime}\left[S_i^{+\prime}, \mathcal{H}\right]_-\rangle + \sum_{ij}\{-1/4(K_{ij} + J_{ij})\langle S_j^{+\prime} S_i^{-\prime}\rangle - K_{ij}\langle S_j^{z\prime}\rangle S + \\
&+ \quad \sum_{ij} -1/4(K_{ij} - J_{ij})\langle S_i^{+\prime} S_j^{+\prime}\rangle + 1/2 N_{ij}\langle S_i^{+\prime} S_j^{z\prime}\rangle \\
&\overset{(A.96)}{=} \quad \frac{1}{2}\sum_i \langle S_i^{-\prime}\left[S_i^{+\prime}, \mathcal{H}\right]_-\rangle + \sum_{ij}\{-1/4(K_{ij} + J_{ij})\langle S_j^{+\prime} S_i^{-\prime}\rangle - K_{ij}\langle S_j^{z\prime}\rangle S + \\
&+ \quad \sum_{ij} -1/4(K_{ij} - J_{ij})\langle S_i^{+\prime} S_j^{+\prime}\rangle - 1/2\sum_i \langle S_i^{+\prime}\left[S_i^{+\prime}, \mathcal{H}\right]_-\rangle + \\
&+ \quad \sum_{ij}\{1/4(K_{ij} - J_{ij})\langle S_j^{-\prime} S_i^{+\prime}\rangle + 1/4(K_{ij} + J_{ij})\langle S_j^{+\prime} S_i^{+\prime}\rangle\} \\
&= \quad \frac{1}{2}\sum_i \langle S_i^{-\prime}\left[S_i^{+\prime}, \mathcal{H}\right]_-\rangle - \frac{1}{2}\sum_i \langle S_i^{+\prime}\left[S_i^{+\prime}, \mathcal{H}\right]_-\rangle + \sum_{ij} -K_{ij}\langle S_j^{z\prime}\rangle S + \\
&+ \quad 1/2 J_{ij}\langle S_i^{+\prime} S_j^{+\prime}\rangle - 1/2 J_{ij}\langle S_i^{+\prime} S_j^{-\prime}\rangle.
\end{aligned}$$

With $\langle S_i^{z\prime}\rangle = \langle S - S_i^{-\prime} S_i^{+\prime}\rangle$, and using $S = 1/2$, we finally end up with:

$$U = \langle\mathcal{H}\rangle = \frac{1}{2}\sum_i \langle S_i^{-\prime}\left[S_i^{+\prime}, \mathcal{H}\right]_-\rangle - \frac{1}{2}\sum_i \langle S_i^{+\prime}\left[S_i^{+\prime}, \mathcal{H}\right]_-\rangle + \frac{1}{2}\sum_{ij} J_{ij}\langle S_i^{+\prime} S_j^{+\prime}\rangle + E_0 + \frac{1}{2}\sum_{ij}(K_0\delta_{ij} - J_{ij})\langle S_j^{-\prime} S_i^{+\prime}\rangle, \quad \text{(A.97)}$$

where the ground-state energy E_0 is defined as

$$E_0 = -K_0 S^2. \quad \text{(A.98)}$$

To compute terms such as $\frac{1}{2}\sum_i \langle S_i^{-\prime}\left[S_i^{+\prime}, \mathcal{H}\right]_-\rangle$, we employ that for the non time-dependent Hamilton operator $\mathcal{H}$ the derivative $S_i^{+\prime}(t)$ can be written as:

$$i\frac{\partial}{\partial t} S_i^{+\prime}(t) = \left[S_i^{+\prime}, \mathcal{H}\right]_-(t). \quad \text{(A.99)}$$

Using above, the first term on the right-hand site of Eq. (A.97) can be reformulated as (see e.g. Ref. [28]):

$$\frac{1}{2}\sum_i \langle S_i^{-\prime}\left[S_i^{+\prime},\mathcal{H}\right]_-\rangle = \frac{i}{2}\sum_i\left(\frac{\partial}{\partial t}\int_{-\infty}^{+\infty} dE \frac{S_{\boldsymbol{q}}^{+-}(E)}{e^{\beta E}-1}\exp\left(-iE(t-t')\right)\right)_{t=t'} \tag{A.100}$$

$$= \frac{1}{2}\sum_{\boldsymbol{q}}\int_{-\infty}^{+\infty} dE \frac{E S_{\boldsymbol{q}}^{+-}(E)}{e^{\beta E}-1}. \tag{A.101}$$

Analogously one obtains

$$-\frac{1}{2}\sum_i \langle S_i^{+\prime}\left[S_i^{+\prime},\mathcal{H}\right]_-\rangle = -\frac{1}{2}\sum_{\boldsymbol{q}}\int_{-\infty}^{+\infty} dE \frac{E S_{\boldsymbol{q}}^{++}(E)}{e^{\beta E}-1} \tag{A.102}$$

and finally an expression for the internal energy of the noncollinear magnet as:

$$U = U_0 + \frac{1}{2}\sum_{\boldsymbol{q}}\int_{-\infty}^{+\infty} dE\left(\frac{E+2S(K_{\mathbf{o}}-J_{\boldsymbol{q}})}{e^{\beta E}-1}S_{\boldsymbol{q}}^{+-}(E) + \frac{E-2SJ_{\boldsymbol{q}}}{e^{\beta E}-1}S_{\boldsymbol{q}}^{++}(E)\right). \tag{A.103}$$

The spectral densities are given as

$$S_{\boldsymbol{q}}^{+-}(E) = 2\langle S^{z\prime}\rangle\left(\chi_1^{+-}\delta(E-E_+)+\chi_2^{+-}\delta(E+E_+)\right), \tag{A.104}$$

$$S_{\boldsymbol{q}}^{++}(E) = 2\langle S^{z\prime}\rangle\left(\chi_1^{++}\delta(E-E_+)+\chi_2^{++}\delta(E+E_+)\right), \tag{A.105}$$

with

$$\chi_{1,2}^{+-} = \frac{1}{2}\left(1 \pm \frac{K_{\mathbf{o}}-1/2K_{\boldsymbol{q}}-1/2J_{\boldsymbol{q}}}{\sqrt{(K_{\mathbf{o}}-K_{\boldsymbol{q}})(K_{\mathbf{o}}-J_{\boldsymbol{q}})}}\right), \tag{A.106}$$

$$\chi_{1,2}^{++} = \pm\frac{1}{2}\frac{1/2K_{\boldsymbol{q}}-1/2J_{\boldsymbol{q}}}{\sqrt{(K_{\mathbf{o}}-K_{\boldsymbol{q}})(K_{\mathbf{o}}-J_{\boldsymbol{q}})}}, \tag{A.107}$$

$$E_+ = 2\langle S^{z\prime}\rangle\sqrt{(K_{\mathbf{o}}-K_{\boldsymbol{q}})(K_{\mathbf{o}}-J_{\boldsymbol{q}})}. \tag{A.108}$$

For the ferromagnetic solution, i.e. $Q=(0,0,0)$, Eq. (A.103) transforms into the known ferromagnetic solution [28].

Bibliography

[1] Ironware piece unearthed from turkey found to be oldest steel, The Hindu Newspaper, March 26, 2009.

[2] U.S. Geological Survey, 2009, Iron and Steel statistics, in Kelly, T.D., and Matos, G.R., Historical statistics for mineral and material commodities in the United States: U.S. Geological Survey Data Series 140, available online at http://pubs.usgs.gov/ds/2005/140/.

[3] Prof. Dr.-Ing. Dieter Ameling, Präsident Wirtschaftsvereinigung Stahl, Vorsitzender Stahlinstitut VDEh, Talk, 2007.

[4] T.Chandra, N.Wanderka, W.Reimers, and M.Ionescu, Materials Science Forum **638**, 3134 (2010).

[5] B. Grabowski, PhD thesis, University of Paderborn, 2009.

[6] X. Sha and R. E. Cohen, Phys. Rev. B **73**, 104303 (2006).

[7] L. Kaufman, E. V. Clougherty, and R. J. Weiss, Acta Metal. **11**, 323 (1963).

[8] H. Hasegawa and D. G. Pettifor, Phys. Rev. Lett. **50**, 130 (1983).

[9] U. von Barth and L. Hedin, Journal of Physics C: Solid State Physics **5**, 1629 (1972).

[10] K. Capelle, Braz. J. Phys. **36**, 1318 (2006).

[11] W. Heisenberg, Zeitschrift für Physik **38**, 411 (1926).

[12] S. V. Halilov, A. Y. Perlov, P. M. Oppeneer, and H. Eschrig, Europhys. Lett. **39**, 91 (1997).

[13] J. Rusz, L. Bergqvist, J. Kudrnovský, and I. Turek, Phys. Rev. B **73**, 214412 (2006).

[14] G. Y. Gao, K. L. Yao, E. Şaşioğlu, L. M. Sandratskii, Z. L. Liu, and J. L. Jiang, Phys. Rev. B **75**, 174442 (2007).

[15] M. Pajda, J. Kudrnovsky, I. Turek, V. Drchal, and P. Bruno, Phys. Rev. B **64**, 174402 (2001).

[16] F. Körmann, A. Dick, B. Grabowski, B. Hallstedt, T. Hickel, and J. Neugebauer, Phys. Rev. B **78**, 033102 (2008).

[17] F. Körmann, A. Dick, T. Hickel, and J. Neugebauer, Phys. Rev. B **79**, 184406 (2009).

[18] N. Bogolyubov and S. Tyablikov, Soviet. Phys.-Doklady **4** (1959).

[19] M. Marsman and J. Hafner, Phys. Rev. B **66**, 224409 (2002).

[20] R. G. Parr and W. Yang, *Density-Functional Theory of Atoms and Molecules*, Oxford Science Publications, 1988.

[21] K. Capelle and G. Vignale, Phys. Rev. Lett. **86**, 5546 (2001).

[22] H. Eschrig and W. E. Pickett, Solid State Communications **118**, 123 (2001).

[23] N. Argaman and G. Makov, Phys. Rev. B **66**, 052413 (2002).

[24] N. I. Gidopoulos, Phys. Rev. B **75**, 134408 (2007).

[25] W. Kohn, A. Savin, and C. A. Ullrich, International Journal of Quantum Chemistry **101**, 20 (2004).

[26] K. Capelle, C. A. Ullrich, and G. Vignale, Phys. Rev. A **76**, 012508 (2007).

[27] T. Gál, P. W. Ayers, F. D. Proft, and P. Geerlings, J. Chem. Phys. **131**, 154114 (2009).

[28] W. Nolting, *Fundamentals of Many-body Physics*, Springer, 2009.

[29] W. Kohn and L. J. Sham, Phys. Rev. **140**, A1133 (1965).

[30] L. M. Sandratskii and P. G. Guletskii, Journal of Physics F: Metal Physics **16**, L43 (1986).

[31] J. Kübler, *Theory of Itinerant Electron Magnetism*, Oxford University Press, 2009.

[32] J. P. Perdew and A. Zunger, Phys. Rev. B **23**, 5048 (1981).

[33] D. M. Ceperley and B. J. Alder, Phys. Rev. Lett. **45**, 566 (1980).

[34] C. S. Wang, B. M. Klein, and H. Krakauer, Phys. Rev. Lett. **54**, 1852 (1985).

[35] M. C. Payne, M. P. Teter, D. C. Allan, T. A. Arias, and J. D. Joannopoulos, Rev. Mod. Phys. **64**, 1045 (1992).

[36] D. E. Eastman, F. J. Himpsel, and J. A. Knapp, Phys. Rev. Lett. **44**, 95 (1980).

[37] S. Y. Savrasov, Phys. Rev. Lett. **81**, 2570 (1998).

[38] E. Runge and E. K. U. Gross, Phys. Rev. Lett. **52**, 997 (1984).

[39] E. Şaşıoğlu, A. Schindlmayr, C. Friedrich, F. Freimuth, and S. Blügel, Phys. Rev. B **81**, 054434 (2010).

[40] G. Onida, L. Reining, and A. Rubio, Rev. Mod. Phys. **74**, 601 (2002).

[41] W. Nolting, *Grundkurs Theoretische Physik 7*, Springer-Verlag, Berlin, 2005.

[42] L. Hedin, Phys. Rev. **139**, A796 (1965).

[43] N. M. Rosengaard and B. Johansson, Phys. Rev. B **55**, 14975 (1997).

[44] J. Kübler, J. Phys.: Condens. Matter **18**, 9795 (2006).

[45] L. Landau and E. Lifshitz, Phys. Z. Sowietunion **8**, 153 (1935).

[46] S. Shallcross, A. E. Kissavos, V. Meded, and A. V. Ruban, Phys. Rev. B **72**, 104437 (2005).

[47] A. V. Ruban, S. Shallcross, S. I. Simak, and H. L. Skriver, Phys. Rev. B **70**, 125115 (2004).

[48] A. V. Ruban, S. Khmelevskyi, P. Mohn, and B. Johansson, Phys. Rev. B **75**, 054402 (2007).

[49] L. M. Sandratskii, Advances In Physics **47**, 91 (1998).

[50] J. Hubbard, J. Hubbard, Proc. R. Soc. London, Ser. A 276, 238 (1963) **Ser. A 276**, 238 (1963).

[51] M. C. Gutzwiller, Phys. Rev. Lett. **10**, 159 (1963).

[52] J. Kanamori, Prog. Theor. Phys. **30**, 275 (1963).

[53] C. Santos and W. Nolting, Phys. Rev. B **65**, 144419 (2002).

[54] M. Ležaić, P. Mavropoulos, and S. Blügel, Appl. Phys. Lett. **90**, 082504 (2007).

[55] N. D. Mermin and H. Wagner, Phys. Rev. Lett. **17**, 1133 (1966).

[56] W. Nolting, *Quantentheorie des Magnetismus, Teil 2, Modelle*, Teubner Verlag, 1997.

[57] M. Exler, *On Classical and Quantum Mechanical Energy Spectra of Finite Heisenberg Spin Systems*, PhD thesis, University Osnabrück, 2006, URN: urn:nbn:de:gbv:700-2006051610.

[58] F. Körmann, A. Dick, T. Hickel., and J. Neugebauer, Phys. Rev. B **81**, 134425 (2010).

[59] J. Oitmaa and W. Zheng, Journal of Physics: Condensed Matter **16**, 8653 (2004).

[60] J. Thoene, S. Chadov, G. Fecher, C. Felser, and J. Kübler, Journal of Physics D: Applied Physics **42**, 084013 (2009).

[61] H. Callen, Phys. Rev. **130**, 890 (1963).

[62] S. H. Liu, Phys. Rev. **139**, A1522 (1965).

[63] S. Tjablikov, *Methods in the Quantum Theory of Magnetism,*, Plenum Press, New York, 1967.

[64] J.-B. Fouet, A. Läuchli, S. Pilgram, R. M. Noack, and F. Mila, Phys. Rev. B **73**, 014409 (2006).

[65] T. Fabritius, N. Laflorencie, and S. Wessel, Phys. Rev. B **82**, 035402 (2010).

[66] N. V. Prokof'ev, B. V. Svistunov, and I. S. Tupitsyn, Physics Letters A **238**, 253 (1998).

[67] H. G. Evertz, Adv. Phys. **1**, 1 (2003).

[68] O. F. Syljuåsen and A. W. Sandvik, Phys. Rev. E **66**, 046701 (2002).

[69] A. W. Sandvik and J. Kurkijärvi, Phys. Rev. B **43**, 5950 (1991).

[70] M. Troyer, S. Wessel, and F. Alet, Phys. Rev. Lett. **90**, 120201 (2003).

[71] F. Wang and D. P. Landau, Phys. Rev. Lett. **86**, 2050 (2001).

[72] A. Albuquerque et al., J. Magn. Magn. Mater. **310**, 1187 (2007).

[73] P. Henelius and A. W. Sandvik, Phys. Rev. B **62**, 1102 (2000).

[74] E. Y. Loh, J. E. Gubernatis, R. T. Scalettar, S. R. White, D. J. Scalapino, and R. L. Sugar, Phys. Rev. B **41**, 9301 (1990).

[75] K. Siemensmeyer, K. Habicht, T. Lonkai, S. Mat'as, S. Gabï£¡ni, N. Shitsevalova, E. Wulf, and K. Flachbart, J. Low Temp. Phys. **146**, 581 (2007).

[76] M. Troyer and U.-J. Wiese, Phys. Rev. Lett. **94**, 170201 (2005).

[77] F. D. Murnaghan, Proc. Natl. Acad. Sci. U.S.A. **30**, 244 (1944).

[78] N. D. Mermin, Phys. Rev. **137**, A1441 (1965).

[79] W. Nolting, *Grundkurs Theoretische Physik 6*, Springer-Verlag, Berlin, 2005.

[80] B. Grabowski, T. Hickel, and J. Neugebauer, Phys. Rev. B **76**, 024309 (2007).

[81] B. Grabowski, L. Ismer, T. Hickel, and J. Neugebauer, Phys. Rev. B **79**, 134106 (2009).

[82] J. Harris, R. O. Jones, and J. E. Mï£¡ller, J. Chem. Phys. **75**, 3904 (1981).

[83] S. Baroni, S. de Gironcoli, A. Dal Corso, and P. Giannozzi, Rev. Mod. Phys. **73**, 515 (2001).

[84] S. Boeck *et al.*, *The* S/PHI/NX *package, http://www.sphinxlib.de/.*

[85] V. Heine, A. I. Liechtenstein, and O. N. Mryasov, EPL (Europhysics Letters) **12**, 545 (1990).

[86] L. Kaufman and H. Bernstein, *Computer Calculation of Phase Diagrams*, Academic, New York, 1970.

[87] N. Saunders and A. P. Miodownik, *Calphad (Calculation of Phase Diagrams): A Comprehensive Guide*, Pergamon, Oxford, 1998.

[88] J. M. Leger, C. Loriers-Susse, and B. Vodar, Phys. Rev. B **6**, 4250 (1972).

[89] S. Morán, C. Ederer, and M. Fähnle, Phys. Rev. B **67**, 012407 (2003).

[90] E. Şaşıoğlu, L. M. Sandratskii, and P. Bruno, Phys. Rev. B **71**, 214412 (2005).

[91] L. Bergqvist, B. Belhadji, S. Picozzi, and P. H. Dederichs, Phys. Rev. B **77**, 014418 (2008).

[92] G. Kresse and J. Furthmüller, Phys. Rev. B **54**, 11169 (1996).

[93] G. Kresse and J. Hafner, Phys. Rev. B **47**, 558 (1993).

[94] P. E. Blöchl, Phys. Rev. B **50**, 17 953 (1994).

[95] J. P. Perdew, K. Burke, and M. Ernzerhof, Phys. Rev. Lett. **77**, 3865 (1996).

[96] J. Zhang and F. Guyot, Phys. Chem. Miner. **26**, 206 (1999).

[97] O. Grotheer, C. Ederer, and M. Fähnle, Phys. Rev. B **63**, 100401 (2001).

[98] C. Loong, J. Carpenter, J. Lynn, R. Robinson, and H. Mook, J. Appl. Phys. **55**, 1895 (1984).

[99] J. Lynn, Phys. Rev. B **11**, 2624 (1974).

[100] J. Crangle and G. M. Goodman, Proceedings of the Royal Society of London, Series A, Mathematical and Physical Sciences **321**, 477 (1971).

[101] F. M. Wang and R. Ingalls, Phys. Rev. B **57**, 5647 (1998).

[102] D. C. Wallace, *Thermodynamics of Crystals*, Dover, New York, 1998.

[103] R. F. Sabiryanov and S. S. Jaswal, Phys. Rev. Lett. **83**, 2062 (1999).

[104] Landolt-Börnstein, editor, *Metals: Phonon States, Electron States and Fermi Surfaces*, volume 13, Springer-Verlag, Berlin, 1981, New Series, Group III.

[105] A. F. Guillemet and P. Gustafson, High Temp. High Press. **16**, 591 (1985).

[106] D. C. Wallace, P. H. Sidles, and G. C. Danielson, J. Appl. Phys. **31**, 168 (1960).

[107] Y. S. Touloukian, R. K. Kirby, R. E. Taylor, and P. D. Desai, *Thermophysical Properties of Matter*, volume 12, IFI/Plenum, New York, 1975.

[108] R. A. Tahir-Kheli, Phys. Rev. **159**, 439 (1967).

[109] J. A. Copeland and H. A. Gersch, Phys. Rev. **143**, 236 (1966).

[110] S. H. Liu and D. B. Siano, Phys. Rev. **164**, 697 (1967).

[111] M. D. Kuz'min, Phys. Rev. Lett. **94**, 107204 (2005).

[112] M. D. Kuz'min, M. Richter, and A. N. Yaresko, Phys. Rev. B **73**, 100401 (2006).

[113] M. E. J. Newman and G. T. Barkema, *Monte Carlo Methods in Statistical Physics*, Oxford University Press, USA, 1999.

[114] The critical temperature within the quantum case does not strictly follow $T_C(S) \sim JS(S+1) = \tilde{J}$ as was, e.g., recently shown using high temperature series expansion [J. Phys.: Condens. Matter **16**, 8653 (2004)]. The complex dependence of $T_C(S)$ is, however, beyond the scope of the present manuscript.

[115] The exclusions are $T_C(S)$ as discussed in the text and the integration constant $U^{\mathrm{QMC}}(0)$ for the internal energy, which cannot be determined solely from the heat capacity. To determine $U^{\mathrm{QMC}}(0)$ we use $U^{\mathrm{cMC}}(T_h) \equiv U^{\mathrm{QMC}}(T_h)$, which holds true for high temperatures T_h. For all considered systems the choice $T_h = 3T_C$ was in this respect sufficient.

[116] The nearest neighbor antiferromagnetic *fcc* lattice is known to be frustrated, see e.g. [J. Low Temp. Phys. **146**, 581 (2007)], and is therefore not considered in this study.

[117] By taking 10 shells into account the average sign $\langle\sigma\rangle_T$ decreases to 10^{-3} for temperatures below $2T_C$. To achieve statistical errors of less than 5%, the calculation time on a conventional computer is in the order of years for a single temperature calculation.

[118] If the heat capacity shows a finite cusp with a magnitude $C_P(T_C) = C_P^{\max}$, a finite size ansatz can be used to extrapolate the dependence $C_P^{\max}(L)$ on system size L. Depending on the finite size scaling fit, the system size required to obtain, e.g., 50% of $C_P^{\max}$ may result in system sizes containing up to 10^7 atoms (see e.g. Phys. Rev. B **42**, 6087 (1990)), which renders the problem to be computationally unfeasible.

[119] The CALPHAD data has been obtained with the THERMOCALC program and the SGTE unary database [105].

[120] R. J. Weiss and K. J. Tauer, Phys. Rev. **102**, 1490 (1956).

[121] H. C. Herper, E. Hoffmann, and P. Entel, Phys. Rev. B **60**, 3839 (1999).

[122] J. Zarestky and C. Stassis, Phys. Rev. B **35**, 4500 (1987).

[123] C. Engin, L. Sandoval, and H. M. Urbassek, Modelling and Simulation in Materials Science and Engineering **16**, 035005 (2008).

[124] H. C. Hsueh, J. Crain, G. Y. Guo, H. Y. Chen, C. C. Lee, K. P. Chang, and H. L. Shih, Phys. Rev. B **66**, 052420 (2002).

[125] M. Y. Lavrentiev, D. Nguyen-Manh, and S. L. Dudarev, Phys. Rev. B **81**, 184202 (2010).

[126] M. Lavrentiev, S. Dudarev, and D. Nguyen-Manh, Journal of Nuclear Materials **386**, 22 (2009).

[127] D. J. Dever, J. Appl. Phys. **43**, 3293 (1972).

[128] Y. Tsunoda and N. Kunitomi, Solid State Commun. **54**, 547 (1985).

[129] Y. Tsunoda and N. Kunitomi, J. Phys. F: Met. Phys. **18**, 1405 (1988).

[130] Y. Tsunoda, J. Phys.: Condens. Matter **3**, 7231 (1991).

[131] B. Jonker, K. Walker, E. Kisker, G. Prinz, and C. Carbone, Phys. Rev. Lett. **57**, 142 (1986).

[132] W. Macedo and W. Keune, Phys. Rev. Lett. **61**, 475 (1988).

[133] H. Magnan, D. Chandesris, B. Villette, O. Heckmann, and J. Lecante, Phys. Rev. Lett. **67**, 859 (1991).

[134] J. Thomassen, F. May, B. Feldmann, M. Wuttig, and H. Ibach, Phys. Rev. Lett. **69**, 3831 (1992).

[135] S. Müller, P. Bayer, C. Reischl, K. Heinz, B. Feldmann, H. Zillgen, and M. Wuttig, Phys. Rev. Lett. **74**, 765 (1995).

[136] R. Ellerbrock, A. Fuest, A. Schatz, W. Keune, and R. Brand, Phys. Rev. Lett. **74**, 3053 (1995).

[137] D. Keavney, D. Storm, J. Freeland, I. Grigorov, and J. Walker, Phys. Rev. Lett. **74**, 4531 (1995).

[138] M. Straub, R. Vollmer, and J. Kirschner, Phys. Rev. Lett. **77**, 743 (1996).

[139] Y. Tsunoda, N. Kunitomi, and R. M. Nicklow, Journal of Physics F: Metal Physics **17**, 2447 (1987).

[140] I. Turek, J. Kudrnovský, M. Diviš, P. Franek, G. Bihlmayer, and S. Blügel, Phys. Rev. B **68**, 224431 (2003).

[141] J. Kuneš and R. Laskowski, Phys. Rev. B **70**, 174415 (2004).

[142] W. Huang, Calphad **13**, 243 (1989).

[143] N. Singh, Phys. Status Solidi B **156**, K33 (1989).

[144] P. D. Desai, J. Phys. Chem. Ref. Data **15**, 967 (1986).

[145] Q. Chen and B. Sundman, J. Phase Equilib. **22**, 631 (2001).

[146] A. F. Guillemet, Int. J. Thermophys. **8**, 481 (1987).

[147] J. E. Saal, S. Shang, Y. Wang, and Z.-K. Liu, Journal of Physics: Condensed Matter **22**, 096006 (2010).

[148] P. Peczak, A. M. Ferrenberg, and D. P. Landau, Phys. Rev. B **43**, 6087 (1991).

[149] R. G. Brown and M. Ciftan, Phys. Rev. Lett. **78**, 2266 (1997).

[150] R. G. Brown and M. Ciftan, Phys. Rev. Lett. **76**, 1352 (1996).

[151] C. Holm and W. Janke, Phys. Rev. Lett. **78**, 2265 (1997).

[152] Landolt-Börnstein, editor, *Metals: Phonon States, Electron States and Fermi Surfaces*, volume 19a, Springer-Verlag, Berlin, 1981, New Series, Group III.

[153] B. Hallstedt, D. Djurovic, J. von Appen, R. Dronskowski, A. Dick, F. Körmann, T. Hickel, and J. Neugebauer, Calphad **34**, 129 (2010).

[154] A. Dick, F. Körmann, T. Hickel., and J. Neugebauer, submitted, 2011.

[155] C. M. Fang, M. H. F. Sluiter, M. A. van Huis, C. K. Ande, and H. W. Zandbergen, Phys. Rev. Lett. **105**, 055503 (2010).

[156] H. P. Scott, Q. Williams, and E. Knittle, Geophys. Res. Lett. **28**, 1875 (2001).

[157] B. J. Wood, Earth and Planetary Science Letters **117**, 593 (1993).

[158] J. Chipman, Metall. Transactions **3**, 55 (1972).

[159] E. Duman, M. Acet, T. Hülser, E. F. Wassermann, J. P. I. B. Rellinghaus, and P. Munsch, J. Appl. Phys. **96**, 5668 (2004).

[160] J. H. Jang, I. G. Kim, and H. Bhadeshia, Comp. Mat. Science **44**, 1319 (2009).

[161] A. K. Arzhnikov, L. V. Dobysheva, and C. Demangeat, J. Phys.: Condens. Matter **19**, 196214 (2007).

[162] G. Miyamoto, J. Oh, K. Hono, T. Furuhara, and T. Maki, Acta Mater. **55**, 5027 (2007).

[163] H. I. Faraoun, Y. D. Zhang, C. Esling, and H. Aourag, J. Appl. Phys. **99**, 093508 (2006).

[164] K. O. E. Henriksson, N. Sandberg, and J. Wallenius, Appl. Phys. Lett. **93**, 191912 (2008).

[165] M. Umemoto, Z. Liu, K. Masuyama, and K. Tsuchiya, Scr. Mater. **45**, 391 (2001).

[166] G. Naeser, Mitt. Kais.-Wilh.-Inst. Eisenforschg. **16**, 207 (1934).

[167] L. S. Darken and R. W. Gurry, J. Metals **3**, 1015 (1951).

[168] H. Seltz, H. McDonald, and C. Wells, Trans. AIME **140**, 263 (1940).

[169] J. Rusz, I. Turek, and M. Diviš, Phys. Rev. B **71**, 174408 (2005).

[170] W. Nolting, A. Vega, and T. Fauster, Z. Phys. B **96**, 357 (1995).

[171] J. Staunton, B. Gyorffy, A. Pindor, G. Stocks, and H. Winter, Journal of Magnetism and Magnetic Materials **45**, 15 (1984).

[172] S.-L. Shang, Y. Wang, and Z.-K. Liu, Phys. Rev. B **82**, 014425 (2010).

Publication List:

- A. Dick, F. Körmann, T. Hickel, and J. Neugebauer, "*Ab initio based determination of thermodynamic properties of cementite including vibronic, magnetic and electronic excitations*", *submitted* (2011).
- F. Körmann, A. Dick, T. Hickel, and J. Neugebauer, "*Role of spin quantization in determining the thermodynamic properties of magnetic transition metals*", Phys. Rev. B **83**, 165114 (2011).
- M. Friák, T. Hickel, F. Körmann, A. Udyansky, A. Dick, J. von Pezold, D. Ma, O. Kim, W. A. Counts, M. Šob, T. Gebhardt, D. Music, J. Schneider, D. Raabe, and J. Neugebauer, "Determining the elasticity of materials employing quantum-mechanical approaches: From the electronic ground state to the limits of materials stability", Steel Res. Int. **82**, 86 (2011).
- F. Körmann, A. Dick, T. Hickel, and J. Neugebauer, "*Rescaled Monte Carlo approach for magnetic systems: Ab initio thermodynamics of bcc iron*", Phys. Rev. B **81**, 134425 (2010).
- B. Hallstedt, J. von Appen, A. Dick, F. Körmann, T. Hickel, and J. Neugebauer, "*Thermodynamic properties of cementite (Fe_3C)*", Calphad **34**, 129 (2010).
- J. Neugebauer, B. Grabowski, F. Körmann, A. Dick, J. von Pezold, M. Friak, and T. Hickel, "*Ab Initio Based Multiscale Modeling of Engineering Materials: From a Predictive Thermodynamic Description to Tailored Mechanical Properties*", Asia Steel (*Proceeding*), (2009).
- F. Körmann, A. Dick, T. Hickel, and J. Neugebauer, "*The pressure dependence of the Curie temperature in bcc iron studied by ab initio simulations*", Phys. Rev. B **79**, 184406 (2009).
- T. Hickel, A. Dick, B. Grabowski, F. Körmann, and J. Neugebauer, "*Steel design from fully parameter-free ab initio computer simulations*", Steel Res. Int. **80**, 4 (2009).
- F. Körmann, J. Kienert, S. Schwieger, and W. Nolting, "*Cu cap layer on Ni_8/Cu(001): reorientation and T_C-shift*", Eur. Phys. J. B **65**, 499-504 (2008).
- F. Körmann, A. Dick, B. Grabowski, B. Hallstedt, T. Hickel, and J. Neugebauer, "*Free energy of bcc iron: Integrated ab initio derivation of vibrational, electronic, and magnetic contributions*", Phys. Rev. B "**78**, 033102 (2008).
- S. Henning, F. Körmann, S. Schwieger, J. Kienert, and W. Nolting, "*Green function theory versus quantum Monte Carlo calculations for thin magnetic films*", Phys. Rev. B **75**, 214401 (2007).
- F. Körmann, S. Schwieger, J. Kienert, and W. Nolting, "*A new type of temperature driven reorientation transition in magnetic thin films*", Eur. Phys. J. B **53**, 463-469 (2006).